MNRAS 000, 1–21 (2022) Preprint 10 November 2022 Compiled using MNRAS LATEX style file v3.0

Gaia white dwarfs within 40 pc III: spectroscopic observations of new candidates in the southern hemisphere

Mairi W. O'Brien,[1★] P.-E. Tremblay,[1] N. P. Gentile Fusillo,[2] M. A. Hollands,[3] B. T. Gänsicke,[1] D. Koester,[4] I. Pelisoli,[1] E. Cukanovaite,[1] T. Cunningham,[1] A. E. Doyle,[5] A. Elms,[1] J. Farihi,[6] J. J. Hermes,[7] J. Holberg,[8] S. Jordan,[9] B. L. Klein,[10] S. J. Kleinman,[11] C. J. Manser,[1,12] D. De Martino,[13] T. R. Marsh,[1] J. McCleery,[1] C. Melis,[14] A. Nitta,[15] S. G. Parsons,[3] R. Raddi,[16] A. Rebassa-Mansergas,[16,17] M. R. Schreiber,[18,19] R. Silvotti,[20] D. Steeghs,[1] O. Toloza,[18,19] S. Toonen,[21] S. Torres[16,17], A. J. Weinberger,[22] and B. Zuckerman[10]
(affiliations can be found after the references)

Accepted 2022 November 8. Received 2022 November 8; in original form 2022 October 4

ABSTRACT

We present a spectroscopic survey of 248 white dwarf candidates within 40 pc of the Sun; of these 244 are in the southern hemisphere. Observations were performed mostly with the Very Large Telescope (X-Shooter) and Southern Astrophysical Research Telescope. Almost all candidates were selected from *Gaia* Data Release 3 (DR3). We find a total of 246 confirmed white dwarfs, 209 of which had no previously published spectra, and two main-sequence star contaminants. Of these, 100 white dwarfs display hydrogen Balmer lines, 69 have featureless spectra, and two show only neutral helium lines. Additionally, 14 white dwarfs display traces of carbon, while 37 have traces of other elements that are heavier than helium. We observe 35 magnetic white dwarfs through the detection of Zeeman splitting of their hydrogen Balmer or metal spectral lines. High spectroscopic completeness (> 97 per cent) has now been reached, such that we have 1058 confirmed *Gaia* DR3 white dwarfs out of 1083 candidates within 40 pc of the Sun at all declinations.

Key words: white dwarfs – stars: statistics – stars: Galaxy – solar neighbourhood

1 INTRODUCTION

Approximately 97 per cent of stars will end their lives as white dwarfs (Fontaine et al. 2001). As stars with masses below ≈ 10 $M_\odot$ leave the main-sequence they become red giants, eventually shedding their outer layers as a planetary nebula, revealing the remaining core — a dense white dwarf held up by electron degeneracy pressure. Once the star is a white dwarf, it cools down for the remainder of its lifetime, a process that is accurately modelled. Photometry and spectroscopy are used to estimate the cooling age of a white dwarf. An initial-to-final mass relation (IFMR; e.g. El-Badry et al. 2018; Cummings et al. 2018; Barrientos & Chanamé 2021; Barnett et al. 2021) is employed to estimate the progenitor mass of the white dwarf, and evolutionary models are used to determine the main-sequence lifetime. From large samples of white dwarfs with known ages and Galactic kinematics, the stellar formation history at different look-back times in the Milky Way's past can be mapped (Fantin et al. 2019, and references therein).

Studies of white dwarf spectral types (Sion et al. 1983) reveal the chemical composition of the atmosphere and non-degenerate convectively mixed envelope, which has far-reaching implications. White dwarfs typically only show spectral lines from either hydrogen or helium, depending on their temperature and atmospheric composition. Van Maanen (1917) discovered the first white dwarf spectrum that displays elements heavier than helium, a spectral class that is now indicative of accreted planetary debris (Zuckerman et al. 2007; Farihi 2016; Veras 2021). These metal-polluted systems are used to understand how planets evolve along with their host stars. Ongoing accretion of planetary de-

★ E-mail: Mairi.O-Brien@warwick.ac.uk

bris has been observed directly through the detection of X-rays from a metal-polluted white dwarf (Cunningham et al. 2022). In contrast, the presence of trace carbon in the atmosphere of the classical DQ stars below 10 000 K is currently explained by convective dredge-up from the interior (Coutu et al. 2019; Koester et al. 2020; Bédard et al. 2022). High-mass DQ white dwarfs (and possibly some lower mass DQ) are likely explained by stellar mergers (Dunlap & Clemens 2015; Cheng et al. 2019; Coutu et al. 2019; Hollands et al. 2020; Farihi et al. 2022).

Degenerate stars provide a unique opportunity to probe extreme astrophysical environments, due to their large surface gravities. White dwarfs can have very strong magnetic fields and there are many proposed channels currently in use to explain their origin (see e.g. Schreiber et al. 2021a,b; Bagnulo & Landstreet 2022). Measured field strengths range from 10^4 to 10^9 Gauss, although the lower observational limit depends on spectral type and the availability of spectro-polarimetric observations (Ferrario et al. 2020; Bagnulo & Landstreet 2021).

The highly accurate astrometry and photometry of nearby stars measured from the *Gaia* spacecraft have enabled rapid progress in the definition of white dwarf samples. Gentile Fusillo et al. (2021) have created a catalogue of $\approx 360\,000$ high-confidence white dwarf candidates present in *Gaia* Early Data Release 3 (EDR3) based on the positions of the candidates on the Hertzsprung-Russell (HR) diagram. No new G, BP or RP magnitudes or astrometry have been released in *Gaia* DR3. Therefore, we reference DR3 as our source in this paper (Gaia Collaboration et al. 2021).

Cooling white dwarfs have a relatively large range of absolute *Gaia* magnitudes ($8 \lesssim M_{\rm G} \lesssim 18$ mag). In particular, the very faint end of the white dwarf luminosity function, which includes ultra-cool white dwarfs from old disc and halo stars (Hollands et al. 2021; Kaiser et al. 2021; Bergeron et al. 2022; Elms et al. 2022), can only be observed up to a distance of 40–100 pc given a *Gaia* limiting magnitude of $G \approx 20$–21. A sample which includes all ages and types of white dwarfs can only be achieved for 40–100 pc, therefore a volume-limited sample out to these distances is needed.

Spectroscopic follow-up observations of *Gaia* candidates are needed to confirm their classification as white dwarfs. Fortunately this work can build upon two decades of observations to define volume-limited samples of white dwarfs within 13 pc, 20 pc or 40 pc (Holberg et al. 2002; Giammichele et al. 2012; Limoges et al. 2015; Holberg et al. 2016). Additional spectroscopic campaigns in the northern hemisphere have targeted 40 pc white dwarfs (Tremblay et al. 2020, hereafter Paper I) using the *Gaia* DR2 white dwarf candidate catalogue from Gentile Fusillo et al. (2019). This resulted in a high level of spectroscopic completeness in the northern hemisphere within 40 pc (McCleery et al. 2020, hereafter Paper II).

As of now, Gentile Fusillo et al. (2021) have identified 542 white dwarf candidates in the northern hemisphere within 40 pc, 531 of which are spectroscopically confirmed from the literature (e.g. Gianninas et al. 2011; Kawka & Vennes 2012; Limoges et al. 2015; Subasavage et al. 2017, Paper I). In Paper II, the 40 pc northern sample was analysed based on a DR2 catalogue, which contained 521 confirmed white dwarfs (Gentile Fusillo et al. 2019).

In the southern hemisphere, Gentile Fusillo et al. (2021) have identified 541 white dwarf candidates within 40 pc, of which 304 are spectroscopically confirmed from the literature. There is a significant gap in the southern hemisphere observations that needs to be filled before meaningful analysis of the volume-limited 40 pc sample can occur.

In this Paper III on *Gaia* white dwarfs in 40 pc, we present spectroscopic follow-up observations of white dwarf candidates from DR3 within 40 pc, the vast majority of which are in the southern hemisphere.

We present 220 updated or confirmed spectral types in the southern hemisphere, and three in the northern hemisphere. We observe two DR3 candidates in the south that are main-sequence stars. We also find two white dwarfs not in the DR3 catalogue, and four white dwarfs within $1\sigma_\varpi$ of 40 pc. Following the results from the present work, the full *Gaia* 40 pc sample of white dwarf candidates has 1058 confirmed white dwarfs out of 1083 initial DR3 candidates (97 per cent spectroscopic completeness). Of the 25 remaining white dwarf candidates in DR3, two are confirmed as main-sequence stars in this paper, and 23 are unobserved. A detailed statistical analysis of the full 40 pc white dwarf sample, including a list of all spectral types and references, will appear in the upcoming Paper IV.

In this work, we discuss the nature of 246 *Gaia* white dwarf candidates, 34 of which have previous spectral type classifications in the literature (see Table 3 for citations). Four of these sources lie outside of 40 pc but are within $1\sigma_\varpi$ of that distance. The majority of targets, 242, are located in the southern hemisphere ($\delta < 0$ deg), while the remaining four are in the northern hemisphere.

2 OBSERVATIONS

2.1 Catalogue photometry and astrometry

Gentile Fusillo et al. (2021) used spectroscopically confirmed white dwarfs from the Sloan Digital Sky Survey (SDSS) (Ahumada et al. 2020) to select regions of the *Gaia* DR3 HR diagram in which white dwarfs are likely to be present. We selected white dwarf candidates from the catalogue of Gentile Fusillo et al. (2021) with a parallax $\varpi - \sigma_\varpi > 25$ mas such that all sources are within $1\sigma_\varpi$ of 40 pc. For each source, Gentile Fusillo et al. (2021) provide a parameter, the probability of being a white dwarf ($P_{\rm WD}$). Gentile Fusillo et al. (2021) suggest using $P_{\rm WD} > 0.75$ as a cut for the best compromise between completeness and contamination, and within 40 pc only eight candidates out of 1083 do not meet this cut, so we therefore include all 1083 candidates in our sample. We prioritised observations of high-confidence candidates within the southern hemisphere that had no previously published spectral type, or an ambiguous classification, as our goal is to increase the spectroscopic completeness of the overall 40 pc white dwarf sample. We use the WD Jhhmmss.ss ± ddmmss.ss naming convention introduced by Gentile Fusillo et al. (2019) in Table 3 and figures throughout the Appendix of this paper. For simplicity, we shorten their WD J names to WD Jhhmm ± ddmm in all other tables and text in this paper.

The Gentile Fusillo et al. (2021) catalogue does not include white dwarfs in unresolved binaries with brighter main-sequence companions. Toonen et al. (2017) predicts

Table 1. Log of spectroscopic observations, where wavelength ranges are those used for analysis in this work.

Telescope/ Instrument	Programme IDs	No. of objects in this work	Wavelength Coverage [Å]	Spectral Resolution (R)
VLT/X-Shooter	0102.C-0351 1103.D-0763 105.20ET.001	181	3600 – 10 200	UVB: 5400, VIS: 8900
SOAR/Goodman	SO2017B-009 SO2018A-013 SO2018B-015	49	3850 – 5550	1100
Shane/Kast	–	11	3600 – 7800	1900
GTC/OSIRIS	GTC103-21A	3	3950 – 5700	2200
WHT/ISIS	ITP08	2	3730 – 7290	Blue: 2000, Red: 3900
Tillinghast/FAST	–	2	3600 – 5500	1500

that 0.5–1 per cent of white dwarfs are part of an unresolved WD+MS binary, therefore in 40 pc we would expect that only 5–10 of these systems would be excluded from the Gentile Fusillo et al. (2021) DR3 catalogue.

2.2 Spectroscopy

We observed a total of 248 white dwarf candidates with parallaxes $\varpi - \sigma_\varpi > 25$ mas as presented in Table 1. The majority of targets (181) were observed from the VLT with the X-Shooter spectrograph (Vernet et al. 2011), where we employed slit widths of 1.0, 0.9 and 0.9 arcsec in the UVB (3000 – 5600 Å, $R = 5400$), VIS (5500 – 10 200 Å, $R = 8900$) and NIR (10 200 – 24 800 Å, $R = 5600$) arms, respectively.

The data were reduced following a standard procedure employing the `Reflex` pipeline (Freudling et al. 2013). The flux calibration used observations of hot DA white dwarfs obtained with the same instrument setup as the science spectroscopy, while telluric correction was performed using `molecfit` (Kausch et al. 2015; Smette et al. 2015). We extracted and inspected X-Shooter NIR spectra, and concluded that the signal-to-noise ratio was insufficient for meaningful analysis. Therefore we do not present any NIR spectra in this work.

We also observed 49 white dwarfs using the Goodman spectrograph (Clemens et al. 2004) mounted on the Southern Astrophysical Research telescope (SOAR). We used the 930 line mm^{-1} grating in the M2 mode (3850 – 5550 Å) and a 1.5 arcsec slit. The data were reduced using the `iraf` package `ccdproc`, and extracted using `noao.twodspec.apextract`. Flux calibration was carried out using spectrophotometric standard stars observed on the same night and with the same setup. The 930–M2 mode does not cover any skylines, and since arcs were not taken close in time to the observations, radial velocities (RVs) from these observations are not reliable.

We also present two observations using the Intermediate-dispersion Spectrograph and Imaging System (ISIS) on the William Herschel Telescope (WHT) and three observations using the Optical System for Imaging and low-Resolution Integrated Spectroscopy (OSIRIS) on the Gran Telescopio Canarias (GTC) (Cepa et al. 2000, 2003), which have the same setup as the observations reported in Paper I.

We also present eleven observations from the Kast Double Spectrograph mounted on the Shane 3 m telescope at the Lick Observatory. We used the 600/4310 grism for the blue, and either 830/8460 or 600/7500 gratings for the red, and we used slit widths of 1, 1.5, or 2 arcsec. We also present two observations from the FAst Spectrograph for the Tillinghast Telescope (FAST) at the F. L. Whipple Observatory. Instrument details for FAST are found in Fabricant et al. (1998).

We have used spectroscopic and photometric data to determine spectral types by human inspection for all 248 observed white dwarf candidates, which are listed in Table 3.

3 ATMOSPHERE AND EVOLUTION MODELS

All white dwarfs in this work are classified into one of the spectral types (SpT) described in Table 2 (Sion et al. 1983). Spectral types are allocated visually according to the relative strength of absorption lines in the spectrum, with 'H' representing Zeeman splitting from the presence of a magnetic field. We have derived atmospheric parameters and chemical abundances using photometric and spectroscopic fitting where appropriate. The notation log(X/Y) used in Table 2 and throughout this work refers to the logarithm of the number abundance ratio of any two chemical elements, X and Y.

3.1 Photometric parameters

Effective temperatures ($T_{\rm eff}$) and stellar radii can be derived for most white dwarfs using photometric and parallax fits to model atmospheres, providing the composition of the white dwarf atmosphere is known (Koester et al. 1979; Bergeron et al. 2001; Gentile Fusillo et al. 2021).

In this work, we rely on the photometric parameters already made available in Gentile Fusillo et al. (2021). In brief, either pure-hydrogen (Tremblay et al. 2011a), pure-helium (Bergeron et al. 2011), or mixed hydrogen and helium (Tremblay et al. 2014) model atmospheres are used, depending on the spectral type (see Table 2), to fit the *Gaia* DR3 photometry to determine $T_{\rm eff}$ and radii of all white dwarfs in the sample. Mixed atmosphere models use the ratio log(H/He) = −5 for all photometric fitting of DC white dwarfs above 7000 K. For DC stars within 5000 K $< T_{\rm eff} <$ 7000 K we use pure-helium atmospheres. For DC white dwarfs below 5000 K it is difficult to constrain the atmospheric composition, as the H α line would be very difficult to detect with most ground- and space-based current or

Table 2. Definitions of all white dwarf spectral types discussed in this work, where photometric model composition refers to composition-selected Gentile Fusillo et al. (2021) parameters. Adopted parameters for DZ and DQ white dwarfs in this work use the hybrid photometric/spectroscopic methods and are shown instead in Tables 6–8.

Spectral type (SpT)	Number in this work	Spectral features in order of strength	Photometric model composition
DA	100	Hydrogen Balmer	pure-H
DAH	28	Hydrogen Balmer + magnetic	pure-H
DB	2	Neutral helium	log(H/He) = −5
DC	69	Featureless	log(H/He) = −5, pure-He below 7000 K, assumed pure-H below 5000 K
DAZ	10	Hydrogen Balmer + metal	pure-H
DZ	12	Metal	log(H/He) = −5, pure-He below 7000 K
DZH	5	Metal + magnetic	log(H/He) = −5, pure-He below 7000 K
DZA	4	Metal + hydrogen Balmer	log(H/He) = −5, pure-He below 7000 K
DZAH	2	Metal + hydrogen Balmer + magnetic	log(H/He) = −5, pure-He below 7000 K
DQ	7	Carbon (molecular bands)	log(H/He) = −5, pure-He below 7000 K
warm DQ	1	Carbon (atomic lines)	pure-He
DQpec	2	Carbon (molecular bands, shifted wavelengths)	log(H/He) = −5, pure-He below 7000 K
DQZ	2	Carbon + metal	log(H/He) = −5, pure-He below 7000 K
DZQ	1	Metal + carbon	log(H/He) = −5, pure-He below 7000 K
DZQH	1	Metal + carbon + magnetic	log(H/He) = −5, pure-He below 7000 K

near-future spectroscopic instruments, so we assume pure-hydrogen atmospheres (Gentile Fusillo et al. 2020, Paper II).

Surface gravities (log(g)), masses and cooling ages are derived using evolutionary models (Bédard et al. 2020). Table 3 shows the derived parameters from a homogeneous set of photometric fits from Gentile Fusillo et al. (2021) using *Gaia* data only. In this work we also derive independent parameters from hybrid fits using spectroscopy and photometry for DQ and DZ stars (see Section 3.3 for details).

3.2 Spectroscopic parameters

We derive $T_{\rm eff}$ and log(g) from spectroscopic fits of Balmer lines in non-magnetic DA white dwarfs using a `Python` implementation adapted from previous Balmer line fitting procedures described extensively in Liebert et al. (2005); Tremblay et al. (2011b); Gianninas et al. (2011, Paper I). This modern fitting code is part of the 4MOST multi-object spectroscopic (MOS) survey consortium pipeline (Chiappini et al. 2019; De Jong et al. 2019) and will also be a key resource for other MOS surveys such as WEAVE (Dalton et al. 2020). We rely on DA models from Tremblay et al. (2011b) with 3D corrections from Tremblay et al. (2013). Table 3 shows spectroscopic parameters determined from this method.

Only DA spectra with at least two visible Balmer lines are fitted. If there is only one spectral line available, either due to the $T_{\rm eff}$ and log(g) of the white dwarf or incomplete spectral coverage, the best-fit parameters cannot be well constrained. For DA white dwarfs below ≈ 5200 K observed with X-Shooter, Balmer lines from H β and above become very weak while $T_{\rm eff}$ and log(g) are degenerate in predicting the equivalent width of the H α line. It is therefore not possible to fit both parameters.

For the two DB white dwarfs in our sample, we use the 3D model atmospheres of Cukanovaite et al. (2021) to obtain log(H/He) and $T_{\rm eff}$. We use a fitting procedure similar to that of Bergeron et al. (2011).

The DC and magnetic white dwarfs in the sample are not fitted spectroscopically but best-fit parameters from *Gaia* photometry are presented in Table 3. Best-fit parameters for confirmed unresolved binary systems are not given. White dwarf candidates that were found to be main-sequence stars are not analysed further.

3.3 Combined spectroscopic and photometric parameters

Atmospheres with carbon traces and metal-polluted white dwarfs are fitted using models from Koester (2010) and improvements described therein. Fits are presented in Sections 4.6 and 4.7. We adopt an iterative approach of combined photometric and spectroscopic fitting. We start by computing a small grid of models with an initial guess on the metal abundances to fit the photometry for $T_{\rm eff}$ and log(g). The subsequent step is then to calculate a new grid of models with variable metal abundances at fixed atmospheric parameters in order to fit chemical composition. We repeat these two steps until convergence.

4 RESULTS

We confirm the classification of 246 white dwarfs within $1\sigma_\varpi$ of 40 pc, 213 of which had no previous observations from literature. The distribution of log(g) as a function of $T_{\rm eff}$ for all white dwarfs in our sample is shown in Fig. 1 based on *Gaia* DR3 photometric parameters (Gentile Fusillo et al. 2021). In Fig. 1, all sources are fitted as single stars. There is a visible second track at log(g) ~ 7.4, below the main distribution at log(g) ~ 8.0 in Fig. 1, where double degenerate binary candidates with about twice the luminosity of a single white dwarf are located. Their log(g) values are underestimated as their photometry is fitted here as if they were single stars.

In Fig. 1 we observe a downward trend in photometric log(g) against $T_{\rm eff}$ below around 6000 K. A similar trend has been discussed following *Gaia* DR2 (Hollands et al. 2018; Bergeron et al. 2019, Paper I, Paper II), and could be due

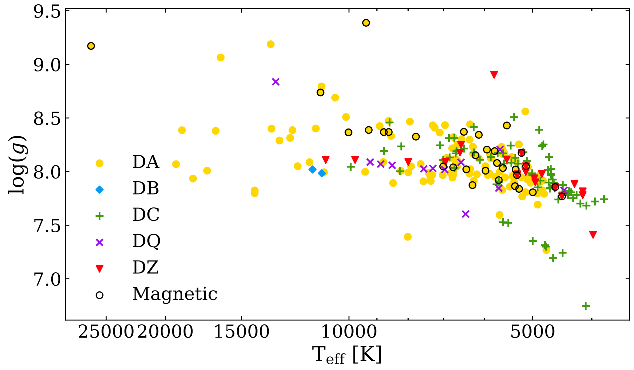

Figure 1. log(g) against $T_{\rm eff}$ distribution for white dwarfs within 40 pc that have been spectroscopically observed in this work, where parameters have been determined from fitting of *Gaia* DR3 photometry. Magnetic stellar remnants have black contours. Data are colour- and symbol-coded by their primary spectral type classification only, for simplicity.

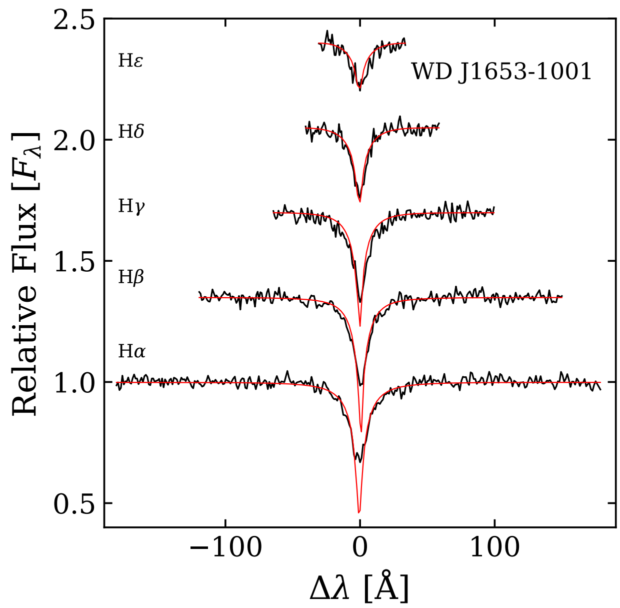

Figure 2. Spectroscopic fits to the normalised Balmer lines for the DAe white dwarf **WD J1653−1001**.

to *Gaia* temperatures being too low or luminosities being too large (see Paper I for details).

Only the two DZH white dwarfs **WD J0548−7507** and **WD J2147−4035**, and the DA **WD J1956−5258** do not have atmospheric parameters determined from *Gaia* DR3 photometry in Gentile Fusillo et al. (2021). **WD J2147−4035** is a very cool IR-faint white dwarf (Apps et al. 2021), and its spectroscopy and photometry has been fitted in Elms et al. (2022). **WD J0548−7507** was selected as a white dwarf candidate by Gentile Fusillo et al. (2019) in *Gaia* DR2, but it was not selected in the DR3 catalogue due to failing the BP−RP excess factor rule, as it is in the Large Magellanic Cloud region (Gentile Fusillo et al. 2021). **WD J0548−7507** has parameters of $T_{\rm eff} = 4720 \pm 170$ K and $\log(g) = 7.9 \pm 0.1$ from *Gaia* DR2 photometric fitting. **WD J1956−5258** was not selected in either of the DR2 or DR3 white dwarf catalogues, due to its bright, *Gaia* G-band magnitude 10, M-dwarf companion separated by 4.7 arcsec on the sky.

We have updated the spectral types of five white dwarfs in the sample previously classified as DC, owing to the higher-quality spectroscopy we have obtained as follows: **WD J1821−5951** (Subasavage et al. 2017) and **WD J1430−2403** (Reid & Gizis 2005) are DAs, **WD J0252−7522** (Subasavage et al. 2007) and **WD J1412−1842** (Dupuis et al. 1994) are DAHs and **WD J2112−2922** (Raddi et al. 2017) is a DZQ. These updated spectral types are shown in italics in Table 3.

While observations focused on southern hemisphere white dwarfs, we also obtained spectroscopy of three northern hemisphere targets omitted from Paper I due to low $P_{\rm WD}$ values in DR2: **WD J1318+7353**, **WD J1815+5532**, and **WD J1919+4527**. In DR3 (Gentile Fusillo et al. 2021), the $P_{\rm WD}$ values of these white dwarfs increased to 0.96, 0.75, and 0.87 respectively. We also re-observed the highly-polluted northern white dwarf **WD J0358+2157** with X-Shooter.

All objects with a parallax below 25 mas are flagged with an asterisk, these objects may be a member of the 40 pc sample within $1\sigma_{\varpi}$. The best estimates of spectroscopic atmospheric parameters and chemical abundances are displayed in Table 5 for DB white dwarfs, Table 6 for DAZ white dwarfs, Table 7 for DZ and DZA white dwarfs, and Table 8 for all white dwarfs with carbon features. The observations of main-sequence stars that contaminate our sample are discussed in Section 4.9.

4.1 DA white dwarfs

The spectra for all observed DA white dwarfs are shown in Fig. A1. All DA white dwarfs with *Gaia* $T_{\rm eff} > 5200$ K, and with more than one spectral line visible, were fitted spectroscopically using our fitting code described in Section 3, with best-fit atmospheric parameters corrected for 3D convection (Tremblay et al. 2013) identified in Table 3. We show fits to Balmer lines for the DA white dwarfs in Fig A2. We do not fit the spectrum of **WD J0312−6444** as it is a known unresolved DA+DA binary (Kilic et al. 2020).

WD J1653−1001 is a DA white dwarf for which we make a tentative detection of emission in the core of the H α and H β lines (see Fig. 2). This emission appears to be similar to that seen in the DAe white dwarf **WD J0412+7549** observed in Paper I. Therefore we make the tentative classification of **WD J1653−1001** as a DAe. A discussion of these systems will be presented in Elms et al. (in prep.).

4.2 Magnetic white dwarfs

Fig. A3 shows 28 magnetic white dwarfs with hydrogen atmospheres that have spectral type DAH. It is not simple to determine the mass of a highly magnetic white dwarf by photometric fitting in the optical because of Zeeman splitting and displacement of spectral lines. Therefore the error bars of the log(g) values quoted in Table 3 for cool magnetic white dwarfs may be slightly underestimated (Paper II).

WD J0103−0522 was analysed in Paper I, where a quadratic wavelength shift of the π-component was observed,

Table 3. Spectral types and parameters of the white dwarf sample

WD J name	SpT	Parallax (mas)	$T_{\rm eff}$ [K] 3D Spectro	log(*g*) 3D Spectro	$T_{\rm eff}$ [K] Gaia	log(*g*) Gaia	Note
001349.89−714954.26	DAH	53.21 (0.02)	–	–	6280 (30)	7.87 (0.02)	(a)
001830.36−350144.71	DAH	28.05 (0.06)	–	–	7010 (60)	8.05 (0.03)	
003036.62−685458.25	DA	25.46 (0.04)	8640 (40)	7.98 (0.05)	8790 (230)	8.09 (0.06)	
003713.77−281449.81	DC:	26.5 (0.1)	–	–	5340 (60)	8.13 (0.04)	
004126.61−503258.58	DC	31.84 (0.09)	–	–	4180 (60)	7.70 (0.04)	
004434.77−114836.05	DZ	27.1 (0.1)	–	–	5300 (70)	7.98 (0.06)	
005311.22−501322.87	DC	28.72 (0.06)	–	–	5570 (60)	8.08 (0.03)	
005411.42−394041.53	DA	37.34 (0.05)	6580 (20)	8.43 (0.02)	6260 (40)	8.23 (0.02)	
010338.56−052251.96	DAH	34.4 (0.1)	–	–	9380 (290)	9.39 (0.05)	(b)
012953.18−322425.86	DA	26.10 (0.05)	6770 (80)	8.1 (0.1)	6720 (50)	8.11 (0.03)	
013843.16−832532.89	DA	31.92 (0.03)	7750 (70)	8.14 (0.09)	7630 (60)	8.07 (0.02)	
* 014240.09−171410.85	DAH	24.97 (0.09)	–	–	5560 (50)	8.00 (0.03)	
014300.98−671830.35	DAZ	102.91 (0.01)	–	–	6350 (30)	7.98 (0.02)	(c)
015038.47−720716.54	DC	31.53 (0.04)	–	–	6840 (60)	8.13 (0.03)	(d)
021228.98−080411.00	DA	59.76 (0.02)	9020 (20)	8.14 (0.02)	8470 (110)	7.89 (0.03)	
024300.36−603414.82	DA	29.86 (0.06)	5760 (120)	8.5 (0.3)	5600 (50)	8.20 (0.03)	
024527.76−603858.32	DA	28.08 (0.04)	6150 (70)	8.4 (0.1)	5880 (50)	7.98 (0.03)	
025017.18−224130.53	DA	27.91 (0.08)	–	–	5620 (60)	8.23 (0.03)	
025245.61−752244.56	*DAH*	32.05 (0.04)	–	–	6200 (50)	8.15 (0.02)	(e)
025332.00−654559.93	DA	26.99 (0.05)	5600 (60)	8.0 (0.1)	5450 (50)	7.86 (0.03)	
025759.87−302709.99	DA	25.95 (0.06)	6330 (60)	8.1 (0.1)	6170 (40)	7.98 (0.02)	
030154.44−831446.19	DA	29.89 (0.03)	6860 (60)	8.0 (0.1)	6810 (50)	7.99 (0.02)	
030407.15−782454.62	DA	25.11 (0.07)	5500 (30)	7.99 (0.04)	5360 (60)	7.90 (0.04)	
031225.70−644410.89	DA	27.33 (0.02)	–	–	–	–	DA+DA (f)
031318.66−560734.99	DA	28.70 (0.02)	11 230 (60)	8.03 (0.03)	10 990 (120)	7.99 (0.02)	
031646.48−801446.19	DA	28.02 (0.03)	7510 (50)	8.0 (0.1)	7360 (60)	7.95 (0.02)	
031715.85−853225.56	DAH	34.04 (0.03)	–	–	26470 (1370)	9.17 (0.05)	(g)
031719.13−853231.29	DA	34.02 (0.02)	17 050 (230)	8.43 (0.03)	16 530 (290)	8.38 (0.02)	(h)
032646.69−592700.23	DA	32.13 (0.05)	6380 (90)	8.5 (0.2)	6330 (60)	8.44 (0.02)	
034010.17−361038.22	DA	29.08 (0.05)	5870 (60)	8.2 (0.1)	5610 (40)	7.83 (0.03)	(i)
034347.42−512516.55	DAZ	35.83 (0.03)	–	–	6740 (50)	8.01 (0.02)	
035005.27−685307.56	DA	30.02 (0.05)	–	–	4910 (50)	7.80 (0.03)	
035531.89−561128.32	DAH	30.35 (0.05)	–	–	5770 (50)	8.19 (0.03)	
035826.49+215726.16	DAZ	27.67 (0.07)	–	–	6780 (80)	8.22 (0.03)	(b)
041630.04−591757.19	DA	54.58 (0.03)	15 540 (70)	7.96 (0.01)	14 270 (240)	7.82 (0.02)	(j)
041823.34−500424.14	DC	41.93 (0.06)	–	–	4700 (40)	8.14 (0.03)	
042021.33−293426.26	DAH	32.16 (0.04)	–	–	6420 (40)	8.02 (0.02)	
042357.67−455042.27	DA	33.40 (0.04)	5900 (40)	8.49 (0.06)	5550 (40)	7.95 (0.02)	(k)
042643.98−415341.44	DAZ	29.06 (0.04)	–	–	6130 (60)	8.12 (0.03)	
042731.73−070802.80	DC	25.17 (0.06)	–	–	6720 (60)	8.04 (0.03)	(b)
044538.42−423255.05	DAZ	36.60 (0.02)	–	–	6750 (50)	7.97 (0.02)	
044903.21−241239.20	DA	33.70 (0.07)	–	–	4870 (50)	7.96 (0.04)	
045943.21−002238.86	DA	40.46 (0.03)	11 060 (100)	8.81 (0.04)	11 090 (120)	8.79 (0.02)	(l)
050552.46−172243.48	DAH	51.68 (0.03)	–	–	5350 (30)	7.86 (0.02)	(m)
051942.85−701401.50	DC	25.22 (0.10)	–	–	4540 (70)	7.74 (0.05)	
052436.27−053510.52	DA	27.98 (0.02)	17 330 (120)	8.08 (0.03)	17 080 (310)	8.01 (0.02)	(b)
052844.01−430449.21	DA	26.09 (0.03)	10 620 (140)	8.70 (0.04)	10 540 (140)	8.69 (0.02)	(n)
053446.50−524150.29	DA	25.21 (0.05)	6110 (60)	8.2 (0.1)	5980 (70)	8.05 (0.04)	
054249.69−190107.34	DC	32.79 (0.03)	–	–	8763 (80)	8.19 (0.02)	
* 054858.25−750745.20	DZH	24.96 (0.09)	–	–	4720 (170)	7.9 (0.1)	DR2 Parameters
055118.71−260912.89	DC	25.28 (0.06)	–	–	4750 (40)	7.30 (0.03)	
055443.04−103521.34	DZ	65.41 (0.02)	–	–	6580 (40)	8.12 (0.02)	(b)
055802.46−722848.43	DC	25.70 (0.05)	–	–	6720 (80)	8.31 (0.03)	
055808.89−542804.68	DA	25.24 (0.08)	–	–	4850 (60)	7.92 (0.05)	
061813.08−801155.22	DA	27.98 (0.02)	14 800 (240)	8.37 (0.06)	13 400 (230)	8.40 (0.01)	(o)
062620.54−185006.83	DAZ	27.94 (0.04)	–	–	7300 (60)	7.97 (0.02)	
064604.27−224633.04	DC	31.26 (0.09)	–	–	4380 (60)	7.78 (0.04)	
064806.66−205839.53	DA	36.97 (0.06)	–	–	5040 (30)	7.91 (0.02)	
070551.92−083526.76	DC	39.42 (0.08)	–	–	4620 (340)	7.9 (0.3)	
071550.55−370642.20	DA	29.23 (0.04)	7260 (90)	8.3 (0.2)	7240 (70)	8.41 (0.02)	
072251.38−304234.38	DA	42.72 (0.07)	–	–	5140 (40)	8.56 (0.02)	
073326.40−445325.34	DA	25.60 (0.02)	9500 (40)	7.98 (0.04)	9410 (80)	8.00 (0.02)	
075328.47−511436.98	DAH	30.56 (0.03)	–	–	9280 (100)	8.39 (0.02)	
075447.40−241527.71	DAH	26.54 (0.07)	–	–	5940 (50)	8.21 (0.03)	
080151.04−282831.73	DQpec	28.54 (0.06)	–	–	5680 (40)	7.85 (0.03)	

Notes: (a) Landstreet & Bagnulo (2019), (b) Tremblay et al. (2020), (c) Subasavage et al. (2017), (d) Subasavage et al. (2008), (e) Subasavage et al. (2007), (f) Külebi et al. (2010), (g) Kilic et al. (2020), (h) Barstow et al. (1995), (i) Reid & Gizis (2005), (j) Bédard et al. (2017), (k) Scholz et al. (2000), (l) Gianninas et al. (2011), (m) Blouin et al. (2019b), (n) O'Donoghue et al. (2013), (o) Kepler et al. (2000), (p) Dufour et al. (2005), (q) Bergeron et al. (2001), (r) Coutu et al. (2019), (s) Hollands et al. (2017), (t) Dupuis et al. (1994), (u) Bagnulo & Landstreet (2021), (v) Kirkpatrick et al. (2016), (w) Raddi et al. (2017), (x) Bergeron et al. (2021), (y) Elms et al. (2022). Objects with an asterisk before their name have a parallax value outside of 40 pc but may still be within that volume at 1σ. A spectral type in italics indicates we have updated the classification in this work. A spectral type followed by a colon represents a tentative classification. Table 2 shows which atmospheric composition was used for the photometric fits of each white dwarf. All quoted uncertainties represent the intrinsic fitting errors. The *3D Spectro* column for DA white dwarfs presents fitted Balmer line parameters.

Table 3. Spectral types and parameters of the white dwarf sample (continued)

WD J name	SpT	Parallax (mas)	$T_{\rm eff}$ [K] 3D Spectro	log(g) 3D Spectro	$T_{\rm eff}$ [K] Gaia	log(g) Gaia	Note
080833.93−530059.48	DZA	33.29 (0.08)	–	–	4140 (100)	7.78 (0.06)	
081200.29−610809.79	DA	25.02 (0.05)	6340 (60)	8.2 (0.1)	6260 (60)	8.17 (0.03)	
081227.07−352943.32	DC	89.51 (0.02)	–	–	6240 (30)	8.18 (0.01)	
081630.14−464113.24	DC	43.48 (0.06)	–	–	4240 (40)	7.78 (0.03)	
081716.19−680838.31	DQpec	25.7 (0.1)	–	–	4440 (100)	7.83 (0.07)	
081843.92−151208.31	DZ	30.41 (0.14)	–	–	3980 (210)	7.4 (0.2)	
082533.15−510730.83	DC:	37.42 (0.05)	–	–	5010 (40)	7.98 (0.03)	
083759.16−501745.76	DA	31.52 (0.02)	12 860 (40)	8.33 (0.02)	12 490 (160)	8.31 (0.01)	
084635.27−362206.68	DA	30.89 (0.07)	–	–	4890 (40)	7.91 (0.03)	
085021.30−584806.21	DZA	42.96 (0.08)	–	–	5600 (50)	8.90 (0.02)	
085430.49−250848.99	DA	31.88 (0.05)	6720 (90)	8.2 (0.1)	6650 (60)	8.25 (0.02)	
090212.89−394553.32	DAH	27.46 (0.03)	–	–	8770 (100)	8.37 (0.02)	
090633.51−262656.02	DA	41.34 (0.06)	–	–	4990 (40)	7.95 (0.03)	
090734.25−360907.93	DA	25.32 (0.08)	5500 (130)	8.2 (0.3)	5220 (60)	7.95 (0.04)	
091228.06−264201.50	DA	27.48 (0.05)	12 730 (40)	9.47 (0.03)	13 440 (280)	9.19 (0.02)	
091600.94−421520.68	DZH:	44.35 (0.04)	–	–	5130 (30)	8.05 (0.02)	
091620.71−631117.21	DA	42.82 (0.02)	10 270 (40)	8.50 (0.03)	10 110 (100)	8.51 (0.02)	
091708.67−454613.68	DAZ	35.31 (0.03)	–	–	6330 (40)	8.02 (0.02)	
091808.59−443724.25	DAH	35.27 (0.05)	–	–	5330 (40)	8.02 (0.03)	
092449.05−491529.60	DC:	44.31 (0.04)	–	–	5420 (30)	8.08 (0.02)	
093011.42−295943.38	DA	30.53 (0.07)	–	–	5100 (60)	7.93 (0.05)	
093659.79−372130.80	DQ	38.10 (0.02)	–	–	9230 (90)	8.09 (0.02)	(p)
093659.94−372126.91	DA	38.15 (0.02)	8130 (60)	8.0 (0.1)	7910 (60)	8.05 (0.02)	(l)
093736.24−385223.21	DA	28.99 (0.05)	5930 (40)	8.43 (0.06)	5660 (50)	8.00 (0.03)	
094052.75−423225.46	DC	26.71 (0.07)	–	–	5860 (60)	8.14 (0.03)	
094240.23−463717.68	DAH	48.83 (0.03)	–	–	5970 (30)	8.01 (0.02)	
095522.89−711808.37	DA	32.73 (0.02)	14 420 (260)	7.87 (0.05)	14 280 (210)	7.80 (0.02)	(l)
101039.30−471729.83	DA	26.94 (0.06)	5980 (40)	8.24 (0.08)	5850 (40)	8.12 (0.02)	
101341.21−523400.86	DA	25.25 (0.05)	7230 (40)	8.49 (0.06)	6920 (60)	8.13 (0.02)	
101812.80−343846.05	DA	30.49 (0.09)	–	–	5090 (50)	8.04 (0.04)	
101947.34−340221.88	DAH	36.30 (0.05)	–	–	6480 (50)	8.37 (0.02)	
103427.04−672239.24	DA	42.40 (0.02)	19 430 (150)	8.44 (0.02)	18 780 (350)	8.39 (0.02)	
103706.75−441236.96	DAH	25.57 (0.07)	–	–	5680 (50)	7.92 (0.03)	
104646.00−414638.85	DAH	35.41 (0.04)	–	–	6750 (40)	8.04 (0.02)	
105735.13−073123.18	DC	81.51 (0.02)	–	–	7100 (50)	8.25 (0.02)	(q)
105747.61−041330.16	DZ	27.51 (0.06)	–	–	6950 (60)	8.09 (0.03)	(r)
105915.98−281955.96	DAZ	25.34 (0.06)	–	–	6650 (60)	8.05 (0.03)	
111717.11−441134.49	DC	37.47 (0.04)	–	–	5590 (30)	7.53 (0.02)	
113216.54−360204.95	DZH	27.44 (0.12)	–	–	4590 (70)	7.86 (0.06)	
114122.38−350406.93	DZA	34.18 (0.09)	–	–	4600 (40)	7.84 (0.04)	
114734.45−745759.24	DC:	50.08 (0.06)	–	–	3820 (80)	7.74 (0.05)	
114901.67−405114.98	DC	25.7 (0.1)	–	–	4290 (60)	7.75 (0.05)	
115020.14−255335.40	DC	34.05 (0.05)	–	–	6690 (60)	8.17 (0.02)	
115403.49−310145.29	DC	25.39 (0.07)	–	–	6110 (60)	8.11 (0.03)	
121456.38−023402.84	DZH	26.28 (0.12)	–	–	5220 (60)	8.17 (0.04)	(s)
121616.94−375848.13	DC	26.3 (0.1)	–	–	4460 (70)	7.88 (0.07)	
121724.77−632945.73	DZ	26.65 (0.04)	–	–	8000 (70)	8.09 (0.02)	
∗ 122257.77−742707.7	DA	24.96 (0.07)	6020 (50)	8.6 (0.1)	5580 (60)	7.95 (0.04)	
123156.66−503247.99	DA	30.48 (0.03)	19 110 (20)	8.0 (0.2)	18 010 (350)	7.94 (0.02)	
123445.37−444001.75	DC	35.12 (0.04)	–	–	6670 (70)	8.19 (0.03)	
124112.37−243428.54	DZ	26.38 (0.08)	–	–	6550 (70)	8.25 (0.03)	
124155.92−133501.27	DC	27.82 (0.05)	–	–	8250 (80)	8.00 (0.03)	
124504.52−491336.69	DQ	34.41 (0.03)	–	–	8500 (70)	8.06 (0.02)	
130744.29−792511.64	DC	25.4 (0.1)	–	–	4670 (80)	7.98 (0.07)	
131727.39−543808.28	DA	40.57 (0.04)	5710 (40)	7.90 (0.08)	5760 (30)	7.95 (0.02)	
131830.01+735318.25	DC:	27.4 (0.1)	–	–	5000 (40)	7.35 (0.04)	
131958.95−563928.42	DC	27.93 (0.05)	–	–	7010 (50)	8.11 (0.02)	
132550.44−601508.04	DB	27.82 (0.03)	11 080 (130)	–	11 510 (120)	7.98 (0.03)	
132756.43−281716.98	DQ	27.48 (0.06)	–	–	6440 (140)	7.60 (0.06)	
133216.49−440838.71	DC	29.25 (0.09)	–	–	5710 (80)	8.17 (0.04)	
133314.60−675117.19	DZ	37.98 (0.05)	–	–	5510 (90)	8.11 (0.05)	
134349.01−344749.39	DA	27.69 (0.09)	–	–	5140 (80)	7.81 (0.05)	
134441.03−650942.13	DA	25.90 (0.09)	–	–	4790 (130)	7.79 (0.09)	
140115.27−391432.21	DAH	36.00 (0.09)	–	–	5510 (60)	8.43 (0.03)	
140608.61−695726.60	DA	27.92 (0.04)	6910 (40)	7.99 (0.05)	6770 (50)	7.95 (0.02)	
141041.67−751030.18	DZA	30.01 (0.08)	–	–	4950 (40)	7.90 (0.04)	
141159.17−592044.99	DA	69.44 (0.03)	6780 (40)	8.07 (0.05)	6650 (40)	8.11 (0.02)	
141220.36−184241.64	*DAH*	30.06 (0.09)	–	–	5720 (90)	8.08 (0.05)	(t)
141622.47−653126.81	DA	25.92 (0.05)	9130 (80)	8.58 (0.08)	8610 (90)	8.47 (0.02)	
142254.17−460549.72	DC	26.45 (0.08)	–	–	6480 (60)	8.22 (0.03)	
142428.39−510233.63	DQ	31.59 (0.05)	–	–	6550 (60)	8.09 (0.03)	
143015.38−240326.12	*DA*	30.7 (0.1)	–	–	4870 (60)	7.90 (0.05)	(i)
143019.96−252040.40	DA	31.64 (0.06)	6930 (40)	8.33 (0.06)	6740 (70)	8.32 (0.03)	
143826.23−560110.20	DC	25.61 (0.05)	–	–	8210 (80)	8.24 (0.02)	
144710.68−694040.21	DC	33.76 (0.07)	–	–	4470 (30)	7.24 (0.02)	
150324.74−244129.02	DA	38.51 (0.05)	6100 (30)	8.7 (0.8)	5670 (30)	7.60 (0.02)	
151431.85−462555.28	DQZ	44.27 (0.03)	–	–	7540 (60)	8.03 (0.02)	
151907.38−485423.83	DQZ	28.26 (0.04)	–	–	8870 (80)	8.07 (0.02)	

Table 3. Spectral types and parameters of the white dwarf sample (continued)

WD J name	SpT	Parallax (mas)	$T_{\rm eff}$ [K] 3D Spectro	log(*g*) 3D Spectro	$T_{\rm eff}$ [K] Gaia	log(*g*) Gaia	Note
152915.63−642811.20	DA	30.82 (0.07)	5550 (30)	8.00 (0.04)	5200 (60)	7.77 (0.04)	
152926.39−141614.44	DA	26.7 (0.1)	5310 (100)	8.2 (0.2)	5270 (90)	8.25 (0.06)	
153044.96−620304.10	DAZ	26.56 (0.07)	–	–	5880 (60)	8.17 (0.03)	
154053.08−485837.95	DZA	27.4 (0.1)	–	–	4830 (50)	7.98 (0.04)	
155131.68−385049.90	DC	28.1 (0.1)	–	–	5290 (40)	8.07 (0.03)	
160027.92−131949.93	DC	27.2 (0.1)	–	–	5010 (100)	7.97 (0.08)	
160137.01−383209.35	DA	30.70 (0.09)	–	–	4910 (40)	7.69 (0.03)	
160454.29−720347.59	DC	27.06 (0.06)	–	–	4090 (40)	6.75 (0.04)	
162224.44−551132.01	DA	27.39 (0.07)	5640 (200)	8.0 (0.5)	5400 (80)	7.96 (0.05)	
162558.78−344145.71	DAH	28.6 (0.1)	–	–	5000 (60)	7.81 (0.04)	
163029.74−373936.84	DC	30.1 (0.1)	–	–	–	–	
163058.32−281815.48	DC	25.5 (0.2)	–	–	3950 (140)	7.72 (0.09)	
163337.05−371314.28	DC	47.40 (0.07)	–	–	5430 (40)	8.24 (0.02)	
163626.53−873706.08	DQ	26.42 (0.07)	–	–	5660 (70)	8.21 (0.04)	
164725.24−544237.58	DA	45.20 (0.02)	8800 (30)	8.34 (0.02)	8530 (70)	8.33 (0.02)	
165335.21−100116.33	DAe	30.65 (0.04)	7360 (40)	7.84 (0.06)	7350 (90)	7.91 (0.03)	
165538.10−232555.73	DA	26.15 (0.06)	7120 (40)	8.09 (0.05)	6990 (50)	8.10 (0.02)	
165823.76−805857.14	DC	44.62 (0.05)	–	–	4690 (30)	7.85 (0.03)	
170054.19−690832.65	DA	27.86 (0.05)	8160 (40)	8.59 (0.03)	7950 (70)	8.47 (0.02)	
170427.96−005026.31	DA	37.04 (0.05)	6650 (700)	8.39 (0.08)	6540 (50)	8.30 (0.02)	
170430.68−481953.11	DC	38.8 (0.1)	–	–	5180 (40)	8.18 (0.03)	
170641.36−264334.71	DAH	76.65 (0.03)	–	–	6130 (30)	8.34 (0.01)	(u)
171436.16−161243.30	DAH	26.98 (0.04)	–	–	11 140 (140)	8.74 (0.02)	
171652.09−590636.29	DAH	33.51 (0.03)	–	–	8600 (90)	8.37 (0.02)	
172239.79−355441.65	DA	27.18 (0.08)	7120 (50)	8.32 (0.08)	7100 (130)	8.36 (0.04)	
173351.73−250759.90	DA	26.8 (0.1)	5520 (40)	8.00 (0.08)	5560 (60)	8.17 (0.04)	
173800.77−311237.21	DC	25.3 (0.1)	–	–	4660 (70)	7.97 (0.06)	
173837.46−342729.28	DA	25.5 (0.1)	–	–	4830 (120)	7.83 (0.09)	
174220.63−203935.92	DC	34.42 (0.07)	–	–	5590 (50)	8.17 (0.03)	
174246.61−650514.67	DC	33.43 (0.04)	–	–	8580 (90)	8.46 (0.02)	
174349.28−390825.95	DA	46.83 (0.02)	11 700 (20)	7.89 (0.01)	11 610 (210)	8.09 (0.03)	
174611.08−625141.41	DA	29.04 (0.04)	7530 (40)	8.00 (0.06)	7400 (60)	7.99 (0.02)	
174736.82−543631.16	DC	73.99 (0.05)	–	–	4360 (30)	7.82 (0.02)	(v)
175325.53−840510.03	DC	26.27 (0.09)	–	–	5110 (70)	8.10 (0.05)	
175554.31−245648.94	DA	26.62 (0.03)	12 830 (10)	8.395 (0.006)	13 000 (200)	8.29 (0.02)	
175931.34−620108.87	DA	26.01 (0.04)	17 000 (70)	9.14 (0.02)	16 220 (270)	9.06 (0.01)	
180314.84−805750.43	DC	29.7 (0.1)	–	–	4800 (70)	8.25 (0.05)	
180315.18−371725.54	DA	37.84 (0.07)	5500 (50)	8.1 (0.1)	5410 (50)	8.14 (0.03)	
180345.86−752318.35	DAH	31.95 (0.05)	–	–	5600 (40)	8.03 (0.03)	
180853.83−704231.62	DC	28.1 (0.1)	–	–	4720 (60)	8.02 (0.05)	
180901.95−410140.69	DC	32.01 (0.06)	–	–	5730 (100)	7.9 (0.6)	
181311.31−860811.23	DA	25.90 (0.08)	–	–	4950 (70)	7.95 (0.06)	
181548.96+553232.22	DC:	26.37 (0.05)	–	–	4630 (50)	7.19 (0.04)	
182159.54−595148.52	*DA*	33.16 (0.06)	–	–	4750 (30)	7.27 (0.03)	(c)
182228.37−653738.06	DA	27.88 (0.09)	–	–	5050 (40)	7.96 (0.04)	
183351.29−694203.57	DA	30.39 (0.02)	8120 (50)	7.87 (0.06)	8010 (60)	7.39 (0.02)	
183852.85−441631.32	DA	29.57 (0.09)	5770 (110)	8.5 (0.2)	5560 (100)	8.17 (0.06)	
183856.35−535726.05	DA	28.0 (0.1)	5260 (30)	8.00 (0.04)	5150 (60)	8.04 (0.04)	
184650.69−452139.33	DC	35.6 (0.1)	–	–	4860 (40)	7.92 (0.04)	
184947.86−095744.38	DA	30.61 (0.03)	12 130 (20)	8.24 (0.01)	12 130 (160)	8.05 (0.02)	
185005.58−285117.29	DA	28.31 (0.08)	5700 (180)	8.5 (0.4)	5330 (90)	8.02 (0.07)	
185709.09−265059.22	DA	25.31 (0.06)	7110 (100)	8.2 (0.2)	7020 (60)	7.97 (0.03)	
185934.75−162656.29	DA	25.86 (0.05)	8510 (150)	8.00 (0.05)	8000 (90)	8.0 (0.6)	
190255.35−044012.64	DC	28.6 (0.1)	–	–	4670 (90)	8.03 (0.08)	
190525.34−495625.77	DZ	33.82 (0.02)	–	–	10 920 (120)	8.11 (0.02)	
191100.25−382031.89	DC:	35.7 (0.1)	–	–	4080 (120)	7.68 (0.08)	
191144.26−272954.76	DB	28.87 (0.03)	11 680 (150)	–	11 480 (140)	8.02 (0.03)	
191858.23−434920.40	DC	29.1 (0.1)	–	–	5360 (130)	8.51 (0.07)	
191936.23+452743.55	DC:	35.64 (0.04)	–	–	4780 (20)	7.31 (0.02)	
193538.63−325225.56	DZAH	29.3 (0.1)	–	–	5310 (50)	7.97 (0.04)	
194522.76−490420.23	DC	29.1 (0.1)	–	–	4320 (100)	7.81 (0.08)	
194549.13−153135.63	DA	32.35 (0.03)	12 590 (40)	8.422 (0.008)	12 380 (170)	8.39 (0.02)	
195211.78−732235.48	DC	31.2 (0.3)	–	–	–	–	
195616.36−525819.16	DA	31.30 (0.08)	7670 (620)	8.65 (0.06)	–	–	Not in catalogue
195639.81−511544.83	DC	31.6 (0.1)	–	–	4640 (70)	7.93 (0.06)	
200348.80−474800.18	DA	32.73 (0.06)	6060 (40)	8.07 (0.07)	5920 (50)	7.97 (0.03)	
200707.98−673442.18	DAH	26.00 (0.05)	–	–	7770 (70)	8.33 (0.02)	
201722.68−401043.73	DZA	25.3 (0.1)	–	–	4970 (80)	7.94 (0.0)	
201756.19−124639.44	DC	35.6 (0.1)	–	–	4820 (50)	8.24 (0.04)	
202011.65−382445.66	DA	35.53 (0.05)	7400 (40)	8.44 (0.06)	7290 (70)	8.43 (0.02)	
202016.78−652523.10	DAZ	25.99 (0.07)	–	–	6340 (70)	8.30 (0.03)	
202025.46−302714.65.	DC	57.27 (0.02)	–	–	9930 (110)	8.04 (0.02)	
202030.93−420256.74	DQ	25.02 (0.06)	–	–	6970 (70)	8.02 (0.03)	
202748.03−563031.58	DZ	28.0 (0.1)	–	–	4140 (120)	7.82 (0.09)	
202749.54−430115.21	DC:	47.02 (0.07)	–	–	4880 (40)	8.39 (0.03)	
202837.91−060842.77	DA	28.09 (0.03)	11 860 (100)	8.49 (0.02)	11 340 (290)	8.40 (0.04)	
202956.94−643420.13	DQ	26.79 (0.04)	–	–	7290 (70)	8.03 (0.02)	
204911.00−544617.50	DA	25.48 (0.04)	7670 (30)	8.02 (0.03)	7550 (60)	7.91 (0.02)	

Table 3. Spectral types and parameters of the white dwarf sample (continued)

WD J name	SpT	Parallax (mas)	$T_{\rm eff}$ [K] 3D Spectro	log(*g*) 3D Spectro	$T_{\rm eff}$ [K] Gaia	log(*g*) Gaia	Note
205050.50−612235.61	DA	29.14 (0.05)	7050 (80)	8.28 (0.09)	6960 (70)	8.43 (0.03)	
205213.41−250415.13	DC	55.61 (0.04)	–	–	4910 (20)	7.85 (0.02)	
211240.64−292217.96	*DZQ*	30.49 (0.04)	–	–	9770 (110)	8.11 (0.03)	(w)
212121.30−255716.33	DA	40.78 (0.05)	19 450 (20)	8.11 (0.05)	19 210 (370)	8.07 (0.02)	
212602.02−422453.76	DC:	39.1 (0.3)	–	–	5480 (30)	7.52 (0.03)	
213721.24−380838.22	DC	30.89 (0.06)	–	–	6860 (70)	8.31 (0.03)	
214023.96−363757.44	warm DQ	25.09 (0.05)	–	–	13 190 (230)	8.84 (0.02)	(x)
214324.09−065947.99	DA	55.10 (0.03)	9390 (80)	8.5 (0.06)	8910 (80)	8.42 (0.02)	
214756.59−403527.79	DZQH	35.8 (0.5)	–	–	–	–	(y)
∗ 214810.74−562613.14	DAH	24.98 (0.08)	–	–	5930 (60)	8.08 (0.03)	
220437.98−312713.76	DA	40.69 (0.07)	–	–	4810 (30)	7.92 (0.03)	
220552.11−665934.73	DAH	31.82 (0.05)	–	–	5260 (40)	7.84 (0.03)	
220655.28−600135.32	DA	26.82 (0.08)	–	–	5040 (40)	7.90 (0.04)	
223418.67−553403.40	DC	26.5 (0.1)	–	–	4690 (70)	7.84 (0.05)	
223601.50−554852.02	DZ	31.34 (0.07)	–	–	5130 (40)	8.00 (0.03)	
223607.66−014059.65	DAH	25.63 (0.04)	–	–	10 020 (160)	8.37 (0.03)	
223634.58−432911.11	DA	33.00 (0.04)	6730 (30)	8.02 (0.04)	6240 (40)	7.92 (0.02)	
223700.03−542241.81	DA	33.93 (0.02)	8320 (10)	8.184 (0.008)	8220 (70)	8.01 (0.02)	
225335.70−143828.19	DA	27.4 (0.1)	5500 (30)	8.20 (0.05)	5320 (100)	8.10 (0.07)	
230232.34−330907.96	DC	28.2 (0.1)	–	–	4710 (90)	7.90 (0.07)	
230345.52−371051.56	DZ	30.9 (0.1)	–	–	4270 (90)	7.88 (0.07)	
234300.85−644737.90	DC	26.89 (0.06)	–	–	5800 (50)	7.98 (0.03)	
234935.57−521528.02	DC	32.36 (0.05)	–	–	6250 (60)	8.42 (0.02)	
235419.41−814104.96	DZH	37.10 (0.06)	–	–	4480 (40)	7.77 (0.04)	
235422.99−514930.65	DC:	32.90 (0.08)	–	–	4470 (50)	7.81 (0.03)	

due to a complex field geometry, and has the largest *Gaia* photometric surface gravity of any white dwarf in the sample. Even from the higher resolution X-Shooter observations, the line cores have round shapes and do not show evidence of multiple sub-components.

WD J0317−8532B is a 1.27 ± 0.02 $M_\odot$ DAH which has a very high field strength of ≈ 340 MG (Barstow et al. 1995), and is part of a wide double-degenerate binary system with a DA companion, **WD J0317−8532A**. This system has been studied extensively pre-*Gaia*, as **WD J0317−8532B** is potentially a double-degenerate merger product due to its large mass (Ferrario et al. 1997; Külebi et al. 2010). We have calculated the *Gaia* best-fit parameters of the two components of this binary system (see Table 3), and have used these to determine the total ages of both stars (Hurley et al. 2000; Cummings et al. 2018; Bédard et al. 2020). The total age of the DAH **WD J0317−8532B** is 315 ± 80 Myr, and the total age of the companion is 450 ± 40 Myr, where errors are statistical and likely underestimated, especially for the hot magnetic component. These total ages are in agreement within 2σ with single-star evolution for both objects. A merger could cause a cooling delay, such that the magnetic star would appear younger than its companion, and we cannot rule this out for **WD J0317−8532B** if there is a moderate cooling delay of the order of 200 Myr.

WD J1706−2643 was observed by Bagnulo & Landstreet (2021) who detected a field strength of 8 MG. The field strengths of the remaining DAH white dwarfs have been estimated by visual comparison with theoretical λ-B curves (Friedrich et al. 1996) and are displayed in Table 4. Uncertainties in field strength are estimated based on the width of the Zeeman split lines.

WD J2236−0140 is magnetic, but its field strength cannot be well-constrained from the limited number of spectral features. There is a broad feature at ≈ 4400–4600 Å. There is also a narrower, stationary component at 4140 Å. The field strength is estimated to be $250 < B < 750$ MG from

Table 4. Magnetic field strengths for newly identified magnetic white dwarfs in the 40 pc sample

WD J name	SpT	⟨*B*⟩ (MG)
001349.89−714954.26	DAH	0.4 (0.2)
001830.36−350144.71	DAH	6.8 (0.4)
∗ 014240.09−171410.85	DAH	15.1 (0.2)
025245.61−752244.56	DAH	22 (3)
035531.89−561128.32	DAH	2.3 (0.2)
042021.33−293426.26	DAH	0.4 (0.2)
050552.46−172243.48	DAH	3.9 (0.2)
∗ 054858.25−750745.20	DZH	1.1 (0.2)
075328.47−511436.98	DAH	19 (2)
075447.40−241527.71	DAH	10.5 (0.2)
090212.89−394553.32	DAH	21 (1)
091808.59−443724.25	DAH	0.4 (0.2)
094240.23−463717.68	DAH	3.4 (0.2)
101947.34−340221.88	DAH	110 (10)
103706.75−441236.96	DAH	0.3 (0.1)
104646.00−414638.85	DAH	3.6 (0.2)
113216.54−360204.95	DZH	0.25 (0.02)
121456.38−023402.84	DZH	2.1 (0.2)
140115.27−391432.21	DAH	7.7 (0.5)
141220.36−184241.64	DAH	21 (3)
162558.78−344145.71	DAH	4.0 (0.2)
171436.16−161243.30	DAH	55 (7)
171652.09−590636.29	DAH	0.7 (0.2)
180345.86−752318.35	DAH	0.2 (0.2)
193538.63−325225.56	DZAH	0.10 (0.01)
200707.98−673442.18	DAH	6.4 (0.2)
∗ 214810.74−562613.14	DAH	12.4 (0.4)
220552.11−665934.73	DAH	2.2 (0.3)
223607.66−014059.65	DAH	> 250
235419.41−814104.96	DZH	0.6 (0.2)

Notes: Objects with an asterisk before their name have a parallax value outside of 40 pc but may still be within that volume at $1\sigma_\varpi$.

Table 5. Atmospheric parameters and chemical abundances of DB white dwarfs, with fixed log(g) determined from photometric fitting.

WD J name	$T_{\rm eff}$ [K] (Spectro)	log(g) (*Gaia*)	log(H/He)
1325−6015	11550 (120)	7.98 (0.02)	−5.03 (0.08)
1911−2729	11680 (150)	8.02 (0.02)	−5.5 (0.3)

Note: All quoted uncertainties represent the intrinsic fitting errors. We recommend adding systematics of 1 per cent in $T_{\rm eff}$ to account for data calibration errors.

these components, although H α spectroscopy is needed to confirm this.

Fig. A8 shows seven magnetic metal-polluted white dwarfs. **WD J2354−8141** and **WD J1132−3602** show splitting of the Ca II H line into two groups of two, and the Ca II K line into six because of the large spin-orbit effect for the 4p state of Ca II (Kawka & Vennes 2011). **WD J0916−4215** is potentially a highly magnetic DZH white dwarf with complex splitting of its spectral features. The field strengths of new DZH white dwarfs have been estimated and are displayed in Table 4. **WD J1935−3252** is weakly magnetic (100 kG) with spectral type DZAH.

The lower limit of detectable magnetic field strength depends on the object; the best case for a magnetic field detection is for an object with very narrow Ca lines and a high signal-to-noise. In this case, we find that field strengths of less than ≈ 50 kG cannot be detected using X-Shooter spectroscopy.

For all magnetic white dwarfs, we estimate field strengths in Table 4 from Zeeman splitting but do not derive spectroscopic atmospheric parameters, which is notoriously difficult (Külebi et al. 2009). Spectropolarimetry is required to determine the magnetic status of the remaining newly observed white dwarfs which do not display Zeeman splitting, a recent effort has been made towards this by Bagnulo & Landstreet (2022) for young white dwarfs in 40 pc.

WD J0812−3529 has been classified as a DC in this work from a Goodman spectrum. Bagnulo & Landstreet (2020) classify it as a DAH with a field strength of 30 MG, determined from their high-quality spectropolarimetric observations.

4.3 DB white dwarfs

The spectra for the two DB white dwarfs we observe are shown in Fig. A4. We derive the $T_{\rm eff}$ of these white dwarfs using 3D model atmospheres (Cukanovaite et al. 2021), and parameters are displayed in Table 5. These are in reasonable agreement with *Gaia* values. These white dwarfs are at the cool end of the DB range, where spectroscopic fits are difficult (Koester & Kepler 2015; Rolland et al. 2018). We therefore fix log(g) to that determined from *Gaia* photometry.

4.4 DC white dwarfs

The spectra of 69 DC white dwarfs are shown in Fig. A5. Nineteen of these were observed with the Goodman or FAST spectrographs, which both only provide spectra in the optical blue range 3000–6000 Å such that H α coverage is missing from the data. This is often the only diagnostic line for DA white dwarfs with low temperatures. Therefore, further spectroscopy may reveal that a subset of these DC systems are in fact DA white dwarfs. The coolest DA in the sample that was observed with Goodman is **WD J1317−5438**, which has a $T_{\rm eff}$ of ≈ 5800 K. For white dwarfs below ≈ 5600 K, the resolution and typical signal-to-noise ratio achieved with Goodman are not high enough to detect the H β line. Therefore the eleven optical blue-only DC with temperatures above 5600 K are likely to be genuine DC as we would see the H β line if they were DA. The remaining eight DC with lower temperatures could have unobserved H α lines, and require further observations. These are classified as tentative DC (DC: spectral type in Table 3).

Three new white dwarf candidates from the north, **WD J1815+5532**, **WD J1919+4527**, and **WD J1318+7353**, are all confirmed as white dwarfs spectroscopically. They are classified as tentative DC (DC:) as their OSIRIS spectra are noisy, and potential spectral features cannot be excluded.

On the *Gaia* HR diagram (see Fig. 4), **WD J1952−7322** is shown to have the faintest absolute *Gaia* G-band magnitude for any DC white dwarf within 40 pc. The spectrum of **WD J1952−7322** displays hints of mild optical collision-induced absorption (CIA), which would be consistent with a mixed H and He atmospheric composition and IR-faint categorisation (Bergeron et al. 2022). Only *Gaia* photometry is available for this white dwarf, so its parameters cannot be constrained given the degeneracy between log(H/He) and $T_{\rm eff}$ with such broad band-passes. **WD J1630−2818** shows signs of mild optical CIA in its spectrum. For both of these white dwarfs, we therefore do not infer $T_{\rm eff}$ and log(g) from *Gaia* photometry.

WD J1147−7457 is a potential ultra-cool (< 4000 K) DC white dwarf and a candidate halo white dwarf, as it has a tangential velocity of ≈ 160 km/s.

WD J1604−7203 is a low-probability ($P_{\rm WD} = 0.28$) white dwarf candidate in the Gentile Fusillo et al. (2021) catalogue. It has a *Gaia* photometric log(g) of 6.75, and a $T_{\rm eff}$ of 4090 K, when fitted as a single star. This object is likely a double degenerate system (see Section 5.5 for discussion).

There are Ca II H+K emission features in the spectrum of **WD J0519−7014** which are not associated with the white dwarf and are due to less than ideal sky subtraction as the result of contamination from the Large Magellanic Cloud. This white dwarf is still classified as a DC, as these emission features are not from the star itself.

4.5 DAZ white dwarfs

Fig. A6 shows the spectra of ten DAZ white dwarfs. **WD J0358+2157** (reported in Paper I) and **WD J0426−4153** are both highly metal-polluted DAZ white dwarfs that will have a dedicated analysis in a future study (Cutolo et al., in prep.), and therefore no spectral fits are presented here.

We fit the other eight DAZ stars using the combined photometry and spectroscopy method of Koester (2010). The fitting of $T_{\rm eff}$ and log(g) relies on photometry from *Gaia*, GALEX (Martin et al. 2005), PanSTARRS (Chambers et al. 2016), SkyMapper (Schmidt et al. 2005), 2MASS (Skrutskie et al. 2006) and WISE (Wright et al. 2010). Not all photom-

Table 6. Atmospheric parameters and chemical abundances of newly observed DAZ white dwarfs, where $T_{\rm eff}$ and log(g) have been determined from a combination of spectroscopic and photometric fitting.

WD J name	$T_{\rm eff}$ [K]	log(g)	log(Ca/H)
0143−6718	6230 (10)	7.91 (0.01)	−11.05
0343−5125	6710 (10)	7.99 (0.01)	−9.60
0445−4232	6650 (10)	7.92 (0.01)	−10.70
0626−1850	7280 (10)	7.96 (0.01)	−10.50
0917−4546	6260 (10)	7.97 (0.01)	−10.30
1059−2819	6530 (10)	7.99 (0.01)	−9.30
1530−6203	5860 (10)	8.15 (0.02)	−11.00
2020−6525	6120 (10)	8.20 (0.02)	−10.65

Note: All quoted uncertainties represent the intrinsic fitting errors. We recommend adding systematics of 1 per cent in $T_{\rm eff}$ to account for data calibration errors.

etry was available for every object. The best-fit parameters, including log(Ca/H) abundances, of the remaining 8 DAZ white dwarfs are displayed in Table 6.

4.6 DZ and DZA white dwarfs

We show 24 DZ, DZA, DZH and DZAH white dwarf spectra in Figs. A7–A9. We fit the combined spectroscopy and photometry for 19 of these objects. **WD J0548−7507** and **WD J2354−8141** are DZH white dwarfs and are not fitted due to the complexity of the splitting of their lines. We also do not fit the potentially high-field DZH **WD J0916−4215**. The X-Shooter spectra of **WD J2147−4035** and **WD J1214−0234** have already been fitted by Elms et al. (2022) and Hollands et al. (2021), respectively. In this section, we discuss all DZ and DZA white dwarfs for which we fit their combined spectroscopy and photometry using the model atmosphere code of Koester (2010).

The fitting of $T_{\rm eff}$ and log(g) relies on photometry from *Gaia*, GALEX, PanSTARRS, SkyMapper, 2MASS and WISE. Not all photometry was available for every object. We detect Ca in all DZ and DZA spectra in our sample.

WD J1057−0413, **WD J1217−6329**, **WD J1905−4956**, and **WD J2236−5548** are DZ white dwarfs with He-dominated atmospheres where no H is detected. Ca was detected in the atmosphere of **WD J1057−0413** by Coutu et al. (2019), and we additionally detect Mg and Fe in this white dwarf. **WD J2236−5548** is a cool DZ which shows strong metal lines and has a He-dominated atmosphere, we have constrained abundances for five metals: Ca, Na, Mg, Fe, and Cr (See Fig. 3 for fit).

WD J0044−1148, **WD J0554−1035**, **WD J1241−2434**, and **WD J1333−6751** are all DZ white dwarfs with He-dominated atmospheres and trace H that is inferred indirectly from their spectra. There is no visible H α line in these spectra, however we observe narrow and sharp metal lines. The electron density in the atmosphere, and therefore the opacity of the atmosphere, is significantly increased by the presence of H which causes the metal lines to appear narrower. **WD J0044−1148** has a companion separated by a few arcseconds (see Table 10). **WD J0554−1035** was identified as a DZ with Ca in Paper I; we also measure the log(H/He) abundance that was not previously constrained. There is a blend of Fe lines in the spectra of **WD J1241−2434** and **WD J1333−6751**.

WD J0818−1512, **WD J1132−3602**, **WD J2027−5630**, and **WD J2303−3710** have very narrow Ca lines, indicating a H-dominated atmosphere. Therefore their abundances presented in Table 7 are in relation to hydrogen, despite their spectral classification of DZ. There is Zeeman splitting in the spectrum of **WD J1132−3602** which indicates a magnetic field of about 280 kG, which has been accounted for in the modelling. **WD J2027−5630** is a potential ultra-cool DZ, with a combined spectroscopic and photometric $T_{\rm eff}$ of around 3700 K.

WD J0808−5300, **WD J0850−5848**, **WD J1141−3504**, **WD J1410−7510**, **WD J1540−4858**, **WD J1935−3252**, and **WD J2017−4010** are DZA white dwarfs with sharp metal lines and a very narrow H α line, indicating nearly pure-H atmospheres (Fig. A9).

WD J0850−5848 has a high photometric log(g) of ≈ 8.9 when using mixed H/He models, and a combined spectroscopic and photometric log(g) of ≈ 8.7. We infer a white dwarf mass of 1.045 ± 0.005 $M_{\odot}$, and a progenitor mass of 5.4 ± 0.1 $M_{\odot}$ (Cummings et al. 2018). The spectrum of **WD J0850−5848** does not indicate the presence of CIA, so we infer that this is indeed a massive white dwarf, and is among the most massive metal-polluted white dwarfs ever observed.

WD J1410−7510 and **WD J1540−4858** both display sharp Fe lines. The DZAH **WD J1935−3252** displays strong metal lines from four elements: Ca, Mg, Fe and Al, and has a weak magnetic field of 100 kG (see Fig. 3 for fit).

WD J0808−5300 displays atmospheric CIA of H_2–H_2 and H_2–H, seen in infrared photometry from 2MASS and WISE. This white dwarf is polluted by Ca, Na, Mg, Fe, Al and Cr. We detect an absorption feature caused by MgH molecules at around 5200 Å, a feature that has been detected in white dwarfs with mixed H/He atmospheres (Blouin et al. 2019a; Kaiser et al. 2021). To our knowledge, we have made the first detection of MgH in a H-dominated atmosphere white dwarf. The hybrid fit to this white dwarf is shown in Fig. 3.

The abundances of Li, Na, Mg, K, Ca, Cr and Fe for the DZH white dwarf **WD J1214−0234** are calculated in Hollands et al. (2021) using the X-Shooter spectrum shown in Fig. A8.

4.7 DQ white dwarfs

We observed nine DQ white dwarfs (Fig. A10). We fitted all objects with the Koester (2010) model atmosphere code using an iterative procedure. Results from the fitting procedure are in Table 8. The fitting of $T_{\rm eff}$ and log(g) relies on photometry from *Gaia*, GALEX, SkyMapper and 2MASS. Not all photometry was available for every object.

Two of the DQ white dwarfs in the sample, **WD J0801−2828** and **WD J1636−8737**, display CH molecular absorption features in their spectra near 4300 Å. We classify **WD J0801−2828** and **WD J0817−6808** as peculiar DQ (DQpec) white dwarfs. This classification describes cool DQ below 6000 K with molecular absorption bands with central wavelengths that have been shifted 100–300 Å from the positions of the C_2 Swan bands (Hall & Maxwell 2008). The warm DQ **WD J2140−3637** is discussed further in Section 5.3.

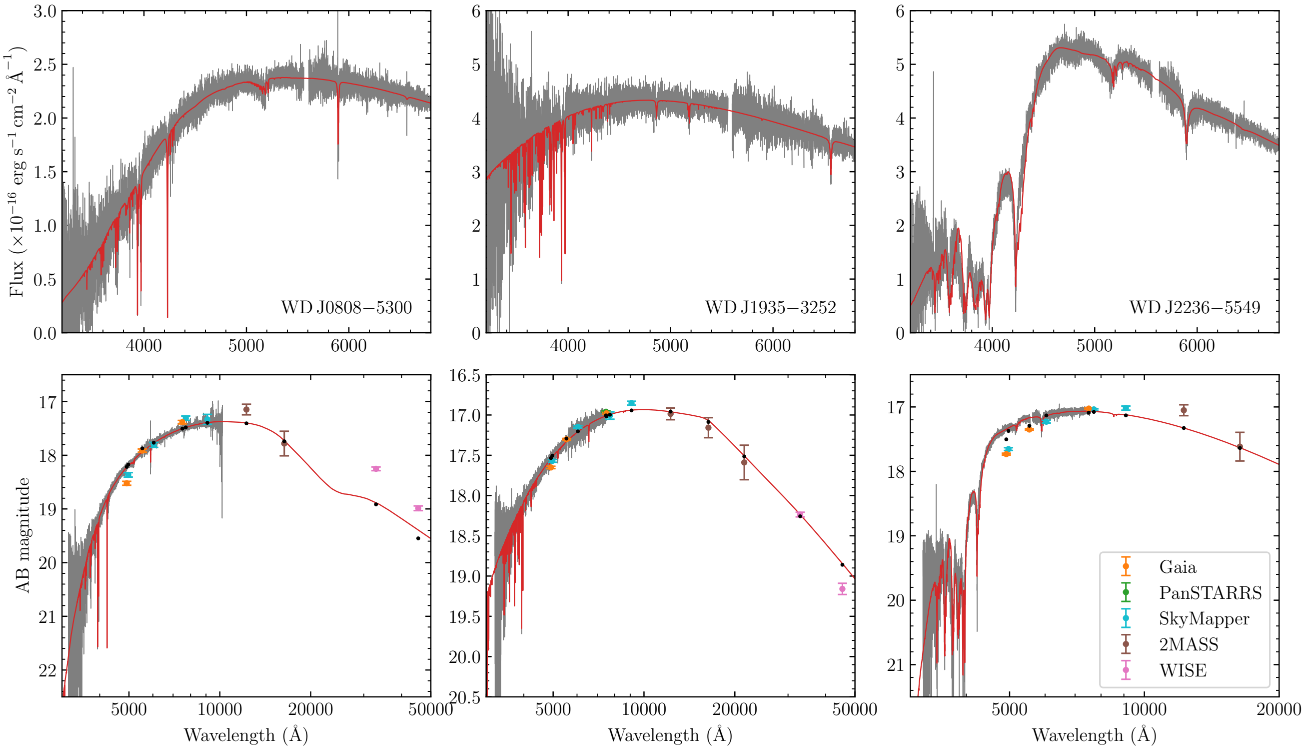

Figure 3. Simultaneous fits of spectroscopy and photometry for three metal-rich DZ and DZA white dwarfs: **WD J0808−5300** (left panels), **WD J1935−3252** (middle panels) and **WD J2236−5549** (right panels). The top row of panels compare our best fit models to normalised spectroscopic observations. The spectroscopic observations are re-calibrated onto the models but are still in physical flux units. The bottom panels compare our best fit models to catalogue photometry over a wider wavelength range than the available spectroscopy provides.

Table 7. Atmospheric best-fit parameters and chemical abundances of DZ and DZA white dwarfs, where $T_{\rm eff}$ and log(g) have been determined from a combination of spectroscopic and photometric fitting. Weakly magnetic DZH and DZAH are also fitted. Upper table: Best-fit parameters for white dwarfs with He-dominated atmospheres. Lower table: Best-fit parameters for white dwarfs with H-dominated atmospheres.

WD J name	SpT	$T_{\rm eff}$ [K]	log(g)	log(H/He)	log(Ca/He)	log(Na/He)	log(Mg/He)	log(Fe/He)	log(Cr/He)
0044−1148	DZ	5310 (30)	7.99 (0.02)	−1.23 (0.03)	−11.53 (0.04)	–	–	–	–
0554−1035	DZ	6230 (20)	8.04 (0.01)	−4.52 (0.05)	−11.78 (0.03)	–	–	–	–
1057−0413	DZ	6500 (20)	8.03 (0.01)	–	−10.30 (0.01)	–	−8.88 (0.02)	−9.60 (0.03)	–
1217−6329	DZ	7420 (80)	7.96 (0.03)	–	−10.43 (0.05)	–	–	–	–
1241−2434	DZ	6310 (30)	8.13 (0.01)	−2.78 (0.04)	−11.42 (0.01)	–	–	−10.29 (0.03)	–
1333−6751	DZ	5640 (60)	8.17 (0.03)	−1.97 (0.02)	−11.41 (0.03)	–	–	−10.62 (0.04)	–
1905−4956	DZ	10 600 (40)	8.08 (0.01)	–	−8.99 (0.03)	–	–	–	–
2236−5548	DZ	5350 (10)	8.17 (0.01)	–	−9.17 (0.01)	−9.16 (0.01)	−7.41 (0.01)	−8.64 (0.01)	−9.9 (0.1)

WD J name	SpT	$T_{\rm eff}$ [K]	log(g)	log(Ca/H)	log(Na/H)	log(Mg/H)	log(Fe/H)	log(Al/H)	log(Cr/H)
0808−5300	DZA	4910 (10)	8.34 (0.01)	−9.74 (0.02)	−9.60 (0.02)	−8.16 (0.02)	−9.05 (0.03)	−9.54 (0.03)	−10.48 (0.03)
0818−1512	DZ	4720 (10)	7.68 (0.01)	−11.50 (0.04)	–	–	–	–	–
0850−5848	DZA	5430 (20)	8.73 (0.01)	−10.65 (0.01)	–	–	–	–	–
1132−3602	DZH	4990 (10)	8.12 (0.01)	−10.84 (0.03)	–	–	–	–	–
1141−3504	DZA	4880 (20)	8.07 (0.01)	−11.11 (0.02)	–	–	–	–	–
1410−7510	DZA	5180 (10)	8.011 (0.007)	−10.64 (0.01)	–	–	−9.36 (0.02)	–	–
1540−4858	DZA	5000 (30)	8.10 (0.02)	−10.57 (0.03)	–	–	−9.77 (0.03)	–	–
1935−3252	DZAH	5430 (10)	8.00 (0.01)	−9.68 (0.02)	–	−7.89 (0.03)	−8.61 (0.02)	−9.12 (0.04)	–
2017−4010	DZA	5250 (20)	8.08 (0.01)	−10.62 (0.03)	–	–	–	–	–
2027−5630	DZ	3750 (130)	7.7 (0.1)	−12.6 (0.1)	–	–	–	–	–
2303−3710	DZ	4790 (50)	8.28 (0.03)	−10.76 (0.06)	–	–	–	–	–

Note: All quoted uncertainties represent the intrinsic fitting errors. We recommend adding systematics of 1 per cent in $T_{\rm eff}$ to account for data calibration errors.

4.8 DQZ and DZQ white dwarfs

WD J1514−4625 and **WD J1519−4854** are classified as DQZ, and **WD J2112−2922** is classified as DZQ. All three show both carbon absorption features and metal lines in their spectra (see Fig. A11). In all three cases, we detect metals from the Ca II H+K lines, and carbon from the C_2 Swan bands. The field of view of the Goodman spectrograph is 10 arcmin, and **WD J1514−4625** and **WD J1519−4854** were both observed by Goodman and are separated by over a degree on the sky, so they are not a duplicate observation. These stars are unlikely to be DQ + DZ binaries, as all three stars have photometric log(g) values close to or above the canonical value of 8.0 for single stars. Elms et al. (2022) make a tentative detection of carbon in the ultra-cool DZ **WD J2147−4035**; this star would notionally be a DZQpecH (Fig. A8). These objects are discussed further in Section 5.2.

4.9 Main-sequence stars

Fig. A12 shows two white dwarf candidates with $P_{\rm WD}$ equal to 1 from Gentile Fusillo et al. (2021) that turned out to be main-sequence stars following spectroscopic observations: **WD J0924−1818** and **WD J1732−1710**. The issues of contamination from *Gaia* DR2 white dwarf samples (Gentile Fusillo et al. 2019) have mostly been solved in DR3 (Gentile Fusillo et al. 2021), such that there are now minimal contaminant sources in our sample (< 1 per cent of this 40 pc south sample has main-sequence contaminants). It is likely that these sources have spurious *Gaia* parallaxes which places them on the white dwarf sequence of the HR diagram, hence their high $P_{\rm WD}$ values. Both stars have high excess flux error values in *Gaia*, indicating either variability or issues with photometry.

5 DISCUSSION

5.1 Comparison with the overall 40 pc sample

The *Gaia* DR3 HR diagram for the volume-limited 40 pc spectroscopic white dwarf sample is shown in Fig. 4. The faintest and reddest white dwarf in the sample is **WD J2147−4035**, at the bottom right of Fig. 4 (Elms et al. 2022).

The mean *Gaia* photometric $T_{\rm eff}$ of our sub-sample of 246 white dwarfs presented in this work is 6930 K, whereas for the full 40 pc sample the mean *Gaia* $T_{\rm eff}$ is 7530 K. Both samples have a standard deviation of ≈ 3000 K. We expect our sub-sample to have a lower mean $T_{\rm eff}$ than in 40 pc overall because our new observations are biased towards fainter white dwarfs at lower $T_{\rm eff}$ that had not previously been observed spectroscopically.

The mean *Gaia* photometric mass of both our sub-sample and the overall 40 pc sample is 0.63 $M_\odot$. The mean mass is biased by the cool white dwarfs with $T_{\rm eff}$ < 5000 K for which masses may have been incorrectly calculated from models (see Fig. 1). The mean mass for white dwarfs with $T_{\rm eff}$ > 5000 K is 0.66 $M_\odot$ (Paper II).

Within this work, we have a sample of 179 white dwarfs observed with X-Shooter. This X-Shooter sample provides a set of white dwarf spectra with a large wavelength coverage and high signal-to-noise ratio. Metal-polluted, carbon-rich,

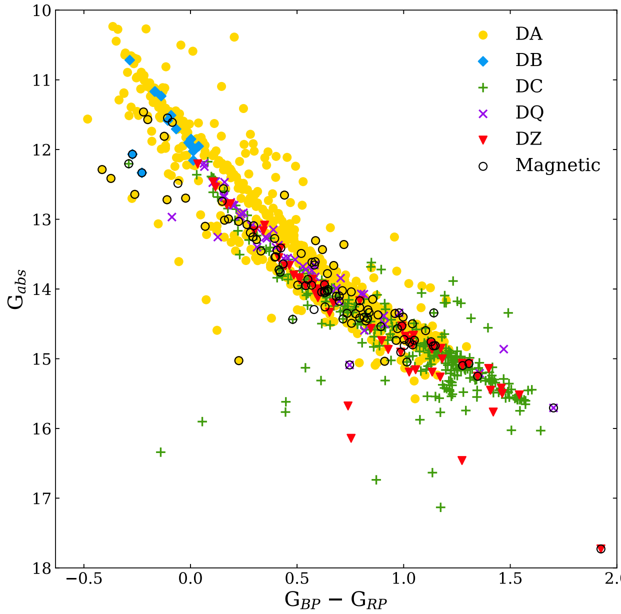

Figure 4. A *Gaia* DR3 Hertzsprung-Russell (HR) diagram for the full spectroscopic 40 pc sample of 1058 white dwarfs. Magnetic stellar remnants have black contours. Data are colour- and symbol-coded by their primary spectral type classification only, for simplicity.

and magnetic white dwarfs are over-represented in this X-Shooter sub-sample compared to the remaining 40 pc white dwarfs (not including those observed with X-Shooter), as shown in Fig. 5. An over-abundance of magnetic and of metal-polluted white dwarfs may be due to the resolution of X-Shooter, a medium-resolution spectrograph, compared to the observations for the existing 40 pc sample, providing us with the opportunity to detect low levels of metal abundances and weaker Zeeman splitting. Since our X-Shooter sub-sample is biased towards lower $T_{\rm eff}$, there might also be a greater incidence of metal-pollution, trace carbon and magnetism due to this bias. It is critical to obtain higher resolution and quality spectra of 40 pc white dwarfs to update fractions of metal-polluted and magnetic white dwarfs and determine the underlying distributions for this volume-limited sample.

Using Keck HIRES high-resolution spectra, Zuckerman et al. (2003) observed that 25 per cent of DA white dwarfs with $T_{\rm eff}$ below 10 000 K were metal-polluted. In our 40 pc south sub-sample, we observe a metal-pollution rate of around 15 per cent for DA white dwarfs with $T_{\rm eff}$ below 10 000 K. It is possible that we do not see such a high fraction of polluted white dwarfs as reported in Zuckerman et al. (2003) due to the intrinsic fainter nature of our sub-sample. Our sub-sample also uses medium-resolution spectroscopy rather than high-resolution, so less metal lines will be detected.

5.2 Metal-polluted DQ White Dwarfs

Both Coutu et al. (2019) and Farihi et al. (2022) observe a significant deficit in the frequency of metal pollution in DQ stars, and observe only a 2 per cent pollution rate in DQs.

Table 8. Atmospheric parameters and chemical abundances of DQ, DQZ and DZQ white dwarfs. $T_{\rm eff}$ and log(g) have been determined from iterative spectroscopic and photometric fitting. The warm DQ **WD J2140−3637** is not included here, as we assume it has a C-dominated atmosphere when fitting, rather than a He-dominated atmosphere (see Section 5.3).

WD J name	SpT	$T_{\rm eff}$ [K]	log(g)	log(C/He)	log(H/He)	log(Ca/He)
0801−2828	DQpec	5970 (10)	7.96 (0.01)	−5.90 (0.01)	−4.25	–
0817−6808	DQpec	4620 (20)	8.02 (0.02)	−7.70 (0.01)	–	–
0936−3721	DQ	8890 (20)	7.96 (0.01)	−4.94 (0.02)	–	–
1245−4913	DQ	8120 (20)	7.94 (0.01)	−5.30 (0.02)	–	–
1327−2817	DQ	7510 (50)	7.90 (0.02)	−5.74 (0.01)	–	–
1424−5102	DQ	6340 (30)	7.98 (0.01)	−7.45 (0.01)	–	–
1514−4625	DQZ	7470 (20)	7.99 (0.01)	−5.96 (0.02)	–	−11.7
1519−4854	DQZ	8960 (20)	8.06 (0.01)	−4.60 (0.02)	–	−11.6
1636−8737	DQ	5370 (40)	8.11 (0.02)	−7.60 (0.01)	−3.40	–
2020−4202	DQ	6870 (30)	7.99 (0.01)	−6.6 (0.2)	–	–
2029−6434	DQ	7120 (20)	7.97 (0.01)	−6.30 (0.01)	–	–
2112−2922	DZQ	8960 (40)	7.87 (0.01)	−4.80 (0.01)	–	−11.6

Note: All quoted uncertainties represent the intrinsic fitting errors. We recommend adding systematics of 1 per cent in $T_{\rm eff}$ to account for data calibration errors.

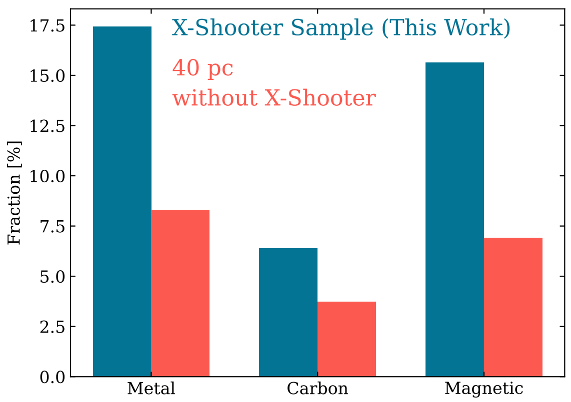

Figure 5. Incidence of different atmospheric compositions between a sample of 179 X-Shooter observations presented in this work, and the full 40 pc sample not including X-Shooter observations. We consider white dwarfs with trace metals in their atmospheres, carbon in their atmospheres, and magnetic white dwarfs.

To explain this deficit, Hollands et al. (2022) and Blouin (2022) model the effect of metal pollution on the presence of Swan bands in DQ white dwarf spectra, and show that for above a relatively low level of pollution, Swan bands will be suppressed such that a DQZ would present as a DZ. Therefore, the only metal-polluted DQ stars that can be observed spectroscopically should have relatively low levels of pollution (Blouin 2022), which aligns with what we observe in the 40 pc sample. Another explanation for this observed deficit is that DQ white dwarfs at all temperatures are the product of binary evolution, altering their circumstellar environments and reducing the occurrence of planetary debris (Farihi et al. 2022).

Thirty per cent of the white dwarf population in 40 pc have He-rich atmospheres, and DZ and DQ white dwarfs independently correspond to about 18 per cent of those white dwarfs with He-rich atmospheres. If the presence of carbon and metals in white dwarfs are independent of each other, the percentage of He-rich white dwarfs in a volume-limited sample with both metal and carbon lines should be about 3 per cent. Therefore in 40 pc we expect to find 8 ± 3 metal-polluted DQ white dwarfs.

The white dwarf **WD J0916+1011** is classified as a DQZ by Kleinman et al. (2013) and is at a distance of 38.6 pc. **WD J2147−4035** is a white dwarf with spectral type DZQH (Elms et al. 2022) and its spectrum is presented in Fig. A8. The white dwarf **Procyon B** is not in the *Gaia* DR3 catalogue, however it is at a distance of ≈ 3.5 pc and was classified as a DQZ following the detection of Mg lines in its UV spectrum (Provencal et al. 2002).

Adding **Procyon B**, **WD J0916+1011** and **WD J2147−4035** to the two newly observed DQZ white dwarfs and the DZQ in this paper gives six out of 253 He-rich white dwarfs in the 40 pc sample that display both metal lines and carbon lines. We therefore do not detect a notable deficit in the numbers of these white dwarfs, but we note that the numbers are too small to draw meaningful conclusions. Coutu et al. (2019) use a sample of SDSS spectra which have lower signal-to-noise than the X-Shooter and Goodman spectra in our sample, possibly explaining why they see less metal-pollution in DQs, or Swan bands in DZs, than we observe in 40 pc, potentially missing those stars with very weak Swan bands and stronger metal features such as **WD J2112−2922**.

5.3 WDJ2140-3637: A warm DQ white dwarf

WD J2140−3637 is a warm DQ white dwarf that has been previously identified in Bergeron et al. (2021). Warm DQ white dwarfs have spectra dominated by C I lines in the optical, and tend to have He-dominated atmospheres (Koester & Kepler 2019) compared to the C/O-dominated magnetic hot DQ white dwarfs at $T_{\rm eff} > 18\,000$ K (Dufour et al. 2007). Bergeron et al. (2021) showed that **WD J2140−3637** belongs to a massive warm DQ white dwarf sequence identified by Coutu et al. (2019) and they state that it has the largest carbon abundance of any warm DQ.

We observe an O I triplet absorption feature at 7772,

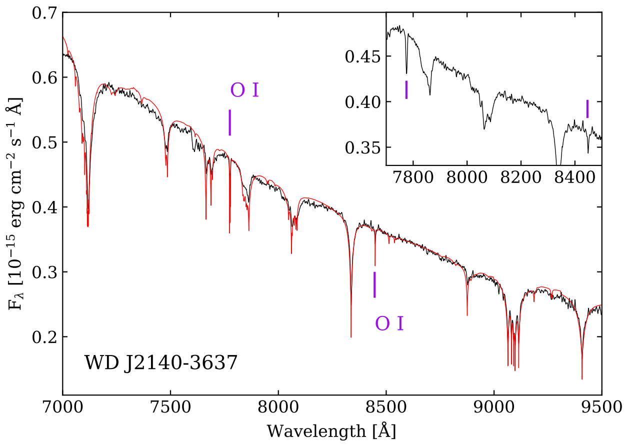

Figure 6. X-Shooter spectrum of **WD J2140−3637** plotted with the combined photometric and spectroscopic fit using Koester (2010) models. The O I absorption features around 7775 Å and 8446 Å are highlighted with purple ticks. The spectrum is convolved by a Gaussian with a FWHM of 1 Å and shifted by 45 km/s. An inset plot shows the region around the oxygen absorption features.

7774, and 7775 Å, and an O I feature around 8446 Å, which are labelled in Fig. 6. As with atmospheric carbon, the presence of oxygen in the atmosphere of **WD J2140−3637** is likely due to dredge-up by an extending convection zone in the upper helium layer of a CO-core white dwarf with small total masses of H and He. We have made the first detection of oxygen in the atmosphere of **WD J2140−3637**.

We fit this object using the same models as for the other DQ stars in this sample (Koester 2010), and find $T_{\rm eff}$ = 11 800 ± 200 K and log(g) = 8.77 ± 0.01. Assuming carbon is the dominant atmospheric element, we estimate the following abundances: log(H/C) < −3.50, log(He/C) < 1.00, log(N/C) < −2.50, log(O/C) = −2.10 ± 0.10. The limit for He due to an absence of spectral features means we cannot exclude that He is more abundant than C. Therefore this white dwarf is potentially the first warm non-magnetic DQ which has a carbon-dominated atmosphere.

Warm DQ white dwarfs may be the cooled down counterparts of hot DQ stars, which are thought to originate from double CO-core white dwarf mergers (Dunlap & Clemens 2015; Williams et al. 2016; Cheng et al. 2019; Coutu et al. 2019). The mass of **WD J2140−3637** determined from our fitting is 1.06 ± 0.01 $M_\odot$.

5.4 Comparison of DA Spectroscopic and Photometric Parameters

For the homogeneous sub-sample of DA white dwarfs with X-Shooter spectroscopy, Fig. 7 displays the differences in $T_{\rm eff}$ of the spectroscopic fitting method adopted in this paper compared to *Gaia* photometric parameters. There is no clear systematic differences for DA white dwarfs above 8000 K due to low number statistics. We observe a clear systematic offset between X-Shooter spectroscopic solutions and *Gaia* photometric parameters in the region 6000 < $T_{\rm eff}$ < 8000 K, where *Gaia* photometric temperatures are systematically lower by 1.5 ± 0.8 per cent (see Fig. 7). The region $T_{\rm eff}$ < 6000 K is excluded because there is a known issue with photometric fits for these low-temperature white dwarfs (see Fig. 1).

In Paper I, using a different spectroscopic data set from WHT for a similar sample of cool DA white dwarfs within 40 pc, a similar offset was found between spectroscopic and photometric temperatures. It was concluded that *Gaia* colours are systematically too red, or the spectroscopic solutions too warm. Radius measurements using *Gaia* photometry and astrometry depend on a comparison between observed and predicted absolute magnitude, the latter itself a function of $T_{\rm eff}$. Therefore, an under-prediction of photometric $T_{\rm eff}$ would result in an over-prediction of radius, hence a systematic decrease in log(g) given the mass-radius relation. As a consequence, any systematic offset in log(g) values between both techniques is in part a consequence of the offset in $T_{\rm eff}$.

In summary, from this work and the recent literature (Genest-Beaulieu & Bergeron 2019; Tremblay et al. 2019; Cukanovaite et al. 2021, Paper I), there is a clear offset between photometric and spectroscopic $T_{\rm eff}$ solutions for DA white dwarfs that is present when using different homogeneous spectroscopic data sets (e.g. WHT, X-Shooter, SDSS) and photometric data sets (e.g. *Gaia* DR2 and DR3, Pan-STARRS, SDSS). This offset appears to be of a similar percentage for temperatures between 5500 K and 30 000 K, where the 1.5 per cent value found in this work is very similar to the offset found for warm non-convective ($T_{\rm eff}$ > 15 000 K) DA white dwarfs from SDSS in Tremblay et al. (2019). Finally, a similar offset is seen for DB white dwarfs (Cukanovaite et al. 2021).

5.5 Binary Systems and Binary Candidates

Table 9 lists all new candidate unresolved binary systems in our 40 pc south sub-sample, where we selected objects with *Gaia* log(g) < 7.72 when fitted as single stars. A white dwarf with a mass lower than ≈ 0.50 $M_\odot$ (log(g) ≲ 7.80) could not have formed through single-star evolution within the age of the universe, therefore these low log(g) solutions indicate binarity. We do not include very cool white dwarfs that are significantly below $T_{\rm eff}$ = 4500 K in our candidate list, as they have a low-mass problem such that low log(g) values for some of these stars may not indicate binarity (Paper II). We do not consider the DZ (**WD J0818−1512**) and DQ (**WD J1327−2817**) stars that have low photometric log(g) values from their pure-He or mixed H/He atmosphere fits (Gentile Fusillo et al. 2021) to be candidate binary systems, as their combined spectroscopic and photometric fits including metals/carbon in Tables 7 and 8 increase their log(g) values significantly.

In Paper II, a system is also considered a candidate unresolved binary when the difference between the spectroscopic and photometric log(g) values is greater than 0.5 dex. For three DA white dwarfs with $T_{\rm eff}$ < 6000 K, the difference between spectroscopic and photometric log(g) values is greater than 0.5 dex. The photometric log(g) value for these stars is close to the canonical value of 8.0 in all cases, and the spectroscopic log(g) values are higher. We do not infer binarity in these systems and suggest instead that spectroscopic fitting of low $T_{\rm eff}$ DA white dwarfs may, in some cases, produce larger log(g) values than expected. We include some DA white dwarfs in our table that have low photometric log(g)

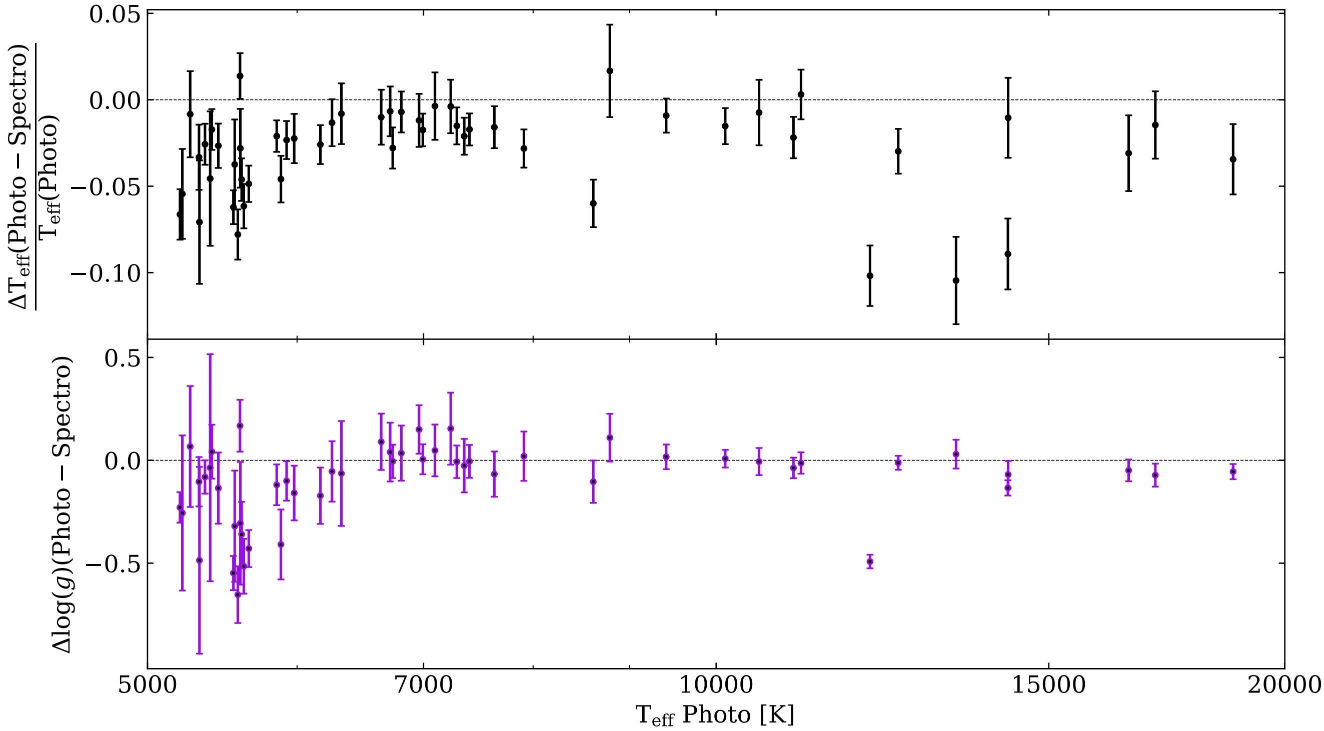

Figure 7. Differences between *Gaia* photometric (*Photo*) and spectroscopic (*Spectro*) $T_{\rm eff}$ (top) and log(g) (bottom) for DA white dwarfs observed with X-Shooter, against *Gaia* photometric $T_{\rm eff}$ (Gentile Fusillo et al. 2021). The spectroscopic fitting method is that which was used to fit all DA white dwarfs in this paper (see Section 3.2).

but larger spectroscopic log(g), as these are still candidate binary systems independent of their spectroscopic best-fit parameters.

WD J1604−7203 is a cool ($T_{\rm eff} \approx 4000$ K) DC white dwarf that has the lowest photometric log(g) in the entire 40 pc sample, of 6.75 ± 0.04 dex. Despite having a photometric $T_{\rm eff} < 4500$ K, we include it in our binary candidate list (Table 9) due to its remarkably low photometric log(g). Even allowing for binary evolution and mass loss resulting in a low-mass white dwarf component, current He-core white dwarf evolution models (Istrate et al. 2016) would not allow a low-mass white dwarf to cool down to such low surface temperature within the age of the universe. The best explanation for such a low photometric log(g) is that this is likely a multiple-degenerate system (double or triple), with its exact nature difficult to constrain given the known systematic photometric under-estimate of mass in very cool white dwarfs (Paper II), and the lack of spectral lines.

Gaia DR3 provides the renormalised unit weight error (RUWE) parameter, which should be around 1.0 for single stars (Belokurov et al. 2020). If the RUWE is significantly greater than 1.0, this indicates a poor astrometric solution, possibly due to contamination that might have also affected the photometry. **WD J1318+7353** and **WD J2126−4224** have RUWE values of 3.5 and 9.1 respectively, indicating that they may be binary systems or otherwise variable.

Table 10 lists all other white dwarfs we observe that are part of a binary system, and was built based on mixed spectral types and common proper-motion pairs. All common proper-motion companions with no confirmed spectral types lie on the main-sequence of the *Gaia* HR diagram. The companions of **WD J1406−6957** and **WD J1945−4904** are candidate cool M-dwarfs with indicative spectral type M7 (Reylé 2018). The small number of unresolved WD+MS binaries in 40 pc are missing from Gentile Fusillo et al. (2021).

Zuckerman (2014) investigated metal-polluted WD+MS star binary systems in order to elucidate the frequency of wide-orbit planets as a function of the semi-major axis of a binary. They found that over a certain range of semi-major axes, the presence of a secondary star suppressed the formation and/or long-term stability of an extended planetary system around the primary. Specifically, for binary star sky plane separations between about 120 and 2500 AU, white dwarfs are significantly less likely to be polluted with heavy elements than single white dwarfs or binaries with sky plane separations >2500 AU.

White dwarfs in Table 10 are consistent with this pattern. Eighteen Table 10 white dwarfs are not a DQ, or in a double degenerate, or have sky plane separations less than 120 AU. Of these 18, 13 have semi-major axes between 120 and 2500 AU; only one is metal polluted. For sky plane separations >2500 AU, one in five of the white dwarfs are polluted.

One can combine the results from the Zuckerman (2014) and the present paper. In an annulus between about 190 and 2800 AU (a ratio of semi-major axes ≈15), there are 28 non-polluted and no polluted white dwarfs, whereas, based on statistics from the 40 pc southern sub-sample presented in this work, 4 should be polluted.

Table 9. New unresolved double degenerate binary candidates in our 40 pc subsample (this work).

WD J name	SpT	*Gaia* $T_{\rm eff}$	*Gaia* log(*g*)
0551−2609	DC	4750 (40)	7.30 (0.03)
1117−4411	DC	5590 (30)	7.53 (0.02)
1318+7353	DC	5000 (40)	7.35 (0.04)
1447−6940	DC	4470 (30)	7.24 (0.02)
1503−2441	DA	5670 (30)	7.60 (0.02)
1601−3832	DA	4910 (40)	7.69 (0.03)
1604−7203	DC	4090 (40)	6.75 (0.04)
1815+5532	DC	4630 (50)	7.19 (0.04)
1821−5951	DA	4750 (30)	7.27 (0.03)
1833−6942	DA	8010 (60)	7.39 (0.02)
1919+4527	DC	4780 (20)	7.31 (0.02)
2126−4224	DC	5480 (30)	7.52 (0.03)

6 CONCLUSIONS

The volume-limited 20 pc sample has been, up until *Gaia* DR2, the largest volume-limited sample of white dwarfs (Hollands et al. 2018). In Paper I and Paper II, a sample of northern hemisphere white dwarfs within 40 pc was presented, with a high level of spectroscopic completeness. In this work, we have described the spectral types of 246 white dwarfs within $1\sigma_\varpi$ of 40 pc, of which 209 were previously unobserved and five have updated spectral types from higher quality spectroscopic observations. We have identified many new magnetic white dwarfs, some of which display complex Zeeman splitting, and have estimated their field strengths. We have observed metal-polluted white dwarfs, including **WD J2236−5548** and **WD J0808−5300** which are polluted by five and six metals, respectively. We have re-observed the warm DQ white dwarf **WD J2140−3637** and detected oxygen in its atmosphere for the first time. We report three new white dwarfs which are metal-polluted and display carbon absorption lines (DQZ and DZQ spectral types). We have also presented new candidate unresolved binary systems from their photometric over-luminosity.

We have fitted DA white dwarfs spectroscopically as well as photometrically. We noted that there is a similar offset in $T_{\rm eff}$ for spectroscopic parameters using both southern X-Shooter (this work) and northern WHT (Paper I) data sets, when compared to *Gaia* photometric fitting.

The volume-limited 40 pc sample of *Gaia* white dwarfs now has a very high level of spectroscopic completeness and we have used this sample to perform a statistical analysis of the local population of white dwarfs (Cukanovaite et al. 2022). We have confirmed the classification of 1058 white dwarfs out of 1083 candidates from DR3. The 40 pc sample provides an eight-fold increase in volume over the previous 20 pc sample (Hollands et al. 2018), which did not have the level of spectroscopic completeness that the 40 pc sample now has. The completeness of the *Gaia* DR3 white dwarf catalogue as well as the selection of Gentile Fusillo et al. (2021) are expected to be very high for single white dwarfs.

Creating significantly larger volume-limited samples than 40 pc requires MOS surveys such as WEAVE, 4MOST and DESI (De Jong et al. 2019; Dalton et al. 2020; Cooper et al. 2022), which may take decades to cover the whole sky. Therefore, the 40 pc sample will be the benchmark volume-limited white dwarf sample for many years to come. A full statistical analysis of the 40 pc sample is being prepared and will be presented in a future paper (Paper IV).

ACKNOWLEDGEMENTS

This work is based on observations collected at the European Southern Observatory under ESO programmes 0102.C-0351, 1103.D-0763, and 105.20ET.001. Based on observations made with the Gran Telescopio Canarias (GTC; programme GTC103-21A), installed in the Spanish Observatorio del Roque de los Muchachos of the Instituto de Astrofísica de Canarias, in the island of La Palma. Based on observations obtained at the Southern Astrophysical Research (SOAR) telescope, which is a joint project of the Ministério da Ciência, Tecnologia e Inovações (MCTI/LNA) do Brasil, the US National Science Foundation's NOIRLab, the University of North Carolina at Chapel Hill (UNC), and Michigan State University (MSU). This work has made use of data from the European Space Agency (ESA) mission *Gaia* (`https://www.cosmos.esa.int/gaia`), processed by the *Gaia* Data Processing and Analysis Consortium (DPAC, `https://www.cosmos.esa.int/web/gaia/dpac/consortium`). Funding for the DPAC has been provided by national institutions, in particular the institutions participating in the *Gaia* Multilateral Agreement. Research at Lick Observatory is partially supported by a generous gift from Google.

This project has received funding from the European Research Council (ERC) under the European Union's Horizon 2020 research and innovation programme (Grant agreement No. 101020057). PET, BTG, IP and TRM were supported by grant ST/T000406/1 from the Science and Technology Facilities Council (STFC). MAH was supported by grant ST/V000853/1 from the STFC. The authors acknowledge financial support from Imperial College London through an Imperial College Research Fellowship grant awarded to CJM. SGP acknowledges the support of a STFC Ernest Rutherford Fellowship. MRS thanks for support from ANID, – Millennium Science Initiative Program – NCN19_171 and FONDECYT (grant 1221059). RR has received funding from the postdoctoral fellowship program Beatriu de Pinós, funded by the Secretary of Universities and Research (Government of Catalonia) and by the Horizon 2020 programme of research and innovation of the European Union under the Maria Skłodowska-Curie grant agreement No 801370. ST and ARM acknowledge support from MINECO under the PID2020-117252GB-I00 grant. ARM acknowledges support from Grant RYC-2016-20254 funded by MCIN/AEI/10.13039/501100011033 and by ESF Investing in your future. DDM acknowledges support from the Italian Space Agency (ASI) and National Institute for Astrophysics (INAF) under agreements I/037/12/0 and 2017-14-H.0 and from INAF project funded with Presidential Decree N.43/2018. TC was supported by the Leverhulme Trust Grant (ID RPG-2020-366).

DATA AVAILABILITY STATEMENT

The raw X-Shooter data underlying this article are available in the ESO archive, at `http://archive.eso.org/cms.html`.

Any reduced spectra from any spectrograph used in this article will be shared on reasonable request to the corresponding author.

REFERENCES

Ahumada R., et al., 2020, ApJS, 249, 3
Apps K., Smart R. L., Silvotti R., 2021, Research Notes of the American Astronomical Society, 5, 229
Bagnulo S., Landstreet J. D., 2020, A&A, 643, A134
Bagnulo S., Landstreet J. D., 2021, MNRAS, 507, 5902
Bagnulo S., Landstreet J. D., 2022, ApJ, 935, L12
Barnett J. W., Williams K. A., Bédard A., Bolte M., 2021, AJ, 162, 162
Barrientos M., Chanamé J., 2021, ApJ, 923, 181
Barstow M. A., Jordan S., O'Donoghue D., Burleigh M. R., Napiwotzki R., Harrop-Allin M. K., 1995, MNRAS, 277, 971
Bédard A., Bergeron P., Fontaine G., 2017, ApJ, 848, 11
Bédard A., Bergeron P., Brassard P., Fontaine G., 2020, ApJ, 901, 93
Bédard A., Bergeron P., Brassard P., 2022, ApJ, 930, 8
Belokurov V., et al., 2020, MNRAS, 496, 1922
Bergeron P., Leggett S. K., Ruiz M. T., 2001, ApJS, 133, 413
Bergeron P., et al., 2011, ApJ, 737, 28
Bergeron P., Dufour P., Fontaine G., Coutu S., Blouin S., Genest-Beaulieu C., Bédard A., Rolland B., 2019, ApJ, 876, 67
Bergeron P., et al., 2021, AJ, 162, 188
Bergeron P., Kilic M., Blouin S., Bédard A., Leggett S. K., Brown W. R., 2022, ApJ, 934, 36
Bidelman W. P., 1985, ApJS, 59, 197
Blouin S., 2022, A&A, 666, L7
Blouin S., Dufour P., Allard N. F., Salim S., Rich R. M., Koopmans L. V. E., 2019a, ApJ, 872, 188
Blouin S., Dufour P., Thibeault C., Allard N. F., 2019b, ApJ, 878, 63
Cepa J., et al., 2000, in Iye M., Moorwood A. F., eds, Society of Photo-Optical Instrumentation Engineers (SPIE) Conference Series Vol. 4008, Optical and IR Telescope Instrumentation and Detectors. pp 623–631, doi:10.1117/12.395520
Cepa J., et al., 2003, in Iye M., Moorwood A. F. M., eds, Society of Photo-Optical Instrumentation Engineers (SPIE) Conference Series Vol. 4841, Instrument Design and Performance for Optical/Infrared Ground-based Telescopes. pp 1739–1749, doi:10.1117/12.460913
Chambers K. C., et al., 2016, arXiv e-prints, p. arXiv:1612.05560
Cheng S., Cummings J. D., Ménard B., 2019, ApJ, 886, 100
Chiappini C., et al., 2019, The Messenger, 175, 30
Clemens J. C., Crain J. A., Anderson R., 2004, in Moorwood A. F. M., Iye M., eds, Society of Photo-Optical Instrumentation Engineers (SPIE) Conference Series Vol. 5492, Ground-based Instrumentation for Astronomy. pp 331–340, doi:10.1117/12.550069
Cooper A. P., et al., 2022, arXiv e-prints, p. arXiv:2208.08514
Coutu S., Dufour P., Bergeron P., Blouin S., Loranger E., Allard N. F., Dunlap B. H., 2019, ApJ, 885, 74
Cukanovaite E., Tremblay P.-E., Bergeron P., Freytag B., Ludwig H.-G., Steffen M., 2021, MNRAS, 501, 5274
Cukanovaite E., Tremblay P. E., Toonen S., Temmink K. D., Manser C. J., O'Brien M. W., McCleery J., 2022, arXiv e-prints, p. arXiv:2209.13919
Cummings J. D., Kalirai J. S., Tremblay P. E., Ramirez-Ruiz E., Choi J., 2018, ApJ, 866, 21
Cunningham T., Wheatley P. J., Tremblay P.-E., Gänsicke B. T., King G. W., Toloza O., Veras D., 2022, Nature, 602, 219
Dalton G., et al., 2020, in Society of Photo-Optical Instrumentation Engineers (SPIE) Conference Series. p. 1144714, doi:10.1117/12.2561067
Dufour P., Bergeron P., Fontaine G., 2005, ApJ, 627, 404
Dufour P., Liebert J., Fontaine G., Behara N., 2007, Nature, 450, 522
Dunlap B. H., Clemens J. C., 2015, in Dufour P., Bergeron P., Fontaine G., eds, Astronomical Society of the Pacific Conference Series Vol. 493, 19th European Workshop on White Dwarfs. p. 547
Dupuis J., Vennes S., Bowyer S., Pradhan A. K., Thejll P., 1994, in American Astronomical Society Meeting Abstracts #184. p. 29.01
El-Badry K., Rix H.-W., Weisz D. R., 2018, ApJ, 860, L17
Elms A. K., Tremblay P.-E., Gänsicke B. T., Koester D., Hollands M. A., Gentile Fusillo N. P., Cunningham T., Apps K., 2022, MNRAS, 517, 4557
Fabricant D., Cheimets P., Caldwell N., Geary J., 1998, PASP, 110, 79
Fantin N. J., et al., 2019, ApJ, 887, 148
Farihi J., 2016, New Astron. Rev., 71, 9
Farihi J., Dufour P., Wilson T. G., 2022, arXiv e-prints, p. arXiv:2208.05990
Ferrario L., Vennes S., Wickramasinghe D. T., Bailey J. A., Christian D. J., 1997, MNRAS, 292, 205
Ferrario L., Wickramasinghe D., Kawka A., 2020, Advances in Space Research, 66, 1025
Fontaine G., Brassard P., Bergeron P., 2001, PASP, 113, 409
Freudling W., Romaniello M., Bramich D. M., Ballester P., Forchi V., García-Dabló C. E., Moehler S., Neeser M. J., 2013, A&A, 559, A96
Friedrich S., Oestreicher R., Schweizer W., 1996, A&A, 309, 227
Gaia Collaboration et al., 2021, A&A, 649, A1
Gaidos E., et al., 2014, MNRAS, 443, 2561
Genest-Beaulieu C., Bergeron P., 2019, ApJ, 871, 169
Gentile Fusillo N. P., et al., 2019, MNRAS, 482, 4570
Gentile Fusillo N. P., Tremblay P.-E., Bohlin R. C., Deustua S. E., Kalirai J. S., 2020, MNRAS, 491, 3613
Gentile Fusillo N. P., et al., 2021, MNRAS, 508, 3877
Giammichele N., Bergeron P., Dufour P., 2012, ApJS, 199, 29
Gianninas A., Bergeron P., Ruiz M. T., 2011, ApJ, 743, 138
Gray R. O., Corbally C. J., Garrison R. F., McFadden M. T., Bubar E. J., McGahee C. E., O'Donoghue A. A., Knox E. R., 2006, AJ, 132, 161
Hall P. B., Maxwell A. J., 2008, ApJ, 678, 1292
Holberg J. B., Oswalt T. D., Sion E. M., 2002, ApJ, 571, 512
Holberg J. B., Oswalt T. D., Sion E. M., McCook G. P., 2016, MNRAS, 462, 2295
Hollands M. A., Koester D., Alekseev V., Herbert E. L., Gänsicke B. T., 2017, MNRAS, 467, 4970
Hollands M. A., Tremblay P. E., Gänsicke B. T., Gentile-Fusillo N. P., Toonen S., 2018, MNRAS, 480, 3942
Hollands M. A., et al., 2020, Nature Astronomy, 4, 663
Hollands M. A., Tremblay P.-E., Gänsicke B. T., Koester D., Gentile-Fusillo N. P., 2021, Nature Astronomy, 5, 451
Hollands M. A., Tremblay P. E., Gänsicke B. T., Koester D., 2022, MNRAS, 511, 71
Houk N., 1978, Michigan catalogue of two-dimensional spectral types for the HD stars. Dept. of Astronomy, University of Michigan
Hurley J. R., Pols O. R., Tout C. A., 2000, MNRAS, 315, 543
Istrate A. G., Marchant P., Tauris T. M., Langer N., Stancliffe R. J., Grassitelli L., 2016, A&A, 595, A35
de Jong R. S., et al., 2019, The Messenger, 175, 3
Kaiser B. C., Clemens J. C., Blouin S., Dufour P., Hegedus R. J., Reding J. S., Bédard A., 2021, Science, 371, 168
Kausch W., et al., 2015, A&A, 576, A78
Kawka A., Vennes S., 2011, A&A, 532, A7
Kawka A., Vennes S., 2012, MNRAS, 425, 1394
Kepler S. O., da Costa A. F. M., Giovannini O., Koester D., 2000, Baltic Astronomy, 9, 125

Kilic M., Bédard A., Bergeron P., Kosakowski A., 2020, MNRAS, 493, 2805
Kirkpatrick J. D., et al., 2016, ApJS, 224, 36
Kleinman S. J., et al., 2013, ApJS, 204, 5
Koester D., 2010, Mem. Soc. Astron. Italiana, 81, 921
Koester D., Kepler S. O., 2015, A&A, 583, A86
Koester D., Kepler S. O., 2019, A&A, 628, A102
Koester D., Schulz H., Weidemann V., 1979, A&A, 76, 262
Koester D., Kepler S. O., Irwin A. W., 2020, A&A, 635, A103
Külebi B., Jordan S., Euchner F., Gänsicke B. T., Hirsch H., 2009, A&A, 506, 1341
Külebi B., Jordan S., Nelan E., Bastian U., Altmann M., 2010, A&A, 524, A36
Landstreet J. D., Bagnulo S., 2019, A&A, 628, A1
Liebert J., Bergeron P., Holberg J. B., 2005, ApJS, 156, 47
Limoges M. M., Bergeron P., Lépine S., 2015, ApJS, 219, 19
van Maanen A., 1917, PASP, 29, 258
Martin D. C., et al., 2005, ApJ, 619, L1
McCleery J., et al., 2020, MNRAS, 499, 1890
O'Donoghue D., Kilkenny D., Koen C., Hambly N., MacGillivray H., Stobie R. S., 2013, MNRAS, 431, 240
Provencal J. L., Shipman H. L., Koester D., Wesemael F., Bergeron P., 2002, ApJ, 568, 324
Raddi R., et al., 2017, MNRAS, 472, 4173
Reid I. N., Gizis J. E., 2005, PASP, 117, 676
Reylé C., 2018, A&A, 619, L8
Rolland B., Bergeron P., Fontaine G., 2018, ApJ, 857, 56
Schmidt B. P., Keller S. C., Francis P. J., Bessell M. S., 2005, in American Astronomical Society Meeting Abstracts #206. p. 15.09
Scholz R. D., Irwin M., Ibata R., Jahreiß H., Malkov O. Y., 2000, A&A, 353, 958
Schreiber M. R., Belloni D., Gänsicke B. T., Parsons S. G., Zorotovic M., 2021a, Nature Astronomy, 5, 648
Schreiber M. R., Belloni D., Gänsicke B. T., Parsons S. G., 2021b, MNRAS, 506, L29
Sion E. M., Greenstein J. L., Landstreet J. D., Liebert J., Shipman H. L., Wegner G. A., 1983, ApJ, 269, 253
Skrutskie M. F., et al., 2006, AJ, 131, 1163
Smethells W. G., 1974, PhD thesis, Case Western Reserve University, Ohio
Smette A., et al., 2015, A&A, 576, A77
Subasavage J. P., Henry T. J., Bergeron P., Dufour P., Hambly N. C., Beaulieu T. D., 2007, AJ, 134, 252
Subasavage J. P., Henry T. J., Bergeron P., Dufour P., Hambly N. C., 2008, AJ, 136, 899
Subasavage J. P., et al., 2017, AJ, 154, 32
Toonen S., Hollands M., Gänsicke B. T., Boekholt T., 2017, A&A, 602, A16
Tremblay P. E., Ludwig H. G., Steffen M., Bergeron P., Freytag B., 2011a, A&A, 531, L19
Tremblay P. E., Bergeron P., Gianninas A., 2011b, ApJ, 730, 128
Tremblay P.-E., Ludwig H.-G., Steffen M., Freytag B., 2013, A&A, 559, A104
Tremblay P. E., Leggett S. K., Lodieu N., Freytag B., Bergeron P., Kalirai J. S., Ludwig H. G., 2014, ApJ, 788, 103
Tremblay P. E., Cukanovaite E., Gentile Fusillo N. P., Cunningham T., Hollands M. A., 2019, MNRAS, 482, 5222
Tremblay P. E., et al., 2020, MNRAS, 497, 130
Veras D., 2021, Oxford Research Encyclopedia of Planetary Science
Vernet J., et al., 2011, A&A, 536, A105
Williams K. A., Montgomery M. H., Winget D. E., Falcon R. E., Bierwagen M., 2016, ApJ, 817, 27
Wright E. L., et al., 2010, AJ, 140, 1868
Zuckerman B., 2014, ApJ, 791, L27
Zuckerman B., Koester D., Reid I. N., Hünsch M., 2003, ApJ, 596, 477
Zuckerman B., Koester D., Melis C., Hansen B. M., Jura M., 2007, ApJ, 671, 872

Table 10. Binary systems in our 40 pc subsample (this work).

Gaia DR3 ID	WD J name (where applicable)	SpT	Sep (arcsec)
2377344185944929152 2377344185944929280	0044–1148	DZ	4.3
2486388560866377856 2486388560866377728	0212–0804	DA dM (a)	3.7
4672306015773211008	0312–6444	DA+DA (b)	–
4613612951211823616 4613612951211823104	0317–8532A 0317–8532B	DA (c) DAH (d)	6.9
4678664766393827328 4678664766393829504	0416–5917	DA (e) dK (f)	13.1
2925551818747071488 2925551853106808832	0646–2246	DC	5.2
5624029566946316928 5624029566946047616	0907–3609	DA	10.8
5436014972680358272 5436014972680358784	0936–3721 0936–3721	DA (g) DQ (h)	4.2
6133033635916500608 6133033601555979648	1234–4440	DC G (f)	38.1
6188345358621778816 6188345358621678592	1327–2817	DQ dK (i)	5.2
5845312191917620224 5845300239052540416	1333–6751	DZ	283
5846206030463663232 5846206202262355712	1406–6957	DA	25.2
6272326022391660928 6272325816233230848	1430–2403	DA	36.6
6271903947364173056 6271903943069412608	1430–2520	DA	8.5
4053455379420643584 4053455379465036800	1738–3427	DA	3.5
5909739660590724224 5909762269301963264	1746–6251	DA G (f)	430
6725656144031366144 6725655937872937472	1809–4101	DC	214
4073522222505044224 4073522012035886848	1857–2650	DA	70.2
6671045050707117568 6671044947630014464	1945–4904	DC	49.5
6665685378201412992 6665685343840128384	1956–5258	DA dM (j)	4.7
6470278694244646912 6470278694244647168	2049–5446	DA dK (k)	23.3
6578917727331681536 6578729710843028608	2126–4224	DC dM (j)	208
6485572518732377856 6485572557387287680	2343–6447	DC dK (f)	41.4

Note: References here are different to Table 3. (a) Gaidos et al. (2014), (b) Külebi et al. (2010), (c) Kilic et al. (2020), (d) Barstow et al. (1995), (e) Bédard et al. (2017), (f) Gray et al. (2006), (g) Gianninas et al. (2011), (h) Dufour et al. (2005), (i) Bidelman (1985), (j) Smethells (1974), (k) Houk (1978). WD J031225.70–644410.89 is an unresolved single *Gaia* source.

Affiliations

[1] Department of Physics, University of Warwick, Coventry, CV4 7AL, UK

[2] European Southern Observatory, Karl Schwarzschild Straße 2, Garching, 85748, Germany

[3] Department of Physics and Astronomy, University of Sheffield, Sheffield, S3 7RH, UK

[4] Institut für Theoretische Physik und Astrophysik, University of Kiel, 24098 Kiel, Germany

[5] Department of Earth, Planetary, and Space Sciences, University of California, Los Angeles, CA 90095, USA

[6] Department of Physics and Astronomy, University College London, London WC1E 6BT, UK

[7] Department of Astronomy & Institute for Astrophysical Research, Boston University, 725 Commonwealth Ave., Boston, MA 02215, USA

[8] Lunar and Planetary Laboratory, Sonett Space Science Building, University of Arizona, Tucson, Arizona 85721, USA

[9] Astronomisches Rechen-Institut, Zentrum für Astronomie der Universität Heidelberg, D-69120 Heidelberg, Germany

[10] Department of Physics and Astronomy, University of California, Los Angeles, CA 90095-1562, USA

[11] Astromanager LLC, Hilo, HI 96720, USA

[12] Astrophysics Group, Department of Physics, Imperial College London, Prince Consort Rd, London, SW7 2AZ, UK

[13] INAF - Capodimonte Astronomical Observatory Naples Via Moiariello 16, I-80131 Naples, Italy

[14] Center for Astrophysics and Space Sciences, University of California, San Diego, CA 92093-0424, USA

[15] Gemini Observatory, Hilo, HI 96720, USA

[16] Departament de Física, Universitat Politècnica de Catalunya, c/Esteve Terrades 5, 08860 Castelldefels, Spain

[17] Institut d'Estudis Espacials de Catalunya, Ed. Nexus-201, c/Gran Capità 2-4, 08034 Barcelona, Spain

[18] Departamento de Física, Universidad Técnica Federico Santa María, Avenida España 1680, Valparaíso, Chile

[19] Millennium Nucleus for Planet Formation, NPF, Valparaíso, Chile

[20] INAF-Osservatorio Astrofisico di Torino, Strada dell'Osservatorio 20, 10025, Pino Torinese, Italy

[21] Institute for Gravitational Wave Astronomy, School of Physics and Astronomy, University of Birmingham, Birmingham, B15 2TT, UK

[22] Earth and Planets Laboratory, Carnegie Institution for Science, 5241 Broad Branch Rd NW, Washington, DC 20015, USA

APPENDIX A: ONLINE FIGURES

This paper has been typeset from a TEX/LATEX file prepared by the author.

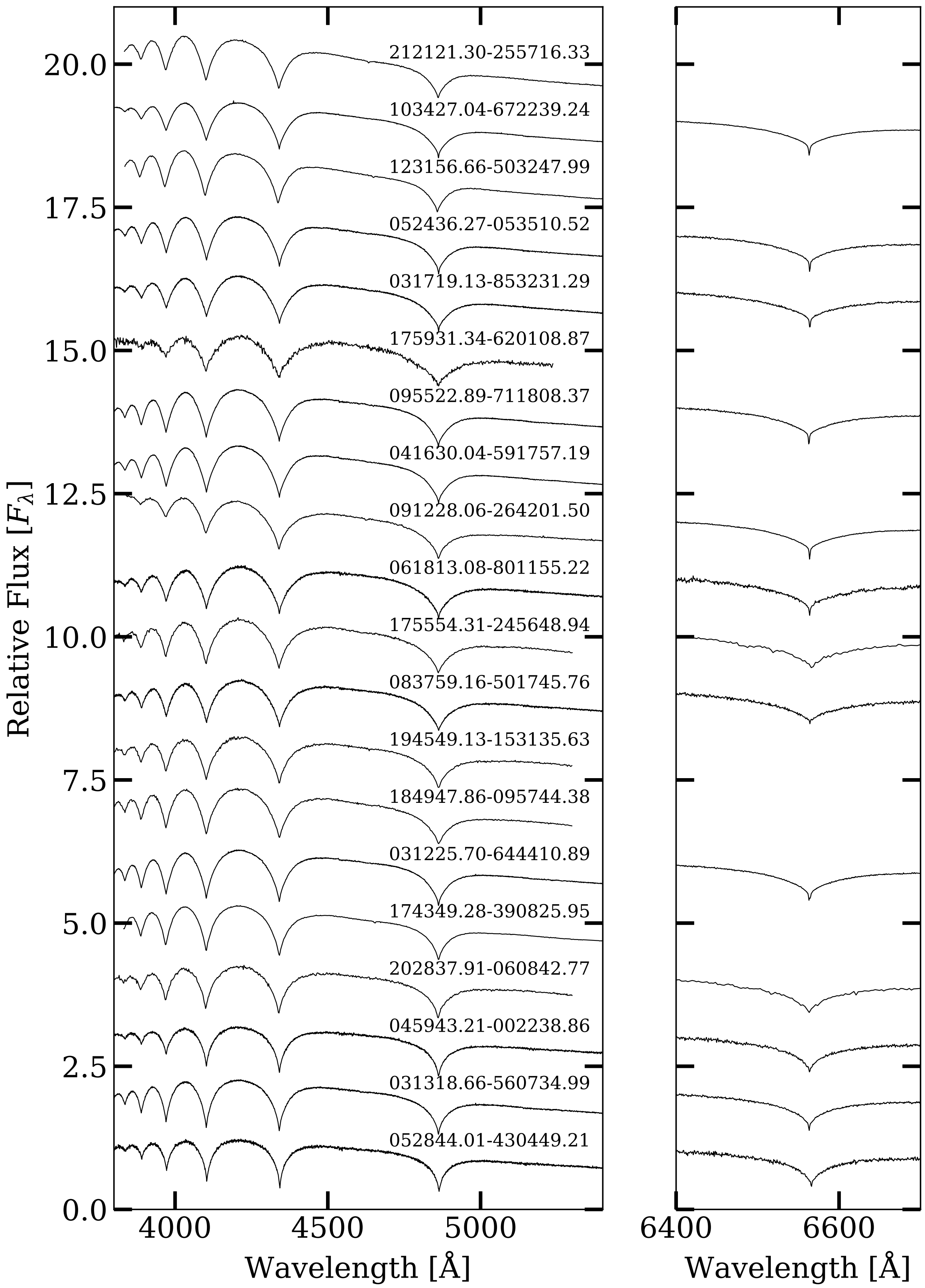

Figure A1. Spectroscopic observations of 100 DA white dwarfs ordered with decreasing photometric temperature (1/5). Temperature range: 19 500 K > $T_{\rm eff}$ > 10 500 K.

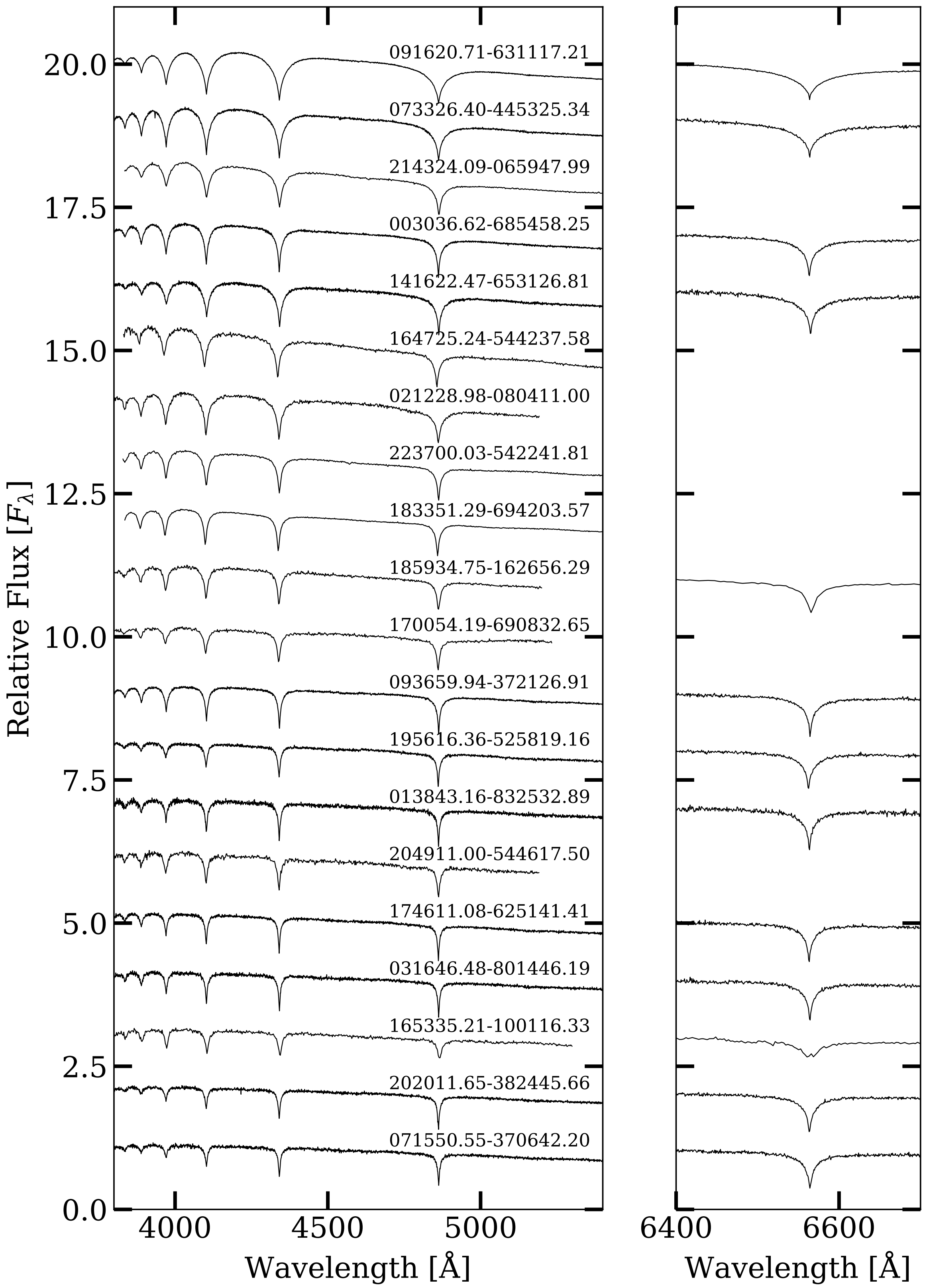

Figure A1. Spectroscopic observations of 100 DA white dwarfs ordered with decreasing photometric temperature (2/5). Temperature range: 10 500 K > $T_{\rm eff}$ > 7200 K.

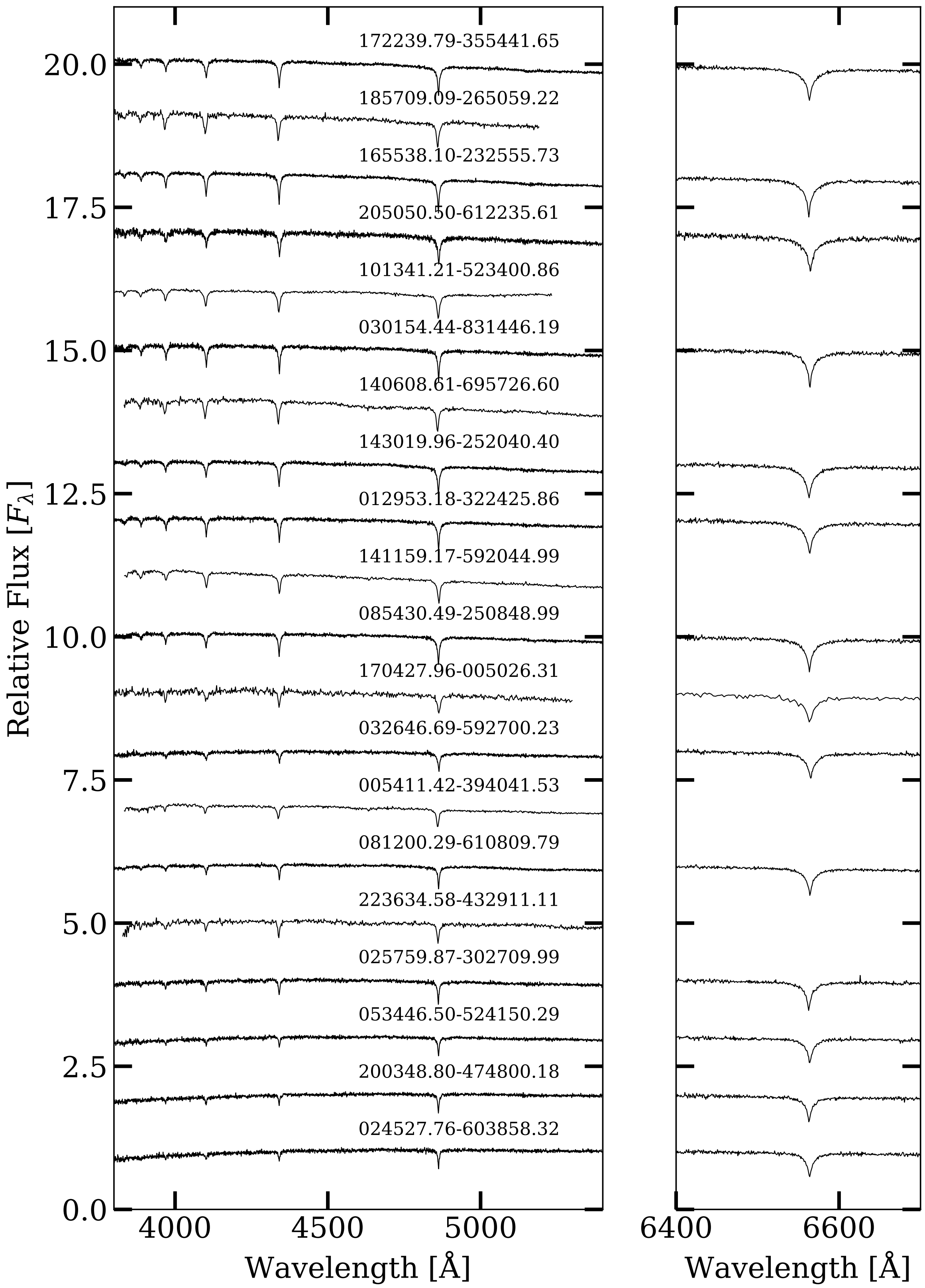

Figure A1. Spectroscopic observations of 100 DA white dwarfs ordered with decreasing photometric temperature (3/5). Temperature range: 7200 K > $T_{\rm eff}$ > 5900 K.

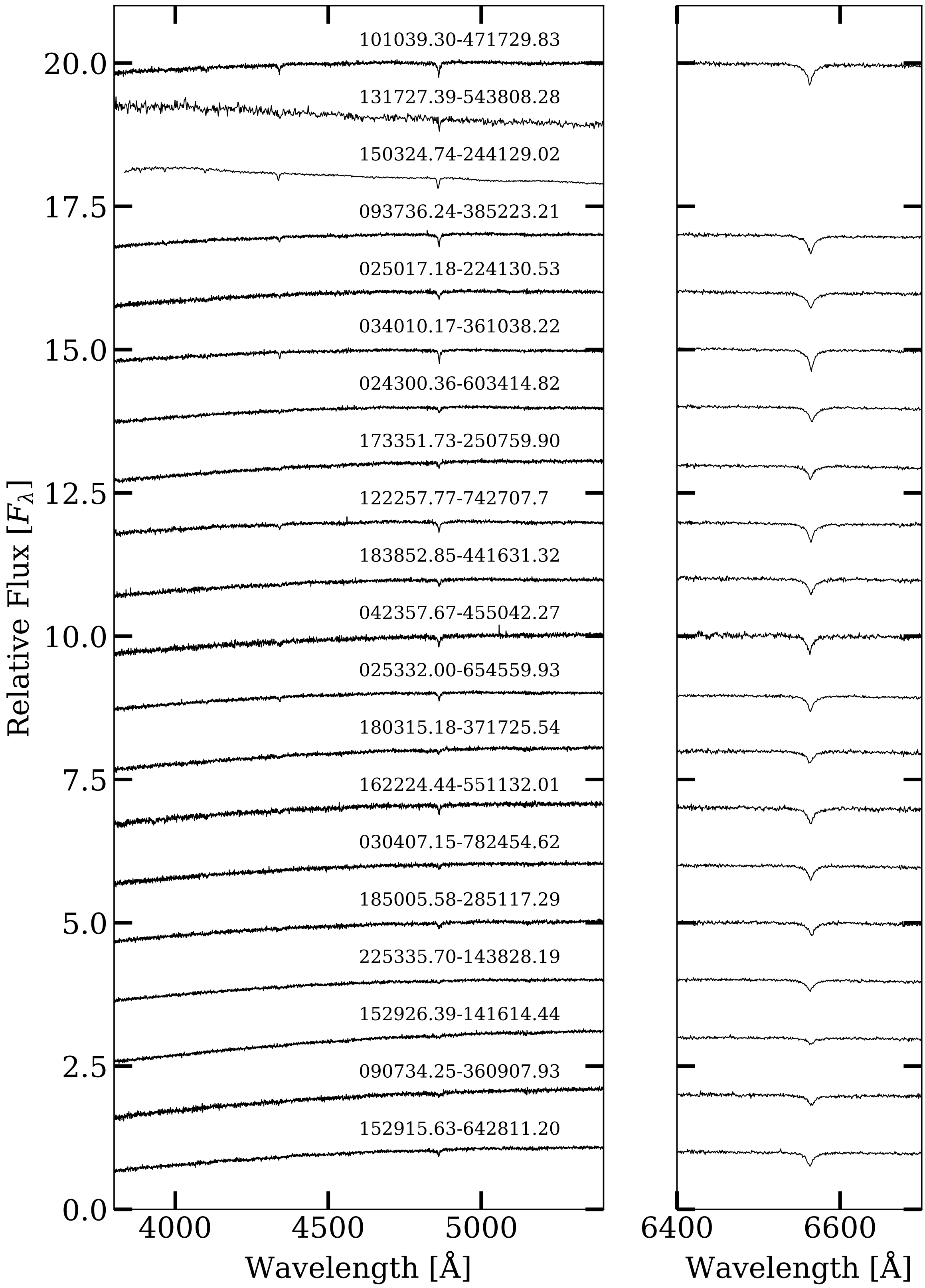

Figure A1. Spectroscopic observations of 100 DA white dwarfs ordered with decreasing photometric temperature (4/5). Temperature range: 5900 K > $T_{\rm eff}$ > 5200 K.

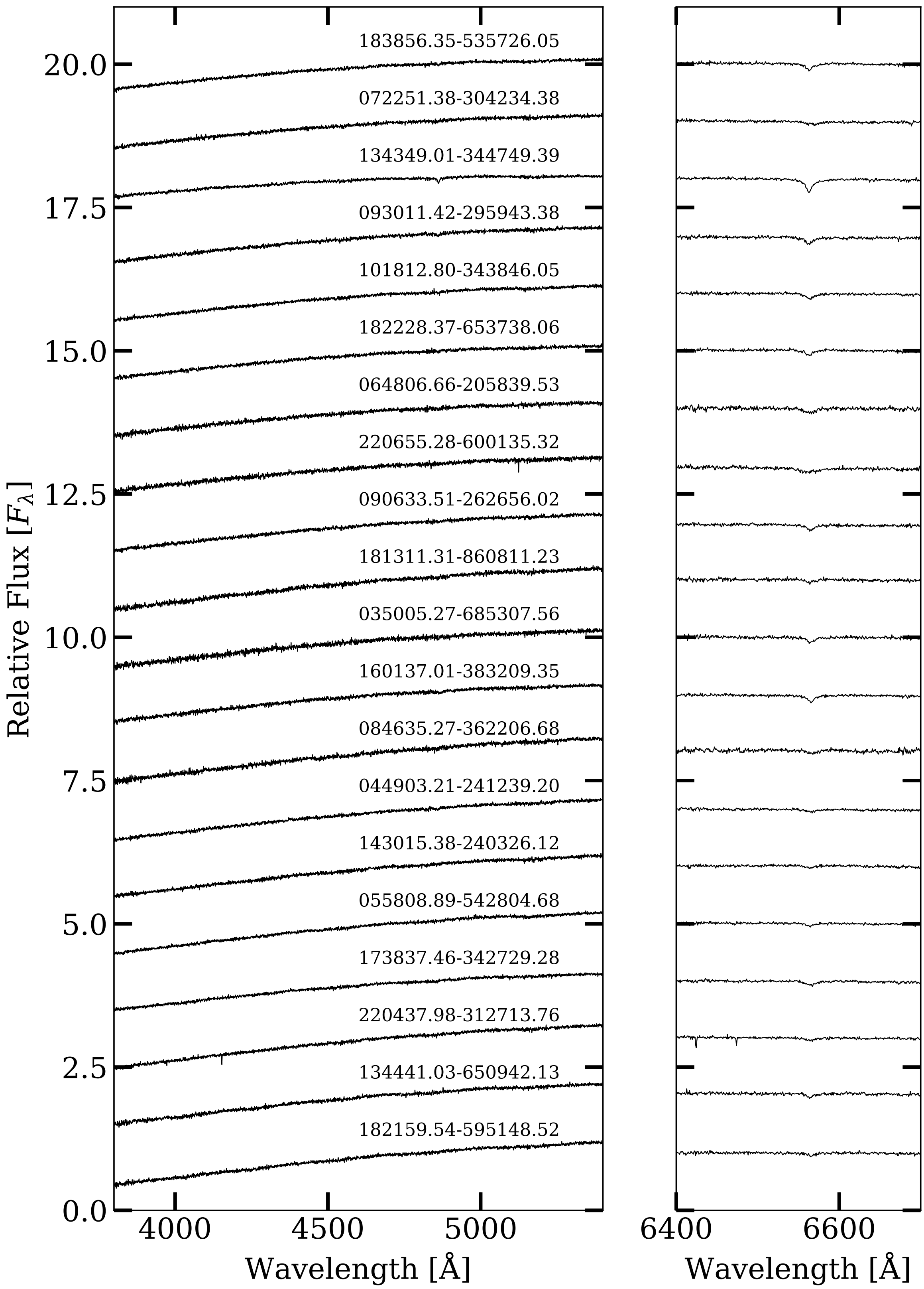

Figure A1. Spectroscopic observations of 100 DA white dwarfs ordered with decreasing photometric temperature (5/5). Temperature range: 5200 K > $T_{\rm eff}$ > 4800 K.

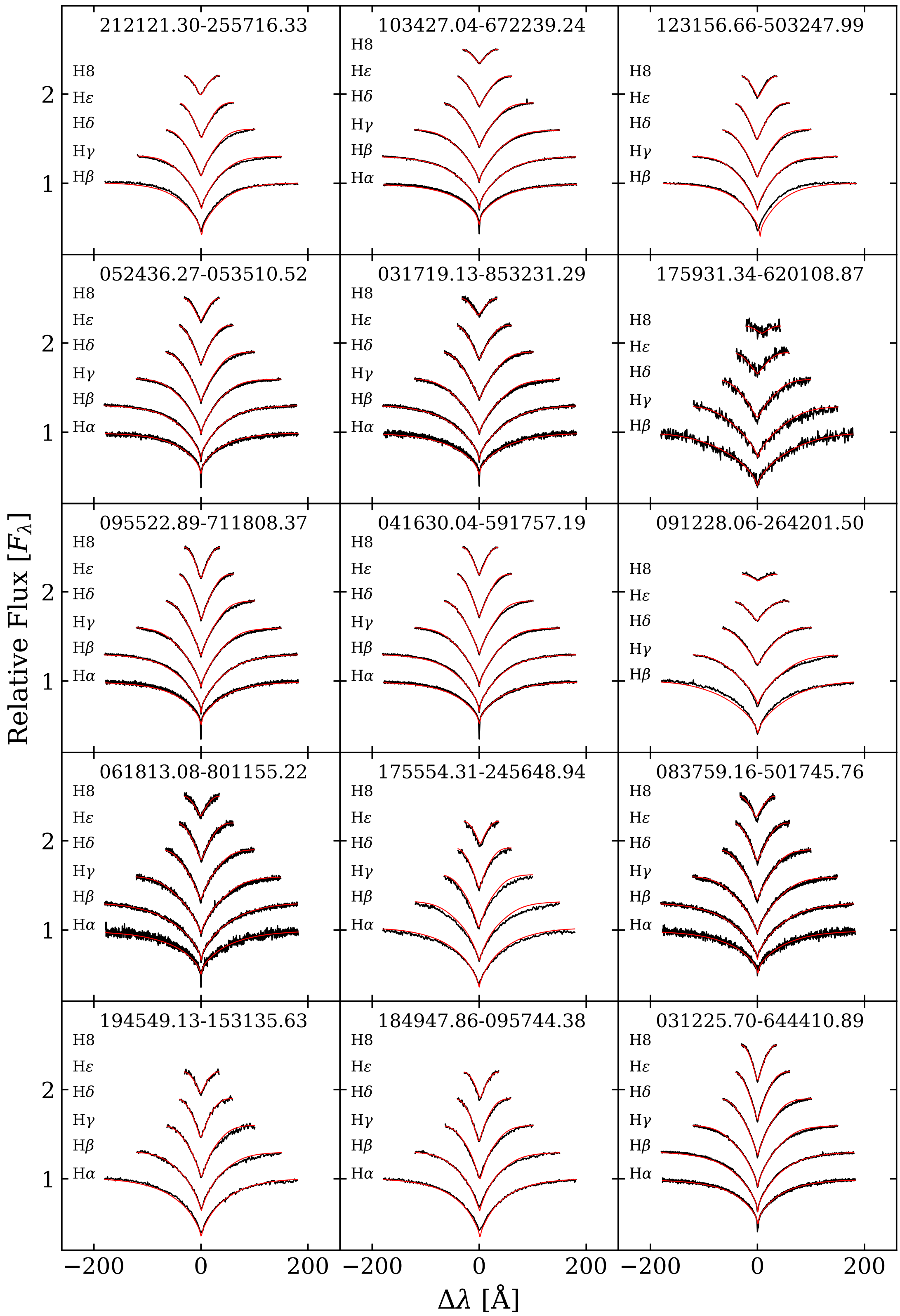

Figure A2. Spectroscopic fits to the normalised Balmer lines for 81 DA white dwarfs ordered with decreasing photometric temperature (1/6). Temperature range: 19 500 K > $T_{\rm eff}$ > 12 000 K.

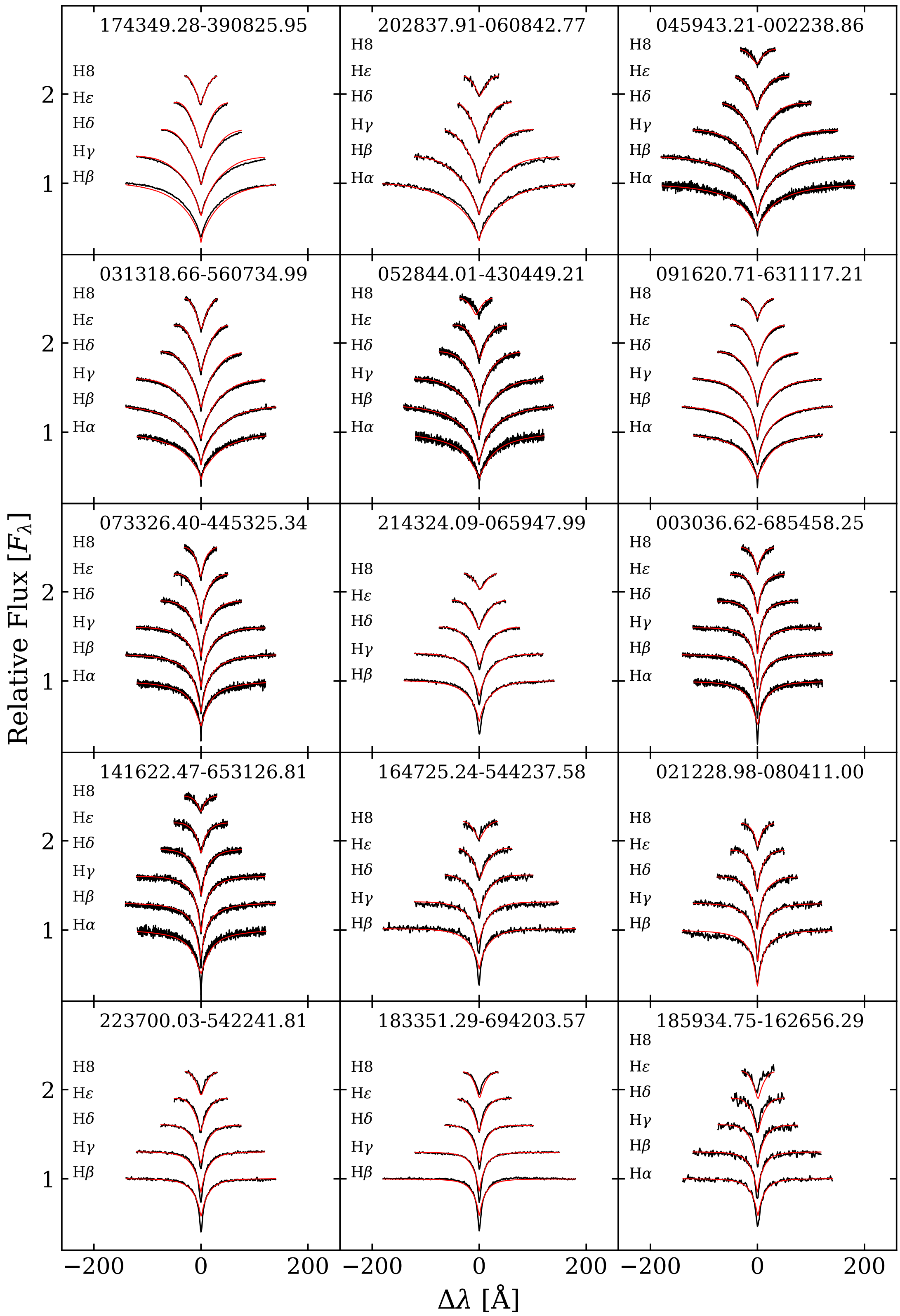

Figure A2. Spectroscopic fits to the normalised Balmer lines for 81 DA white dwarfs ordered with decreasing photometric temperature (2/6). Temperature range: 12 000 K > $T_{\rm eff}$ > 8000 K.

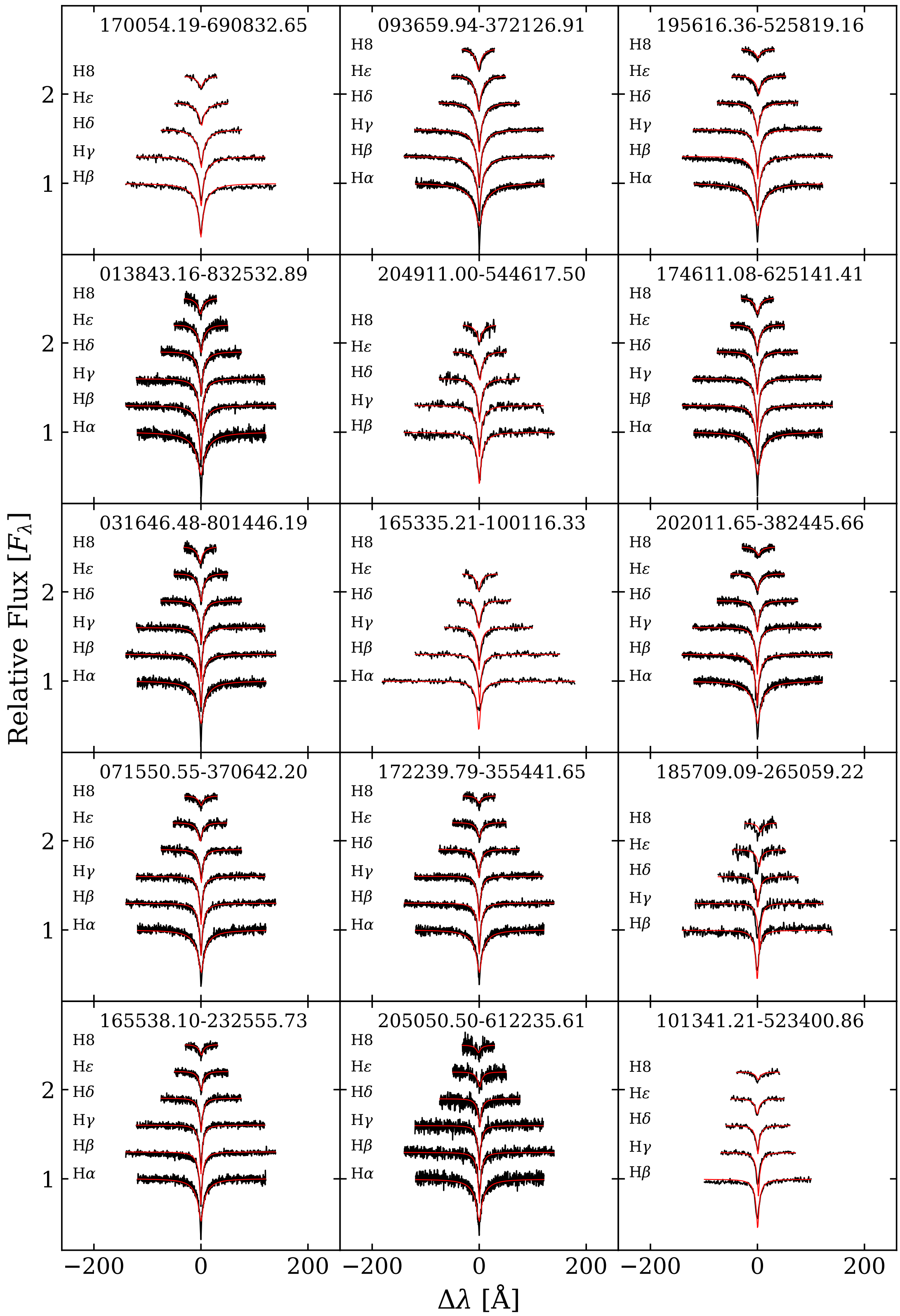

Figure A2. Spectroscopic fits to the normalised Balmer lines for 81 DA white dwarfs ordered with decreasing photometric temperature (3/6). Temperature range: 8000 K > $T_{\rm eff}$ > 6900 K.

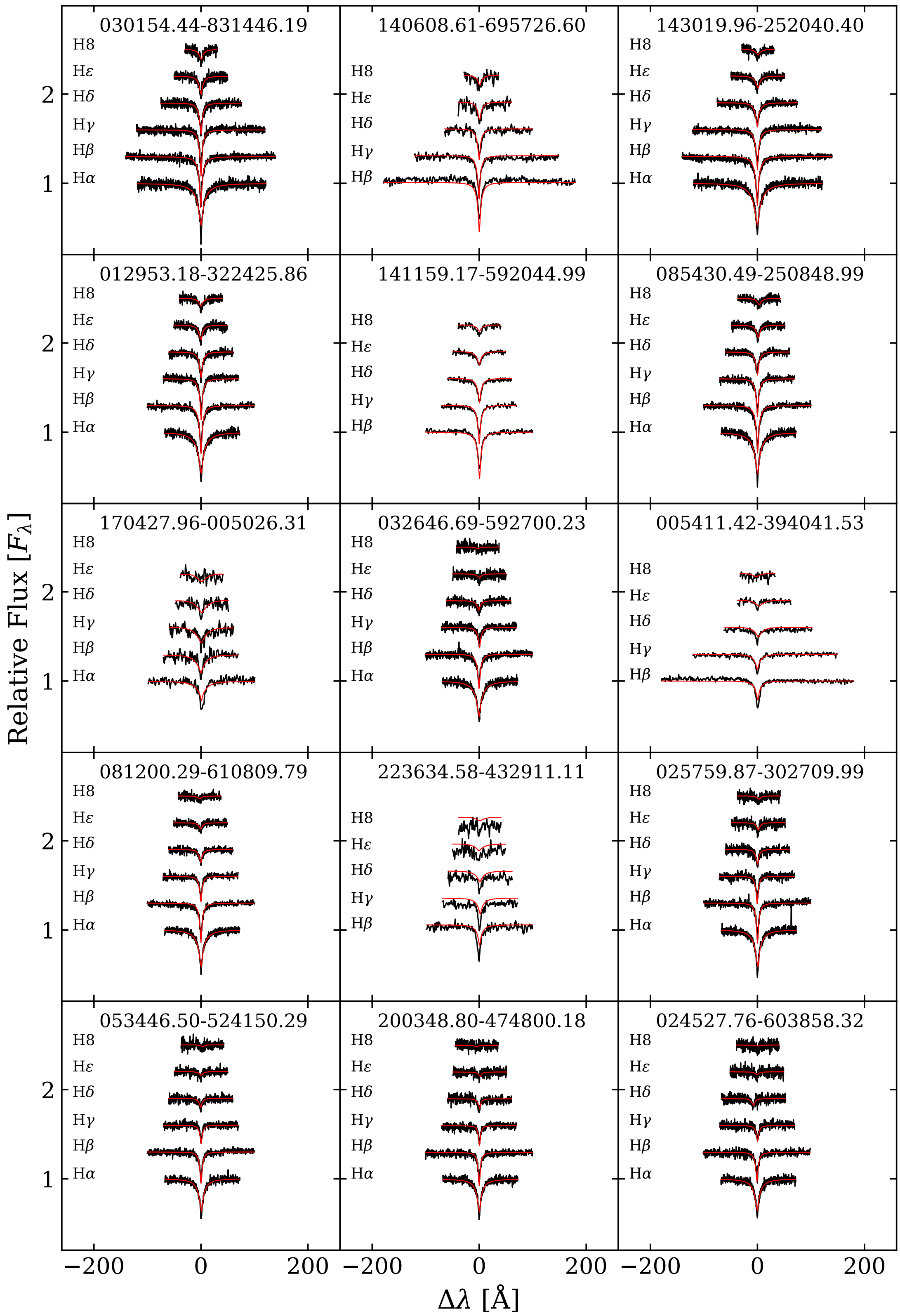

Figure A2. Spectroscopic fits to the normalised Balmer lines for 81 DA white dwarfs ordered with decreasing photometric temperature (4/6). Temperature range: 6900 K > $T_{\rm eff}$ > 5900 K.

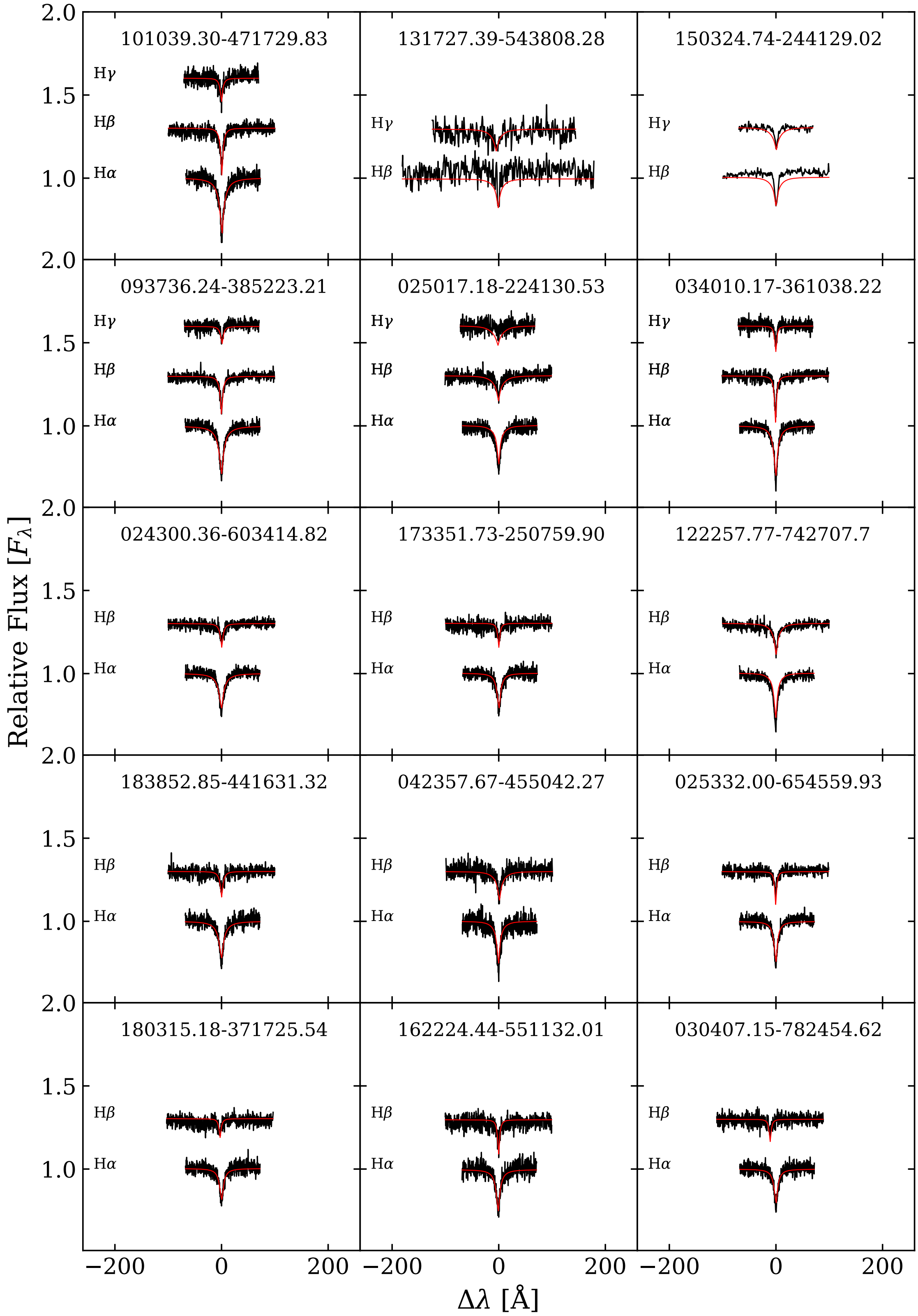

Figure A2. Spectroscopic fits to the normalised Balmer lines for 81 DA white dwarfs ordered with decreasing photometric temperature (5/6). Temperature range: 5900 K > $T_{\rm eff}$ > 5400 K.

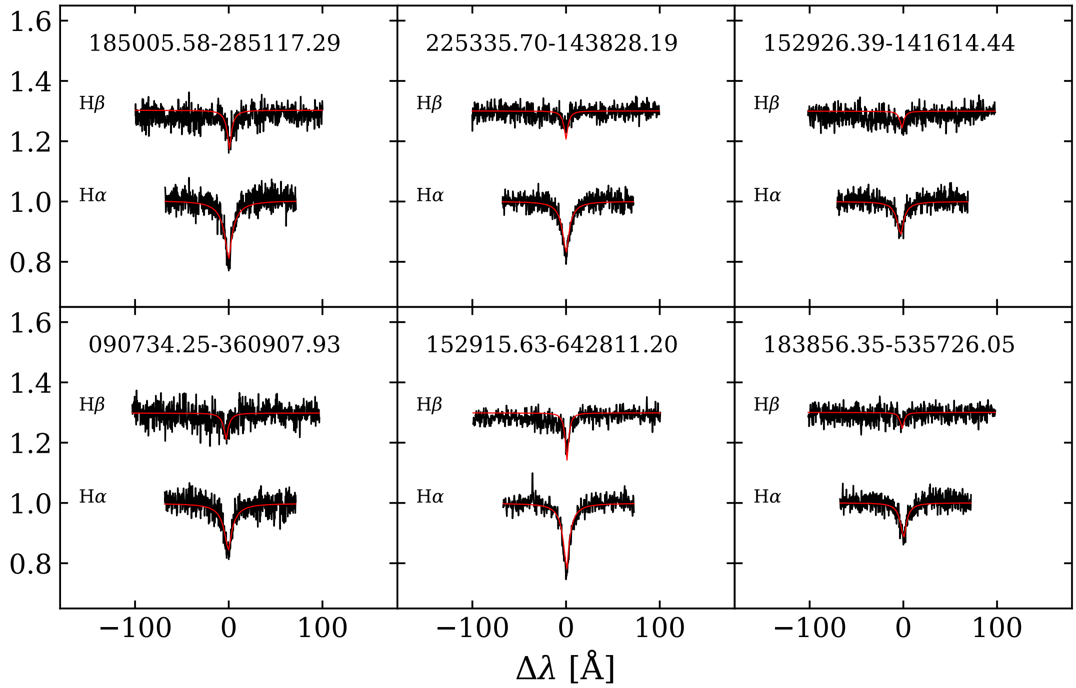

Figure A2. Spectroscopic fits to the normalised Balmer lines for 81 DA white dwarfs ordered with decreasing photometric temperature (6/6). Temperature range: 5400 K > $T_{\rm eff}$ > 5200 K.

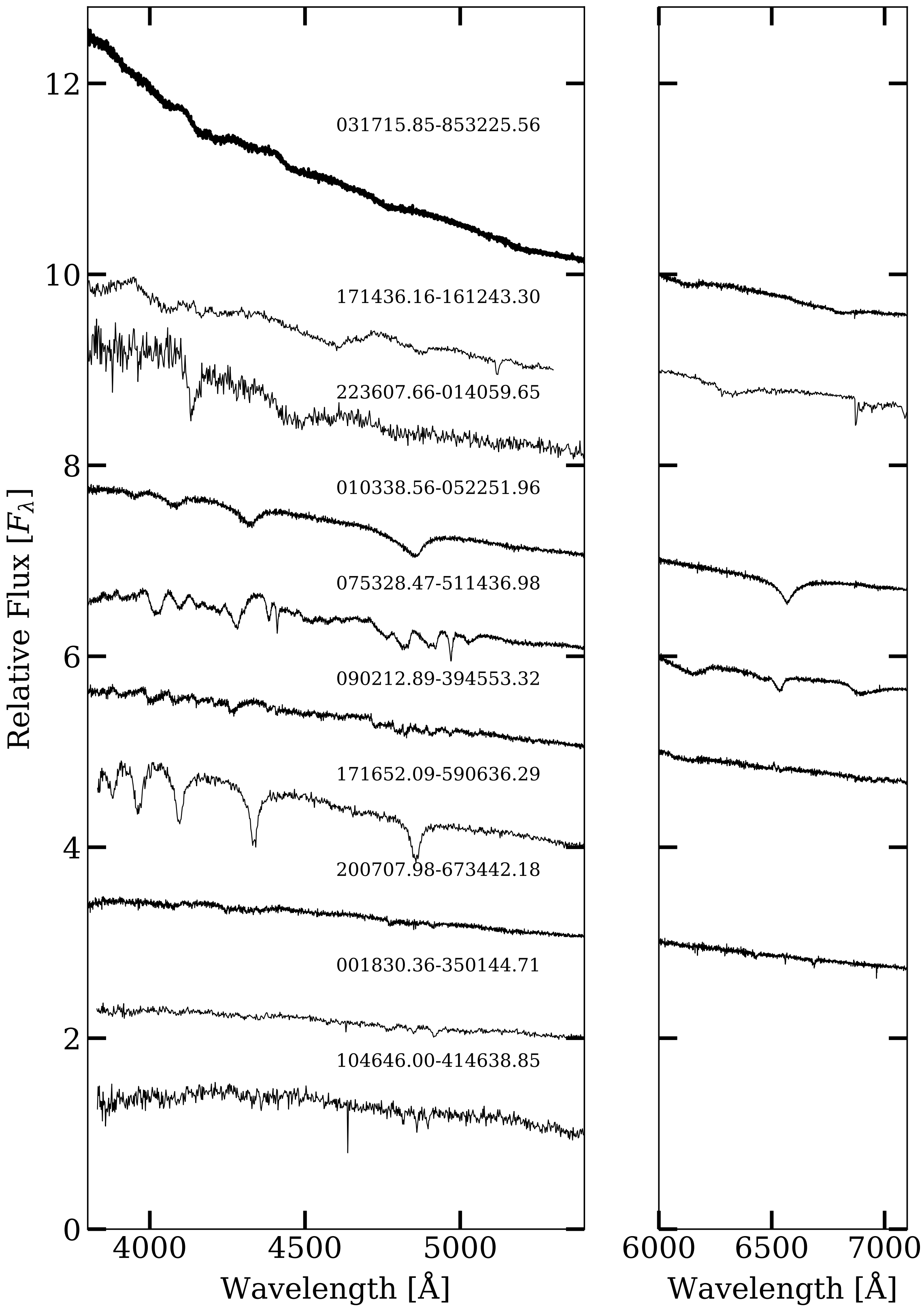

Figure A3. Spectroscopic observations of 28 DAH magnetic white dwarfs ordered with decreasing photometric temperature (1/3). Temperature range: 26 500 K > $T_{\rm eff}$ > 6700 K.

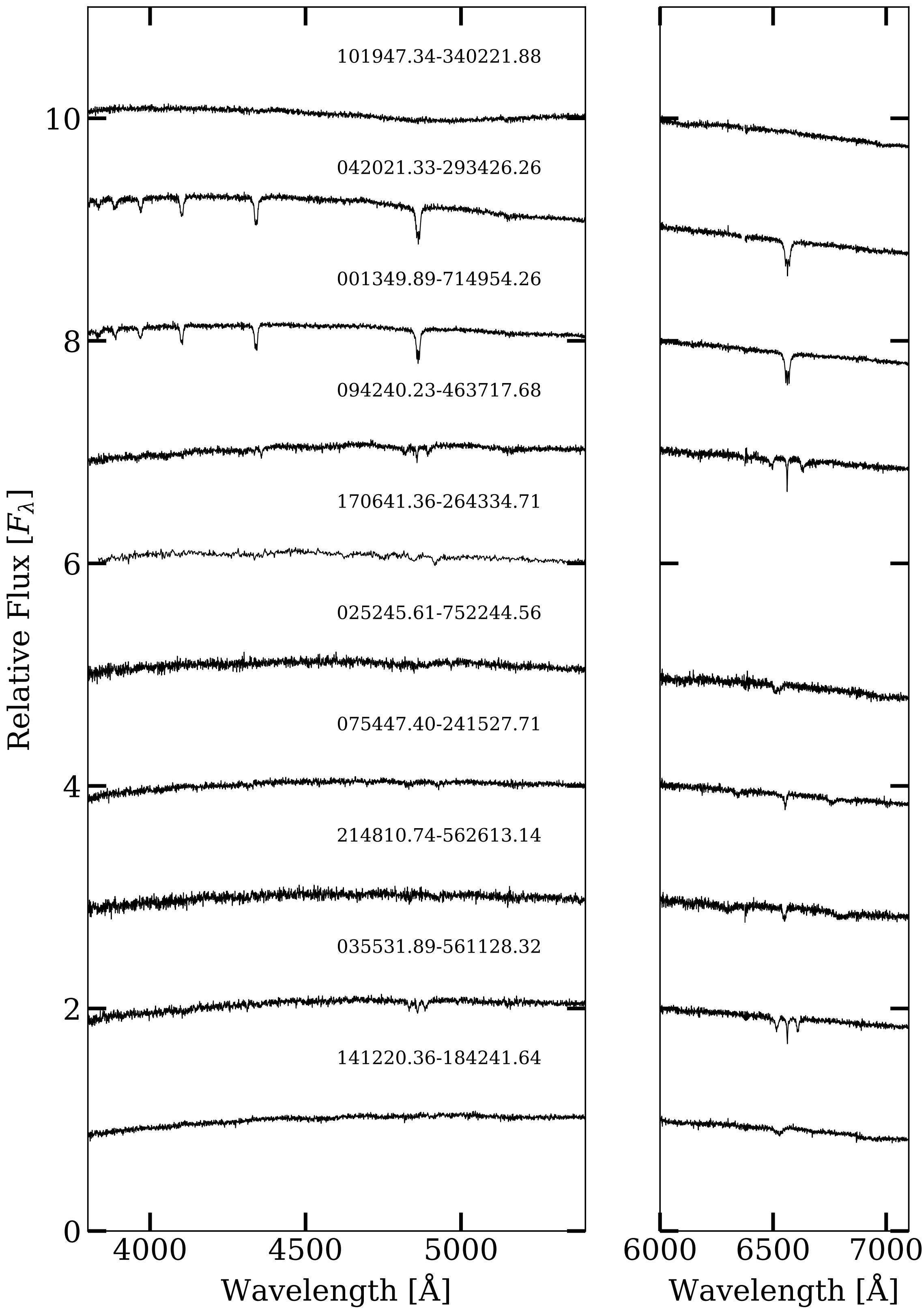

Figure A3. Spectroscopic observations of 28 DAH magnetic white dwarfs ordered with decreasing photometric temperature (2/3). Temperature range: 6700 K > $T_{\rm eff}$ > 5700 K.

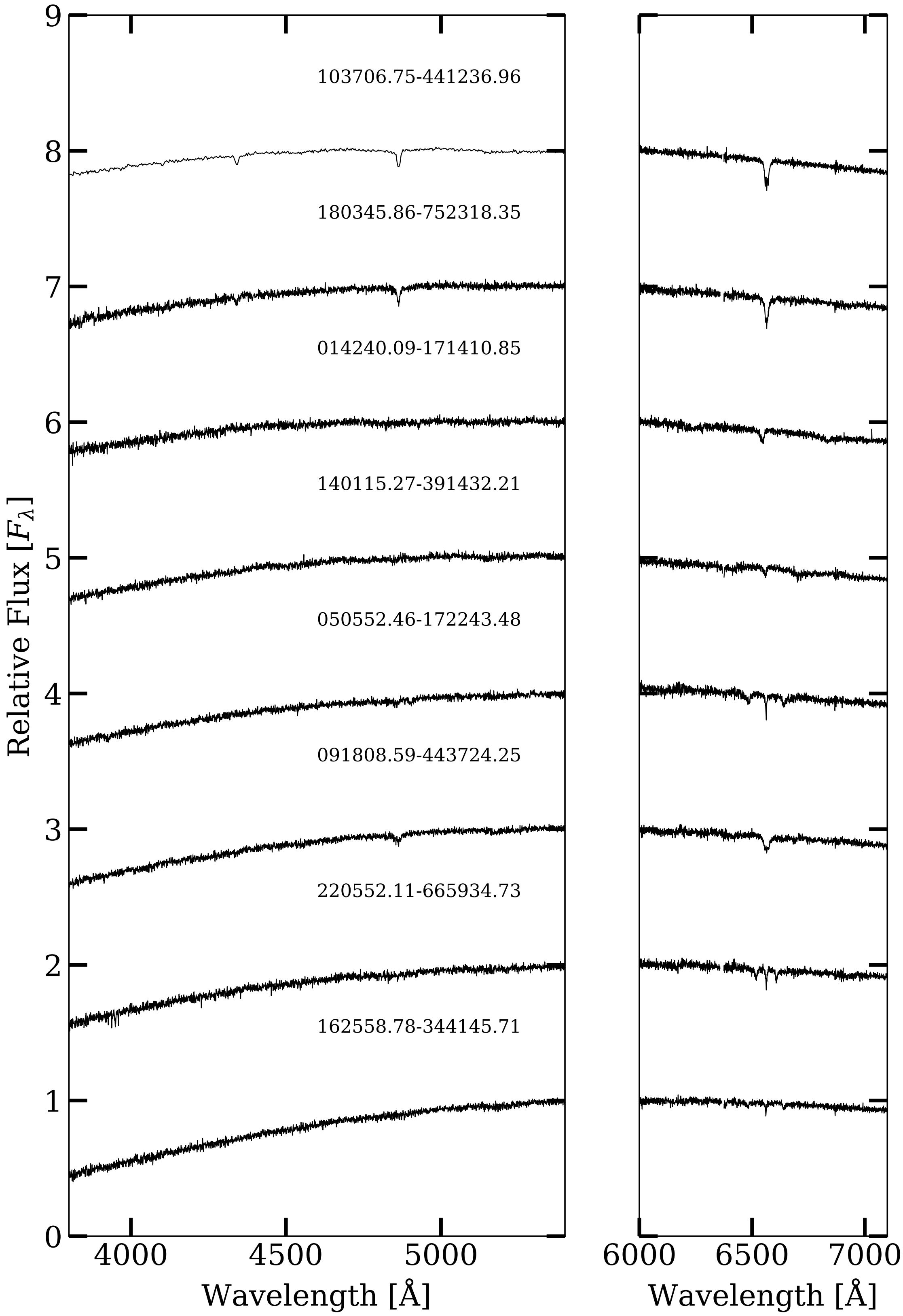

Figure A3. Spectroscopic observations of 28 DAH magnetic white dwarfs ordered with decreasing photometric temperature (3/3). Temperature range: 5700 K > $T_{\rm eff}$ > 5000 K.

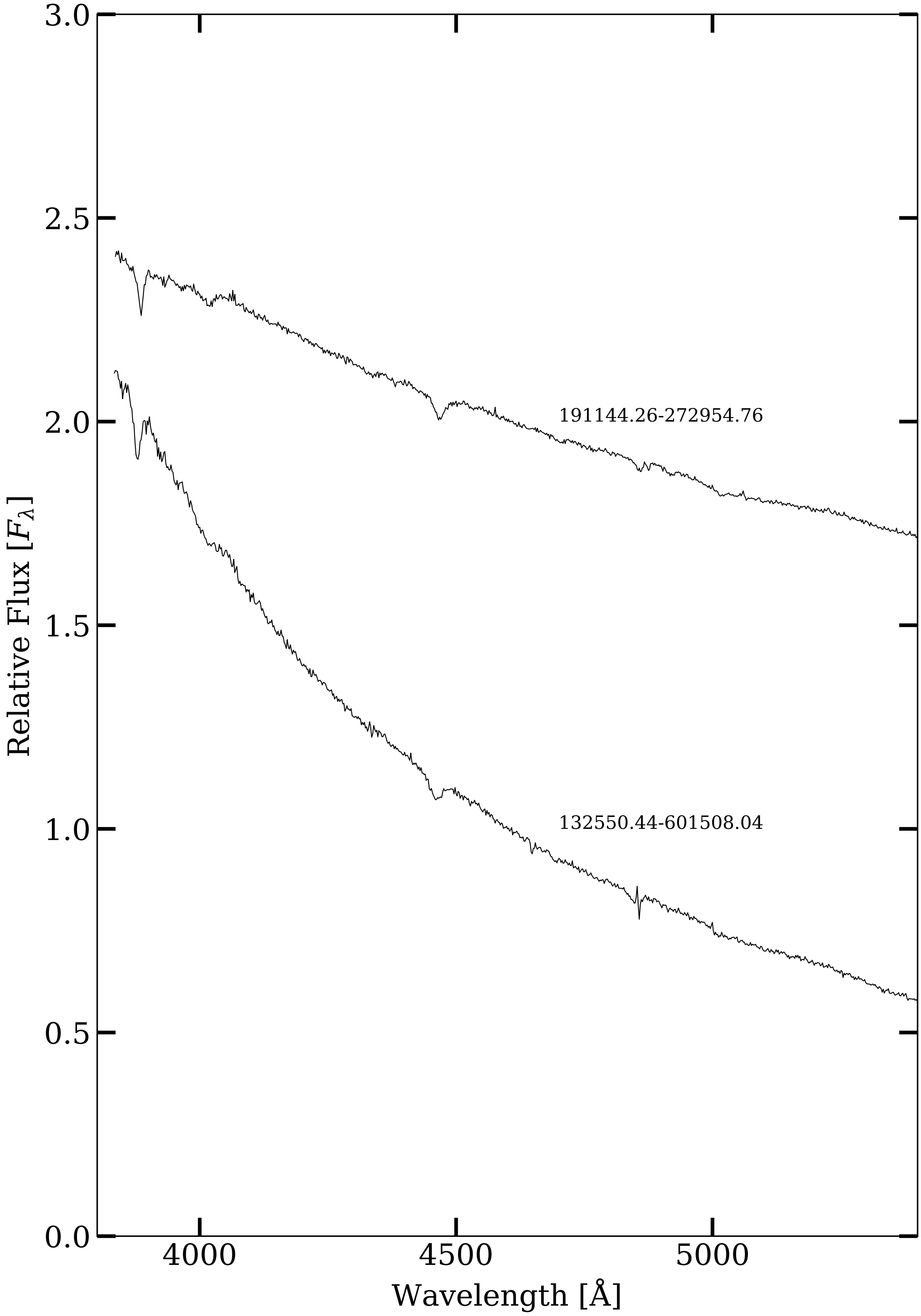

Figure A4. Spectroscopic observations of 2 DB white dwarfs.

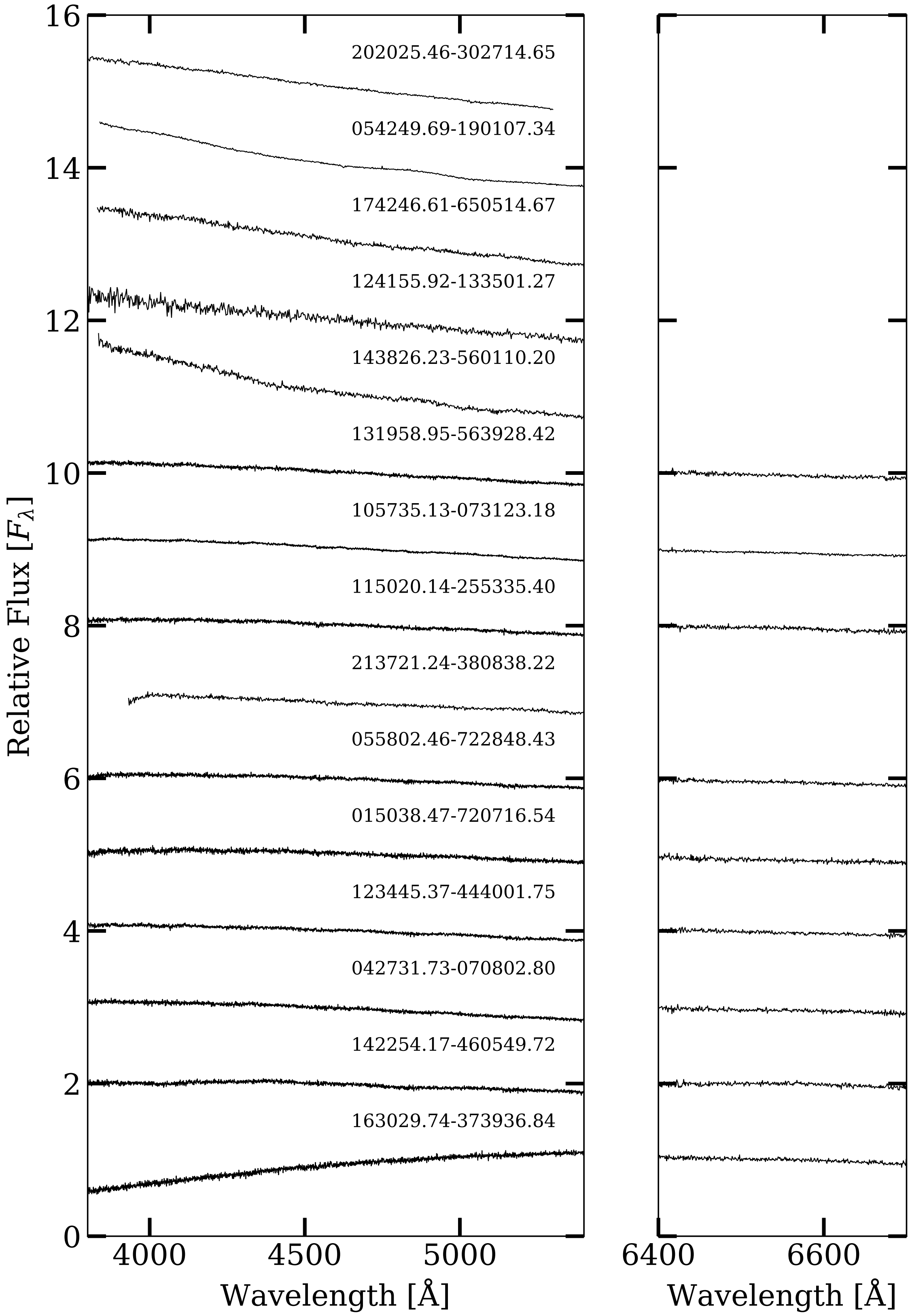

Figure A5. Spectroscopic observations of 69 DC white dwarfs ordered with decreasing photometric temperature (1/4). Temperature range: 10 500 K > T_{eff} > 6600 K.

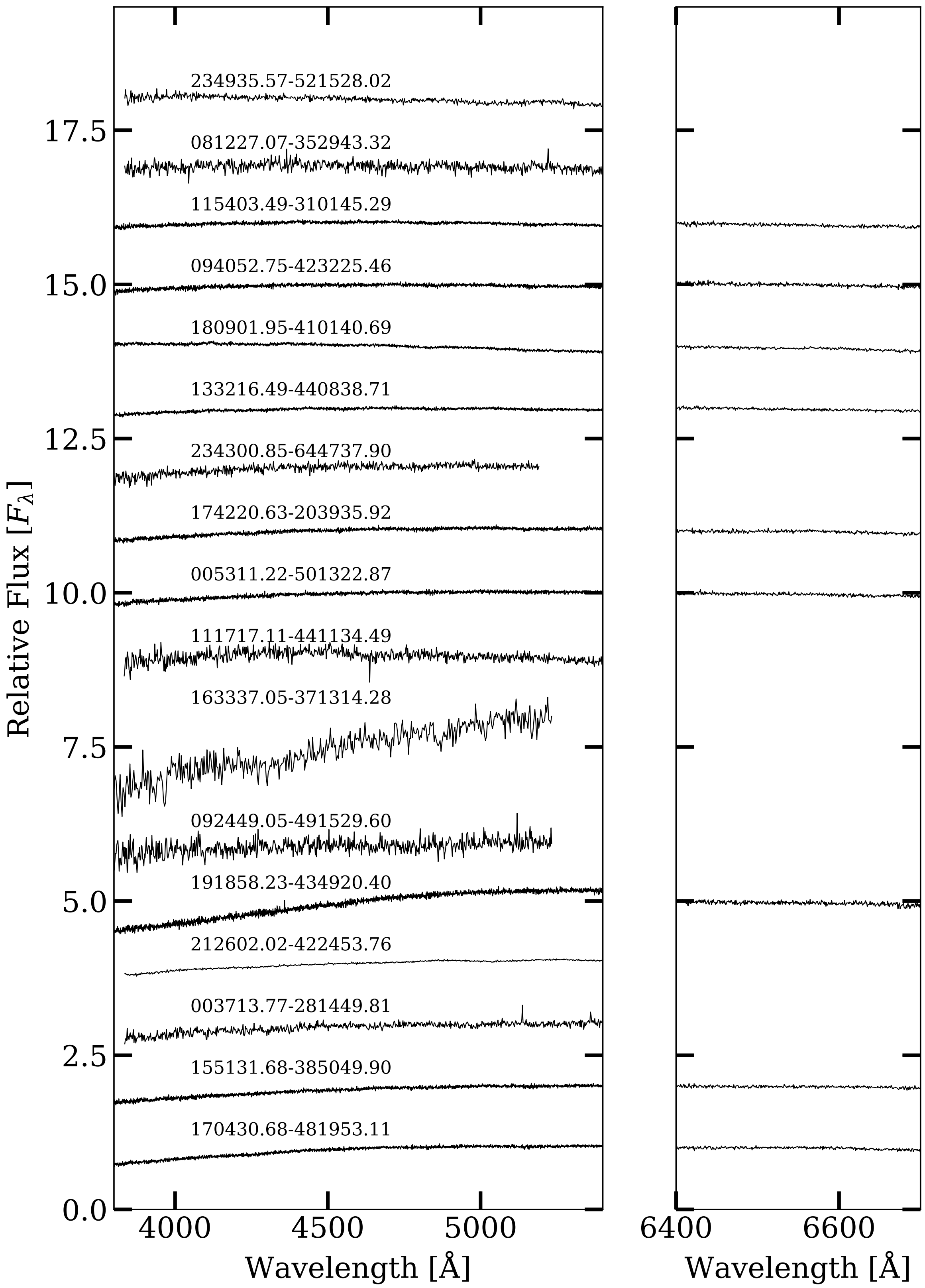

Figure A5. Spectroscopic observations of 69 DC white dwarfs ordered with decreasing photometric temperature (2/4). Temperature range: 6600 K > $T_{\rm eff}$ > 5200 K.

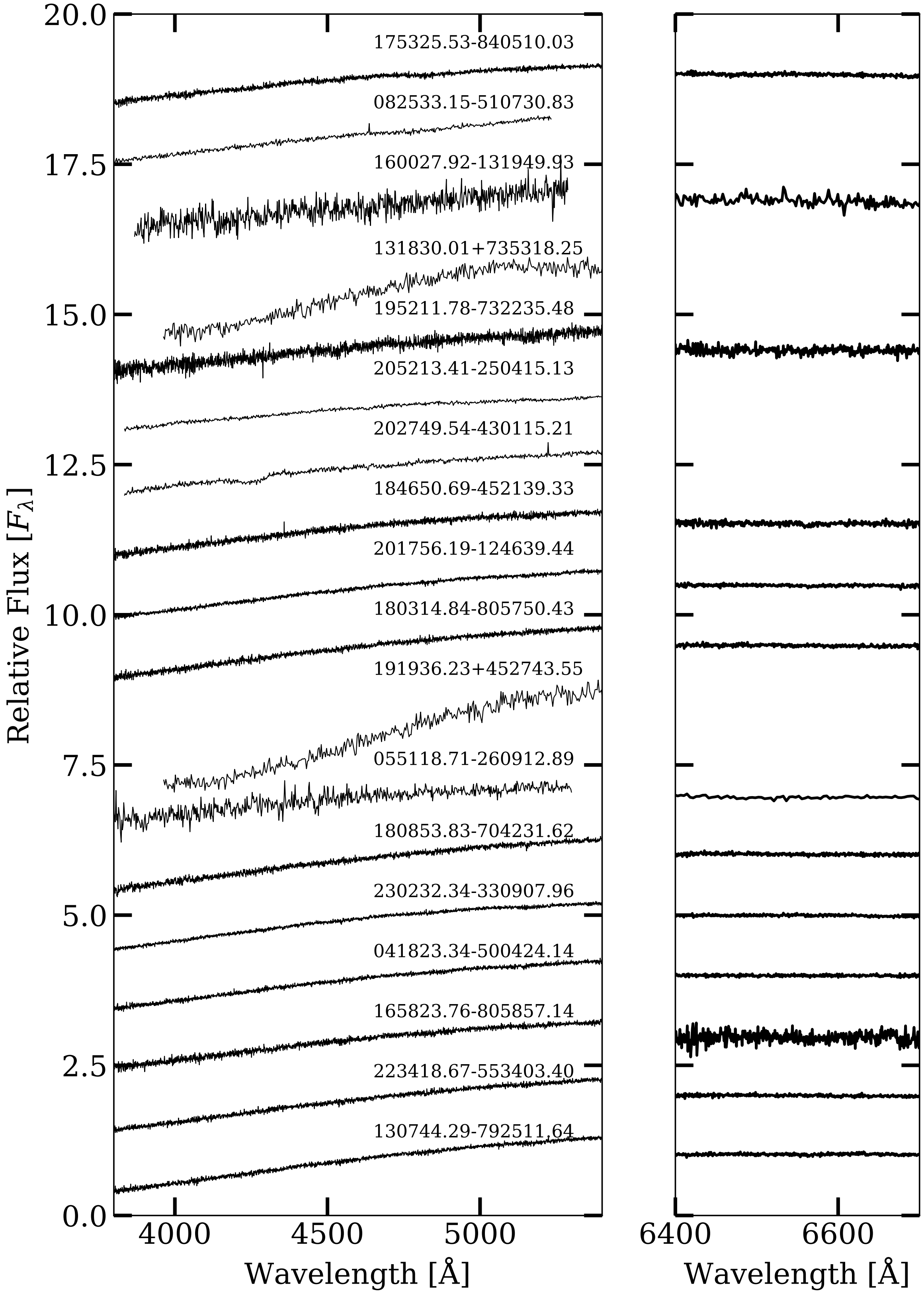

Figure A5. Spectroscopic observations of 69 DC white dwarfs ordered with decreasing photometric temperature (3/4). Temperature range: 5200 K > $T_{\rm eff}$ > 4700 K.

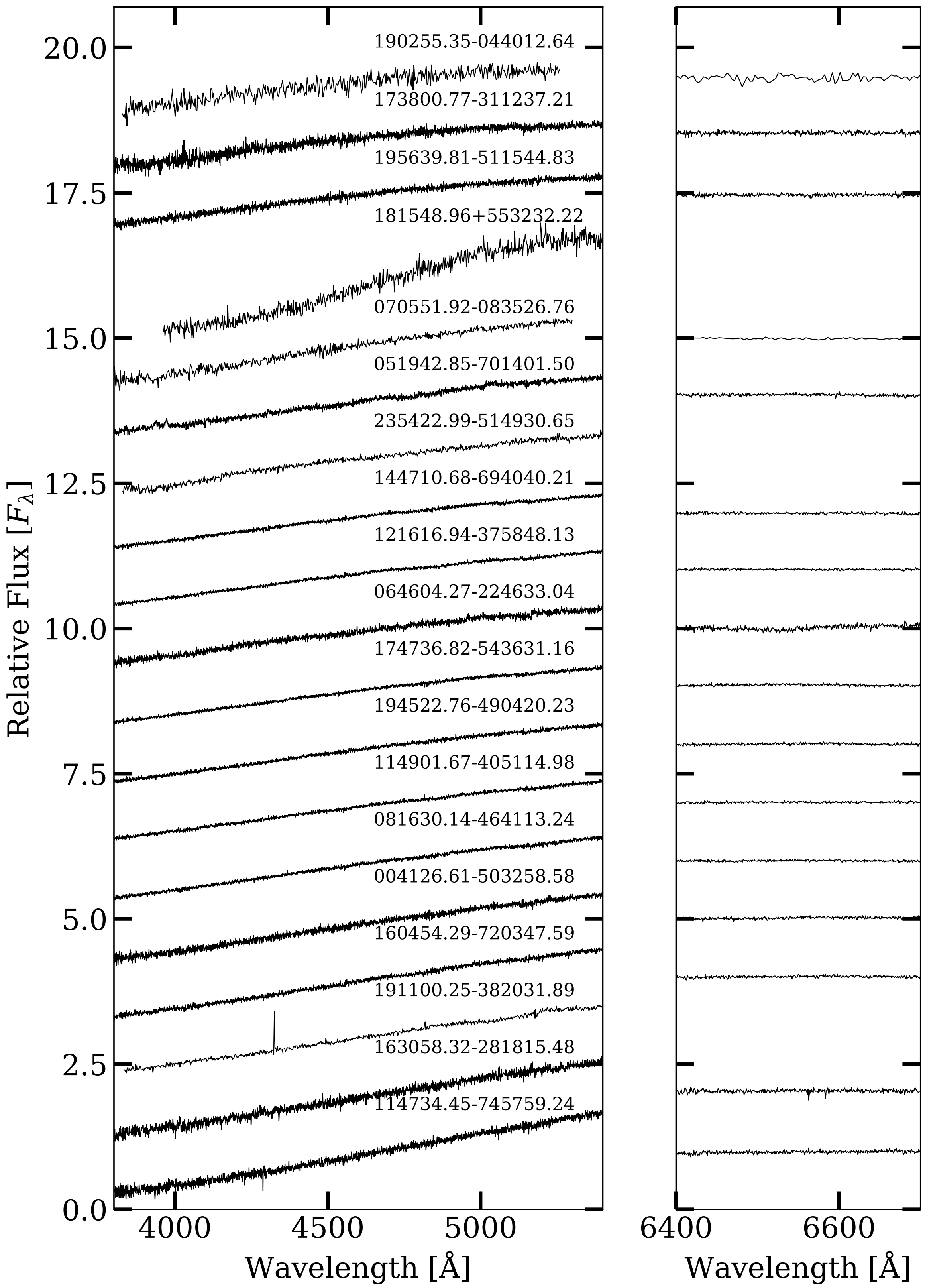

Figure A5. Spectroscopic observations of 69 DC white dwarfs ordered with decreasing photometric temperature (4/4). Temperature range: 4700 K > $T_{\rm eff}$ > 3800 K.

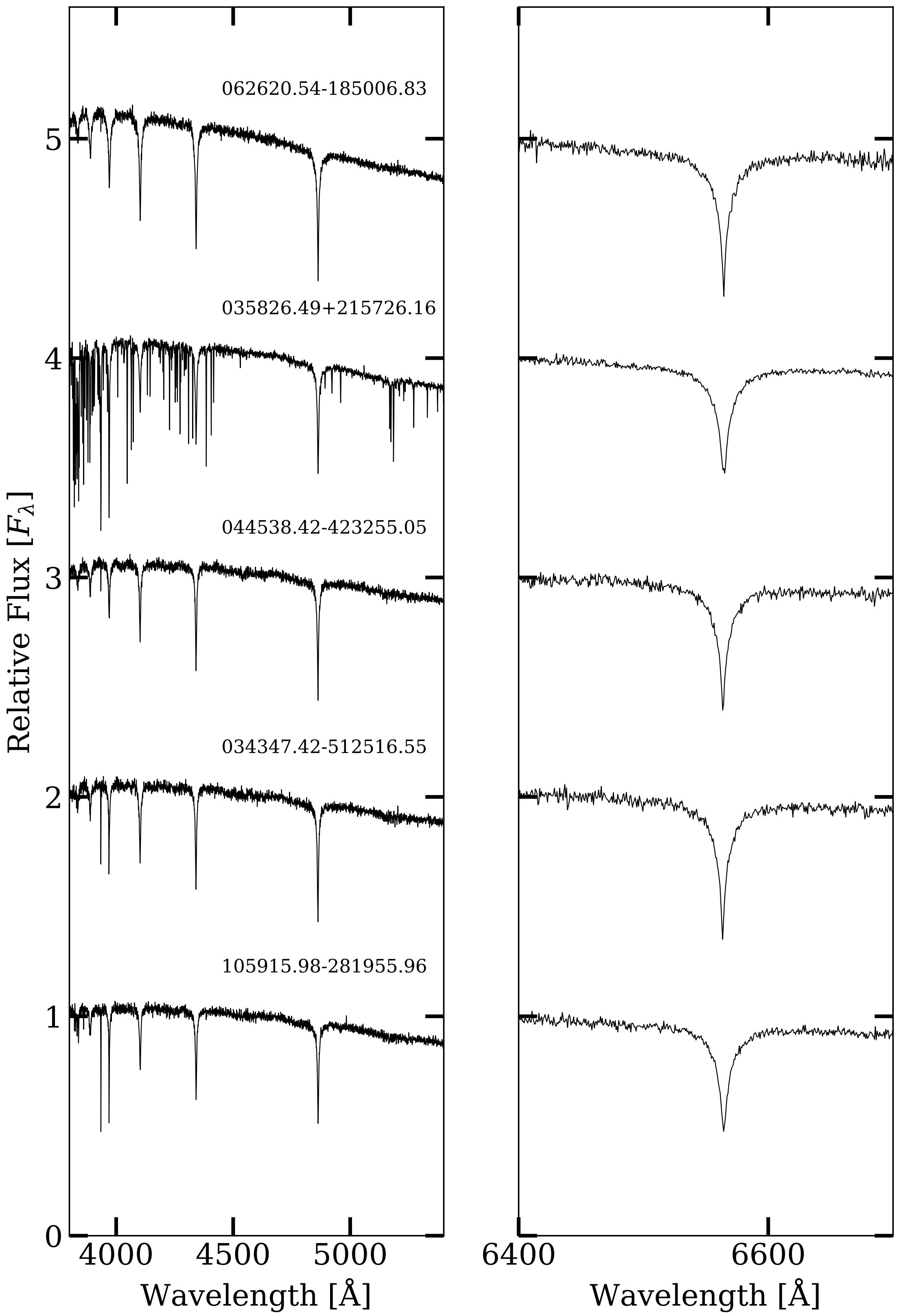

Figure A6. Spectroscopic observations of 10 DAZ white dwarfs ordered with decreasing photometric temperature (1/2). Temperature range: 7300 K > $T_{\rm eff}$ > 6600 K.

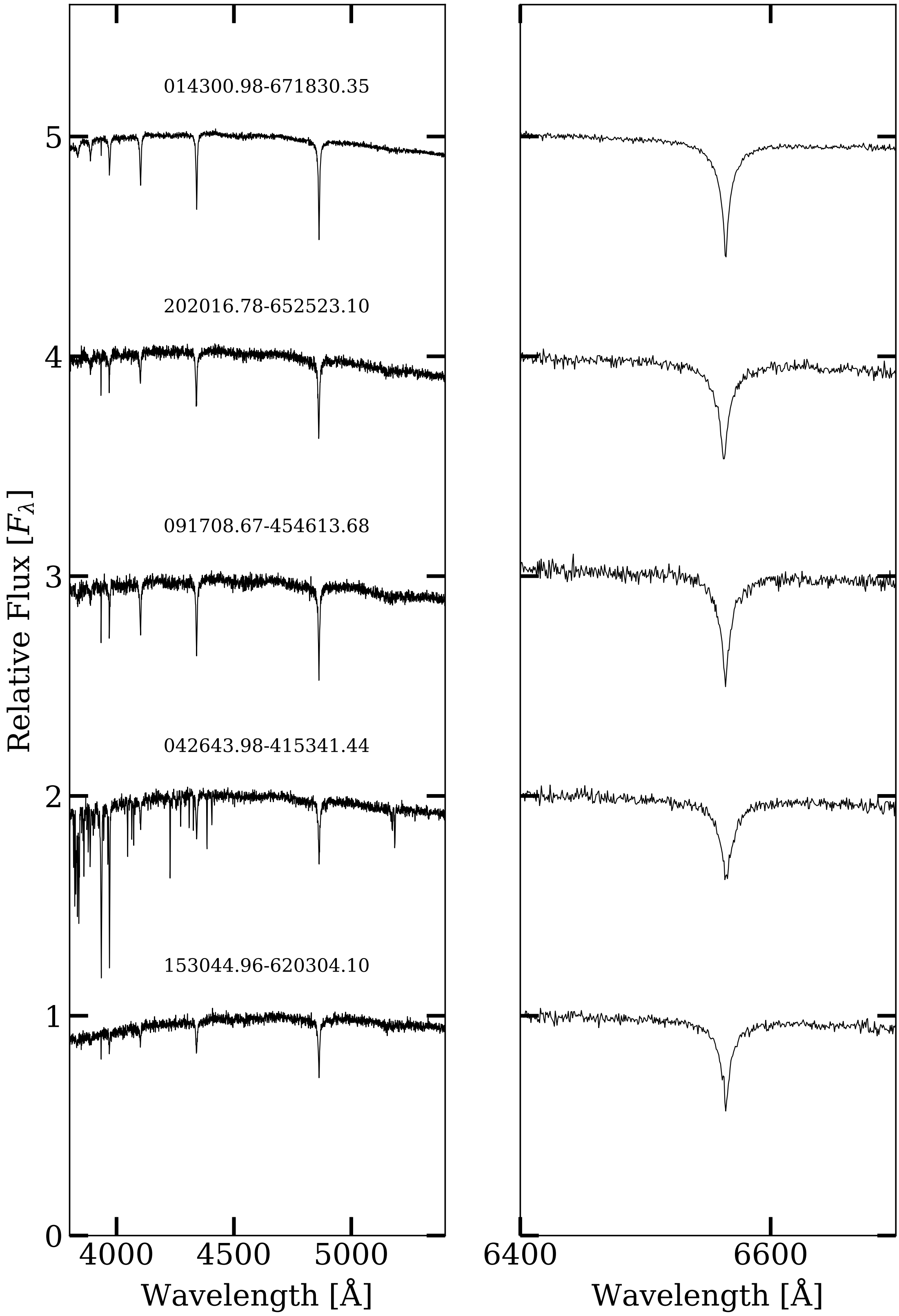

Figure A6. Spectroscopic observations of 10 DAZ white dwarfs ordered with decreasing photometric temperature (2/2). Temperature range: 6600 K > T_{eff} > 5900 K.

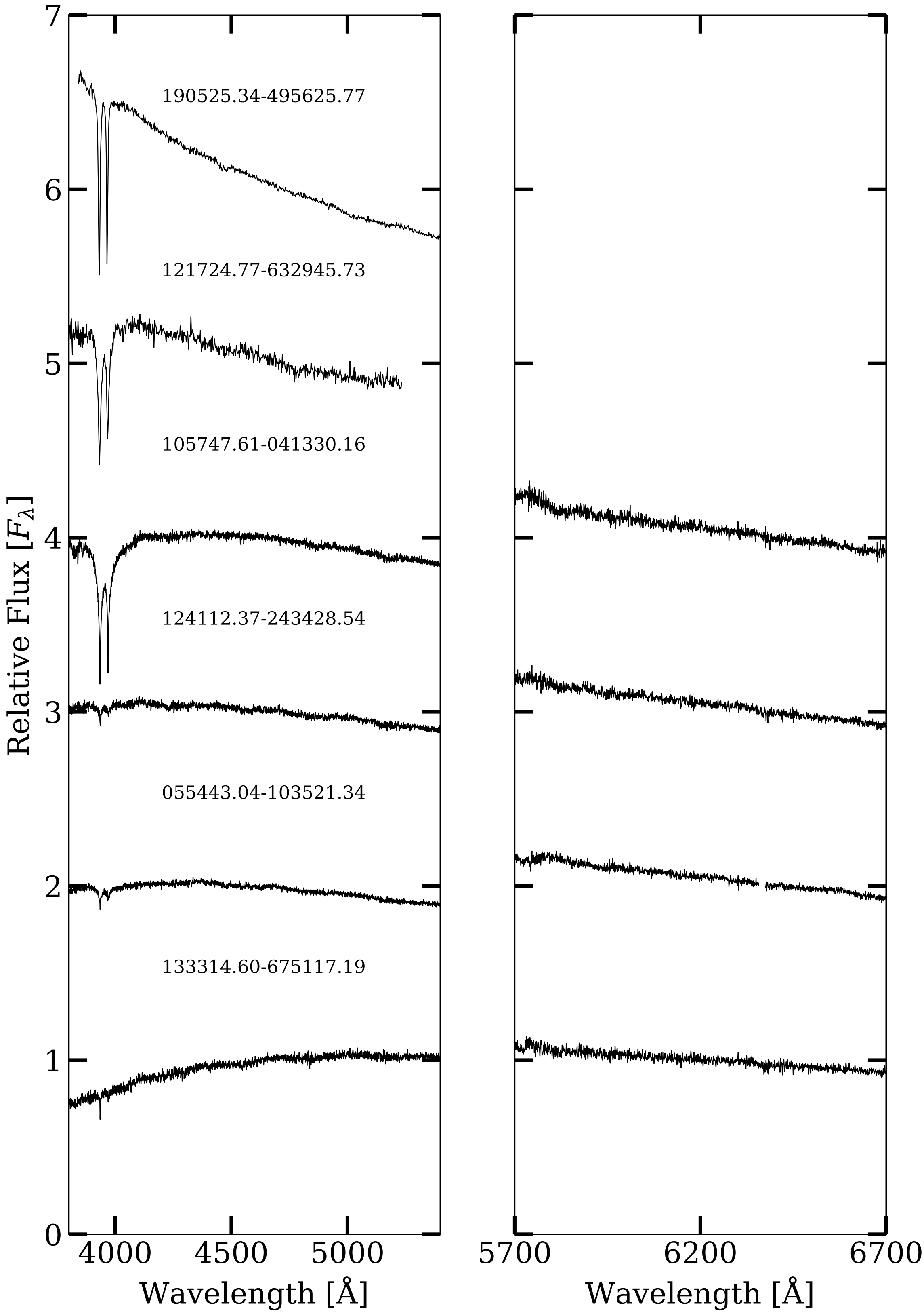

Figure A7. Spectroscopic observations of 11 DZ white dwarfs ordered with decreasing photometric temperature (1/2). Temperature range: 11 000 K > $T_{\rm eff}$ > 5700 K.

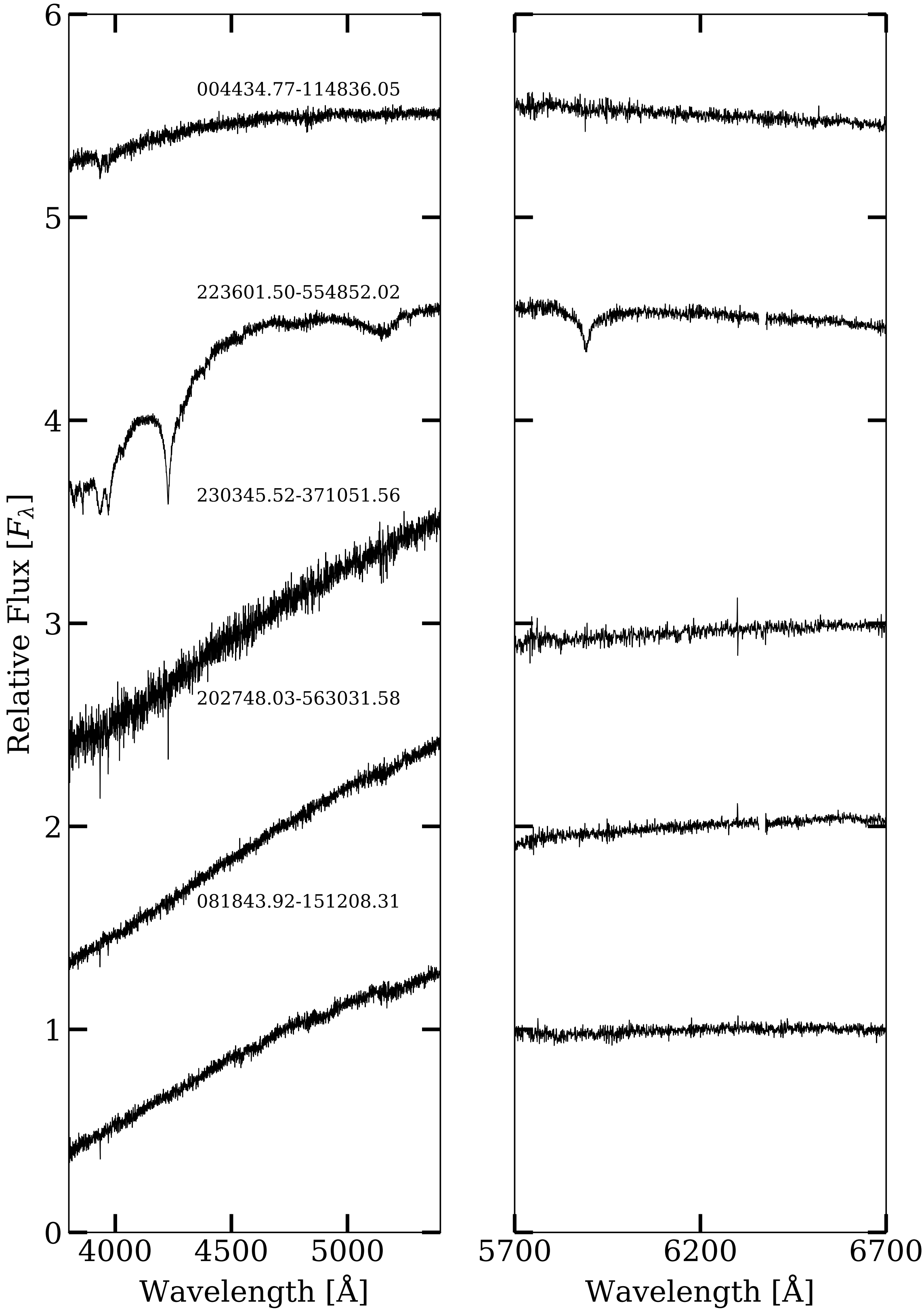

Figure A7. Spectroscopic observations of 11 DZ white dwarfs ordered with decreasing photometric temperature (2/2). Temperature range: 5700 K > $T_{\rm eff}$ > 4000 K.

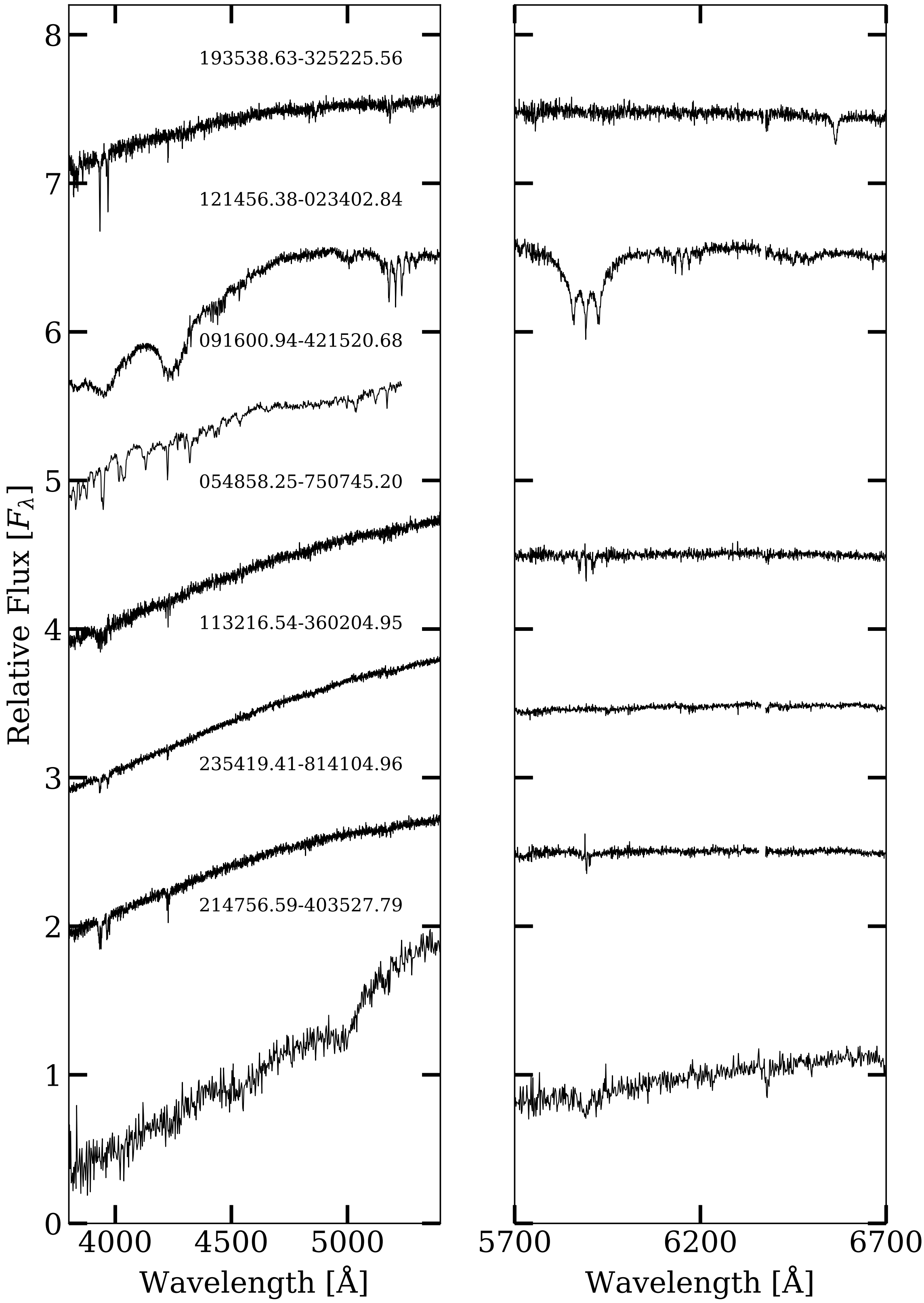

Figure A8. Spectroscopic observations of 7 DZH, DZAH, and DZQH magnetic white dwarfs ordered with decreasing photometric temperature. **WD J2147−4035** also displays carbon features (DZQH).

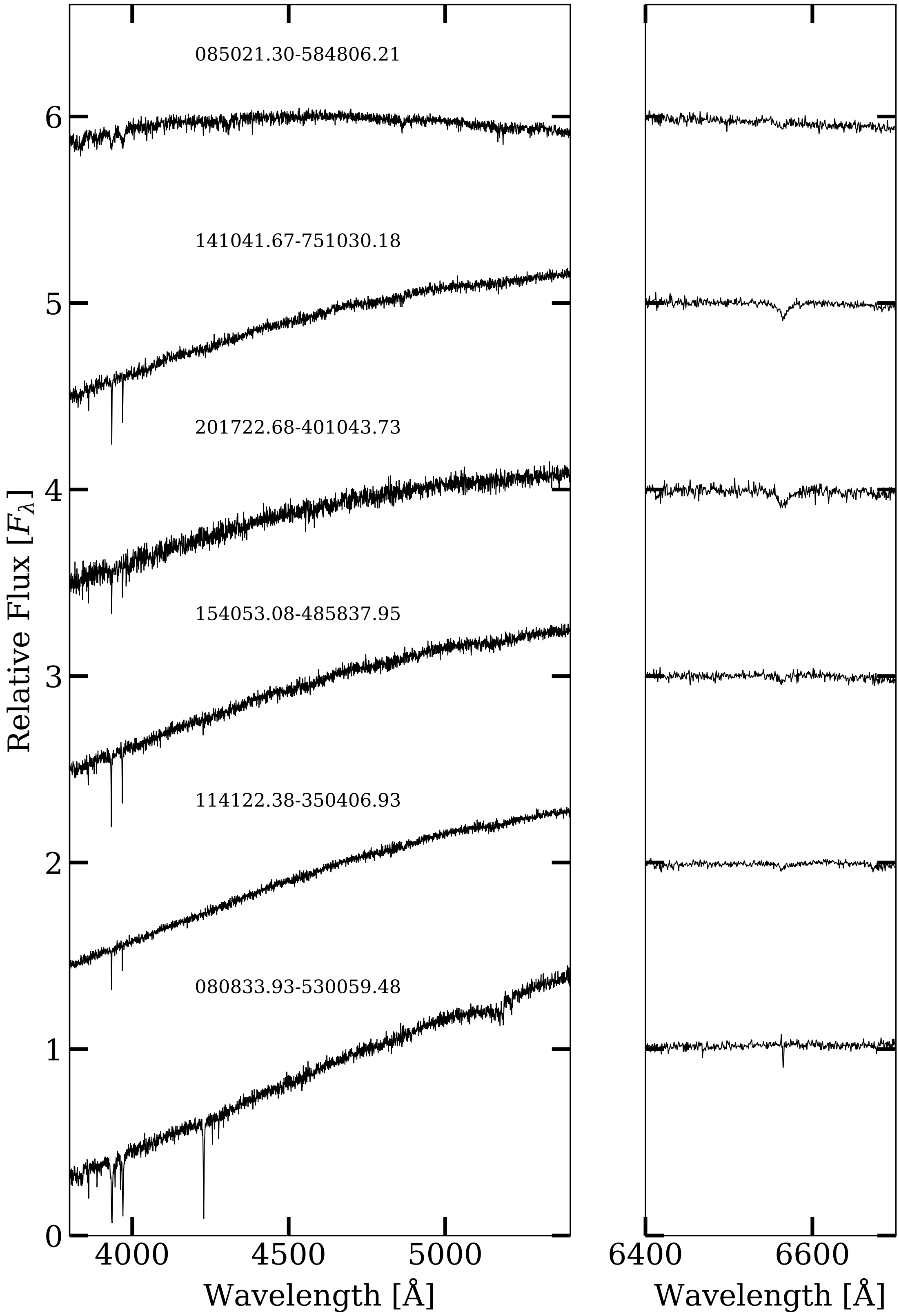

Figure A9. Spectroscopic observations of 6 DZA white dwarfs ordered with decreasing photometric temperature.

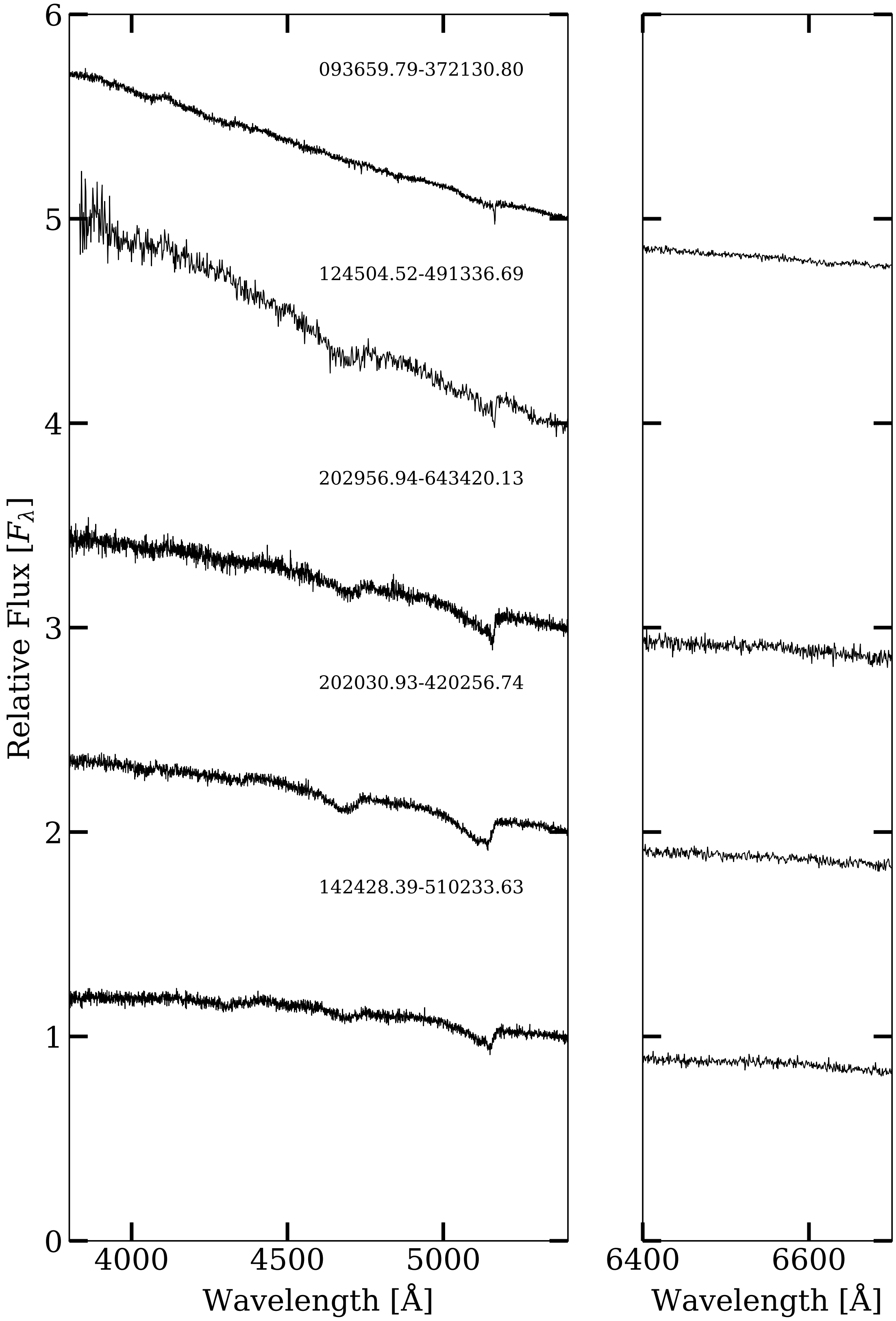

Figure A10. Spectroscopic observations of 9 DQ white dwarfs ordered with decreasing photometric temperature (1/2). Temperature range: 9200 K > $T_{\rm eff}$ > 6700 K.

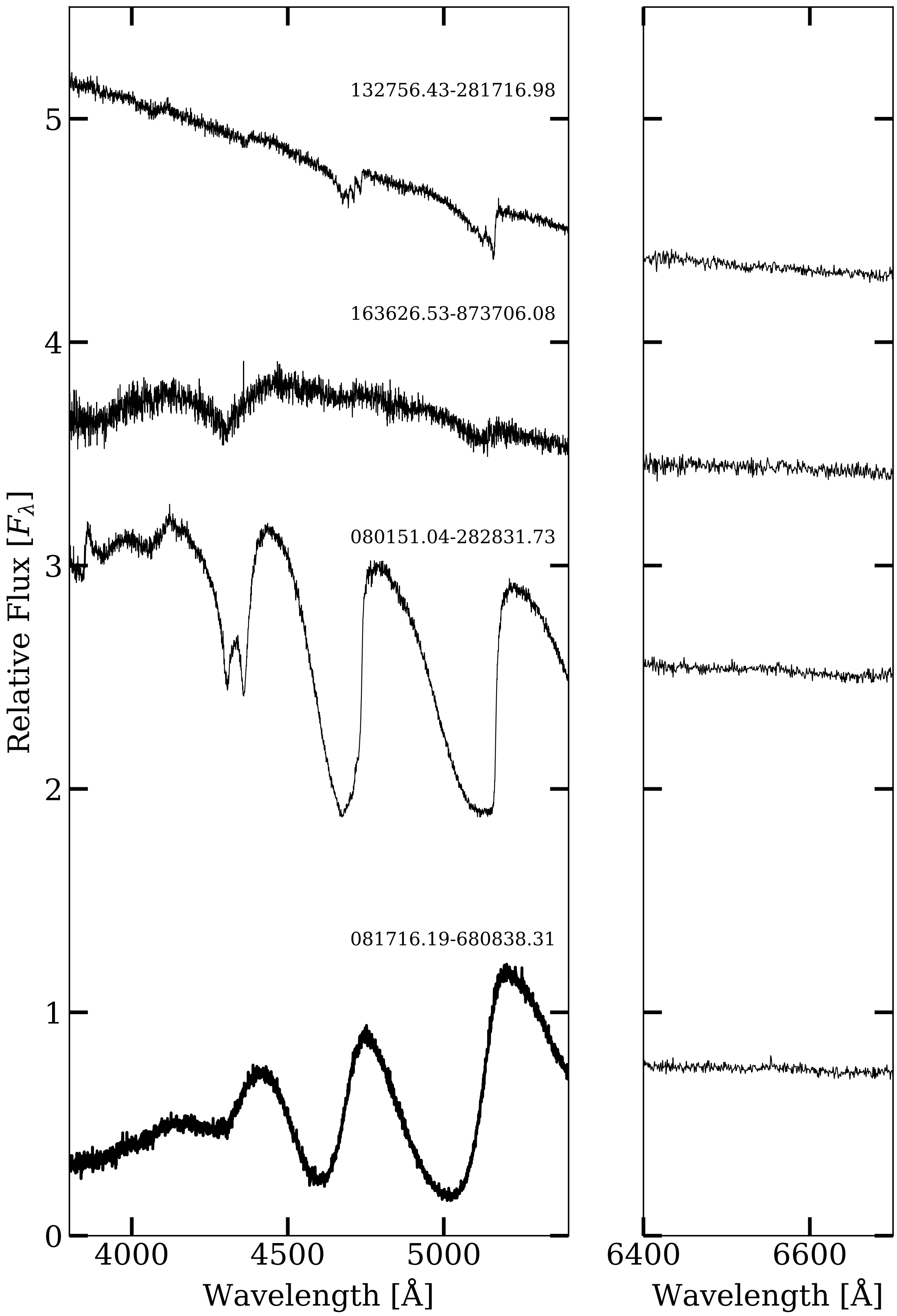

Figure A10. Spectroscopic observations of 9 DQ white dwarfs ordered with decreasing photometric temperature (2/2) The bottom two are classified as peculiar DQ (DQpec) white dwarfs. Temperature range: 6700 K > $T_{\rm eff}$ > 4400 K.

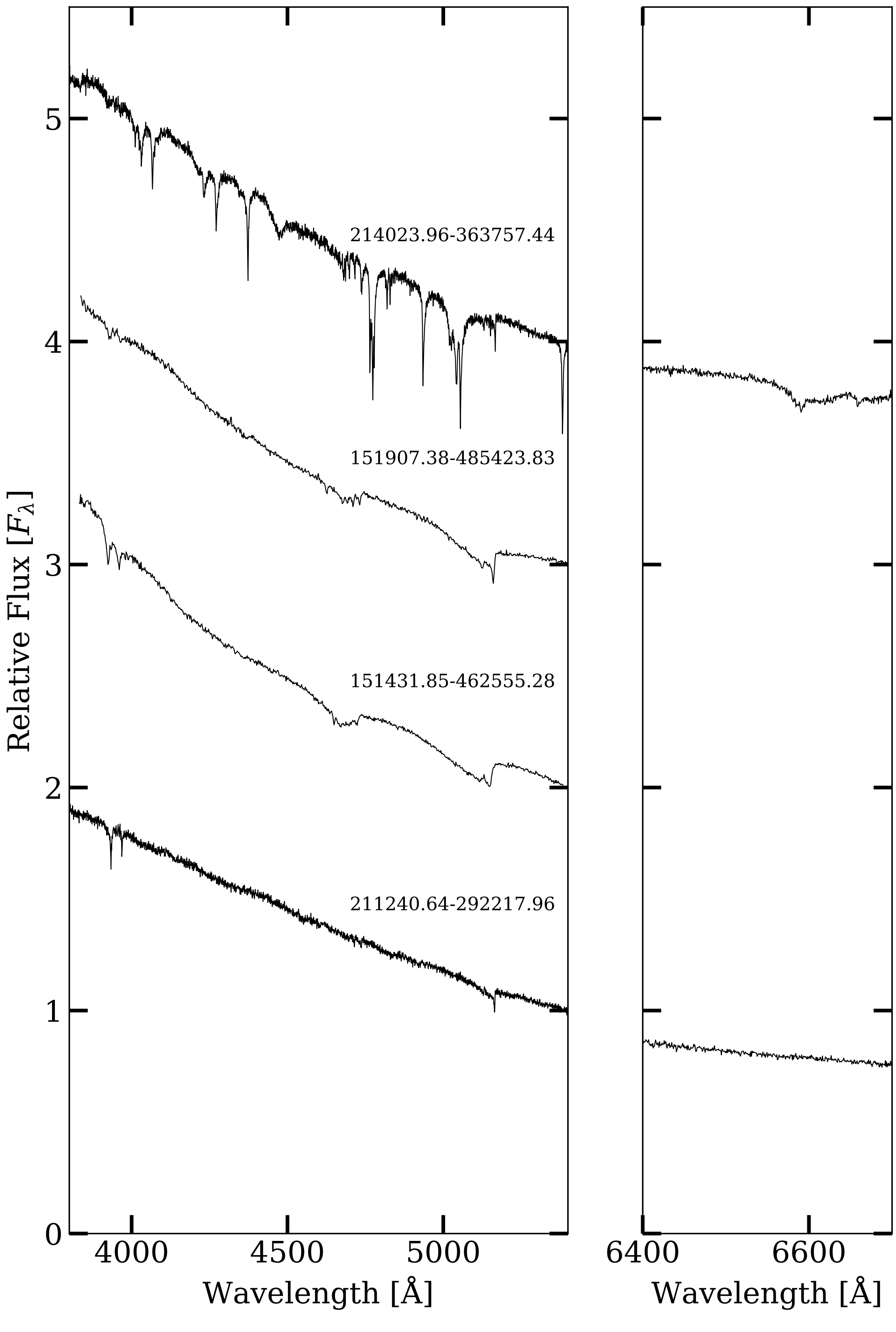

Figure A11. Spectroscopic observations of a warm DQ white dwarf (top), two DQZ white dwarfs (middle) and one DZQ white dwarf (bottom).

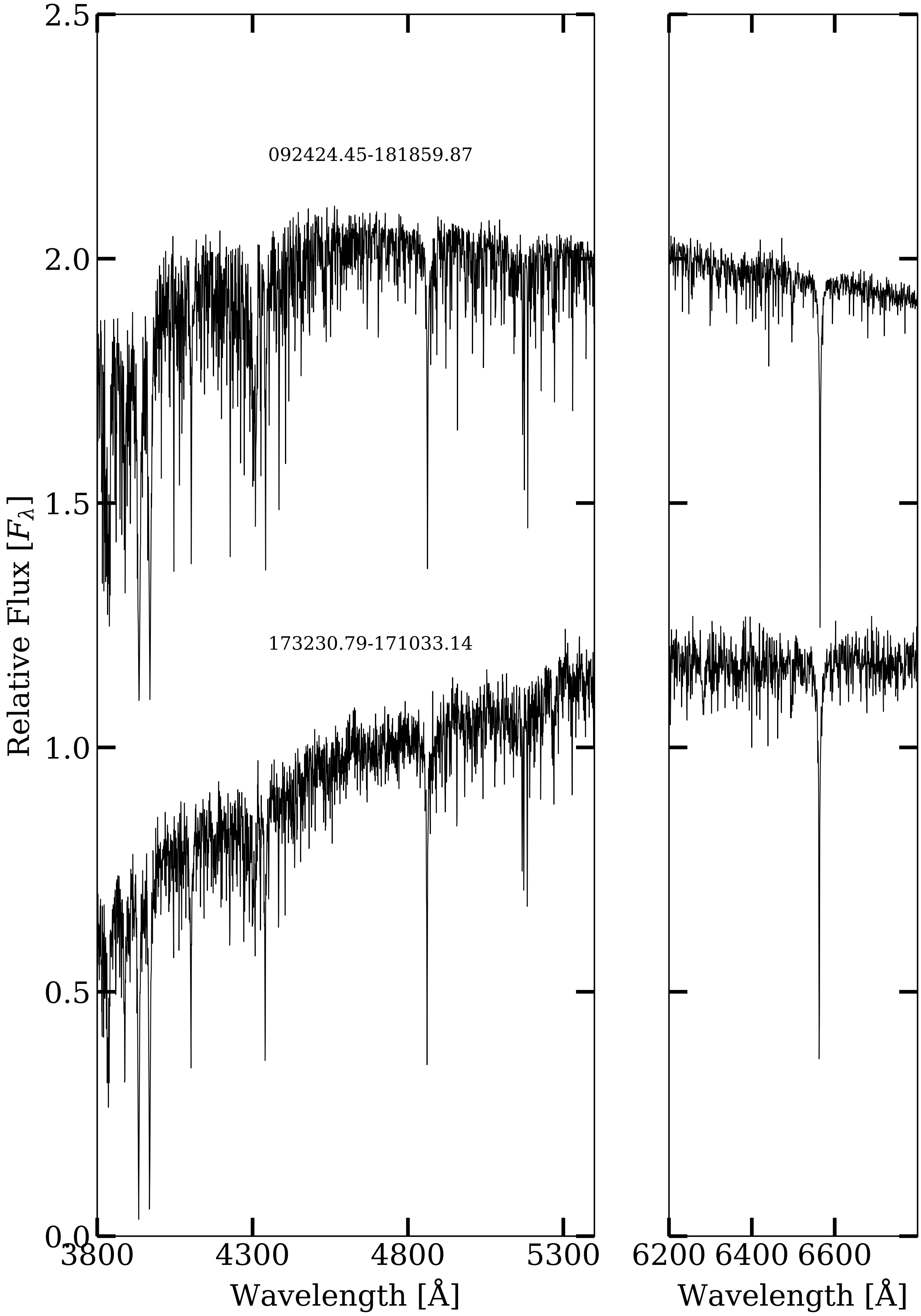

Figure A12. Spectroscopic observations of main-sequence stars that are high-probability white dwarf candidates ($P_{WD} > 0.99$) in DR3 Gentile Fusillo et al. (2021).